PFG

Photogrammetrie
Fernerkundung
Geoinformation

Organ der Deutschen Gesellschaft für Photogrammetrie, Fernerkundung und Geoinformation (DGPF) e. V.

Jahrgang 2012, Heft 1

E. Schweizerbart'sche Verlagsbuchhandlung
(Nägele u. Obermiller) Stuttgart 2012

DGPF

Deutsche Gesellschaft für Photogrammetrie, Fernerkundung
und Geoinformation (DGPF) e.V.
Gegründet 1909

Die *Deutsche Gesellschaft für Photogrammetrie, Fernerkundung und Geoinformation* (DGPF)
e.V. unterstützt als Mitglieds- bzw. Trägergesellschaft die folgenden Dachverbände:

isprs

International Society
for Photogrammetry
and Remote Sensing

DAGM

Deutsche Arbeits-
gemeinschaft für
Mustererkennung e.V.

GeoUnion
Alfred-Wegener-Stiftung

PFG – Jahrgang 2012, Heft 1
Inhaltsverzeichnis

Editorial

Originalbeiträge

Beiträge aus Wissenschaft und Praxis

Mitteilungen

Zusammenfassungen der „Originalbeiträge" und der „Beiträge aus Wissenschaft und Praxis"
(deutsch und englisch) sind auch verfügbar unter www.dgpf.de/neu/pfg/ausgaben.htm

Department of Optical Information Systems (OS) – Sensors and Instruments for Space- and Airborne Applications

Preface: This PFG-issue focuses on the work of the Department of Optical Information Systems (OS) at the Institute of Robotics and Mechatronics of the German Aerospace Center (DLR). DLR is Germany's national research centre for aeronautics and space. Its extensive research and development work in aeronautics, space, transportation and energy is integrated into national and international cooperative ventures. As Germany's Space Agency, the German federal government has given DLR responsibility for the forward planning and implementation of the German space programme. Presently, the DLR is composed of about 100 departments and 31 institutes. However, the department of OS is the only one specialized on airborne and space borne optical sensors.

In combination with engineering research the latest generations of spaceborne sensor systems are able to achieve the highest spatial and spectral resolutions to meet the requirements of Earth and planetary observation systems. The combination of large line and / or matrix detectors with intelligent synchronization control, fast read-out chains and new focal plane concepts open the door to new remote-sensing and smart deep space instrumentation.

The Department of Optical Information Systems was founded in 2003. Its predecessor was founded in 1981 as the Institute of Space Research of the Academy of Sciences of the GDR with the focus of Earth observation hardware and real time information processing. After the German reunification parts of the institute were integrated in the DLR. Thus, Berlin-Adlershof has been a centre for optical remote sensing sensors for 40 years.

In the past 20 years many widely known air- and space sensors had their origin in the department of OS. This editorial highlights the scientific results of DLR and OS in Ber-lin-Adlershof over the last two decades in the field of leading edge instrumentation and focal plane designs for space- and airborne applications. The paper includes instruments and sensors developed by DLR-OS which have influenced photogrammetry, planetary research and remote sensing. The articles that follow provide an insight in the present scientific work of the department.

Vorwort: Das vorliegende PFG-Heft widmet sich schwerpunktmäßig der Abteilung Optische Informationssysteme (OS) am Institut für Robotik und Mechatronik des Deutschen Zentrums für Luft- und Raumfahrt (DLR). Das DLR ist Deutschlands nationales Forschungszentrum für Luft- und Raumfahrt. Seine umfangreichen Forschungs- und Entwicklungsarbeiten in Luftfahrt, Raumfahrt, Verkehr und Energie sind in nationale und internationale Kooperationen eingebunden. Als Deutschlands Raumfahrt-Agentur hat die Bundesregierung dem DLR die Planung und Umsetzung der deutschen Raumfahrtaktivitäten übertragen.

Zum DLR gehören derzeit etwa 100 Abteilungen, die in 31 Instituten zusammengefasst sind. Allerdings ist OS die einzige Abteilung, die auf flugzeug- und satellitengestützte optische Sensoren spezialisiert ist.

Mit Hilfe der Ingenieurswissenschaften und der neusten Generation dieser Raumfahrttechnologien erreichen diese Produkte eine Qualität, die für höchste geometrische und spektrale Auflösung genutzt werden kann. Die Kombination von großen Zeilen- und / oder Matrix-Detektoren mit intelligenter Synchronisation, schnellen Verarbeitungsketten, und neuen Fokalebenenkonzepten öffnet die Tür für neue Erdbeobachtungs- und Tiefrauminstrumente.

Die Ursprünge der Abteilung gehen auf das 1981 gegründete Institut für Kosmosfor-

schung der Akademie der Wissenschaften der DDR zurück. Nach der Wende wurden Teile des Instituts vom DLR übernommen. Die Abteilung OS wurde 2003 gegründet. Damit ist seit 40 Jahren der Standort Berlin Adlershof ein Zentrum der optischen Sensorik für die Fernerkundung.

In den letzten 20 Jahren sind viele bekannte Sensoren am OS entwickelt worden. Das Editorial ist eine Darstellung der technologischen und wissenschaftlichen Resultate der letzten zwanzig Jahre, in denen die Abteilung OS eine führende Rolle in der Sensor- und Instrumentenentwicklung für die Luft- und Raumfahrt gespielt hat. OS hat und wird neue Detektorentwicklungen betreiben und neue höchstgenaue Verarbeitungstechnologien entwickeln, die es ermöglichen, den immer weiter steigenden Anforderungen der Nutzer gerecht zu werden. Die weiteren Artikel des PFG-Heftes gewähren einen Einblick in die aktuellen Forschungsarbeiten der Abteilung.

1   Introduction

The preceding institute of Optical Information Systems (OS) at the Robotics and Mechatronics Center of the German Aerospace Center (DLR) was founded 1992 at January 1. OS has been formed from parts of the former Institute of Space Research of the Academy of Sciences of the GDR. Here the members of the institute were working on a variety of technical and scientific challenges. Some highlights are change detection methods in real time for space- and airborne applications, in parallel on-chip analog processing and digital real time data processing. The following technological results reflect different steps of the digital processing chain.

Main topics are the development of sensors with high spatial and / or spectral resolution. The first on-board real time classification was demonstrated with the BIRD (Bi-Spectral Infrared Detection) satellite which provided fire maps and high temperature events in real time. For high spatial resolution the data processing is much more complex because of the need of generating the DTM first or of using an actual DTM to be able to compare the data independent of the satellite manoeuvres and scaling factors. The following parts show instruments and FPAs (focal plane assemblies) which are developed to fulfil the particular performances criteria and in parallel opens the door to the digital instrument design. For most of the shown applications, a data compression capability (lossy or lossless) as part of the digital data processing has been implemented in order to reduce the whole data rate. The Institute for Robotics and Mechatronics has also been working on 3D automatic data processing to use the technology for sensor orientation and remote sensing. In combination with the hardware technology OS is working on the next generation of remote sensing satellites, which can be used for information extraction based on change detection methods.

In the following the most significant developments are described.

2   WAOSS (Wide Angle Optoelectronic Stereo Scanner) (1996)

DLR OS was responsible for the CCD Line Scanner WAOSS for the Mars 96 Mission. The design is shown in the Fig. 1. The Wide-Angle Optoelectronic Stereo Scanner WAOSS was one of the important payload components for

Tab. 1: WAOSS Specification.

Focal Length	21.7 mm
Field of View (across track)	80 °
Convergence Angle	25 °
Number of CCD-Lines	3
Elements per CCD-Line	5184
Elements Spacing	7 µm
Spectral Channel – Nadir – Forward, Backward	470...670 nm 580...770 nm
Data Compression Method	DCT (discrete cosine transform) - JPEG
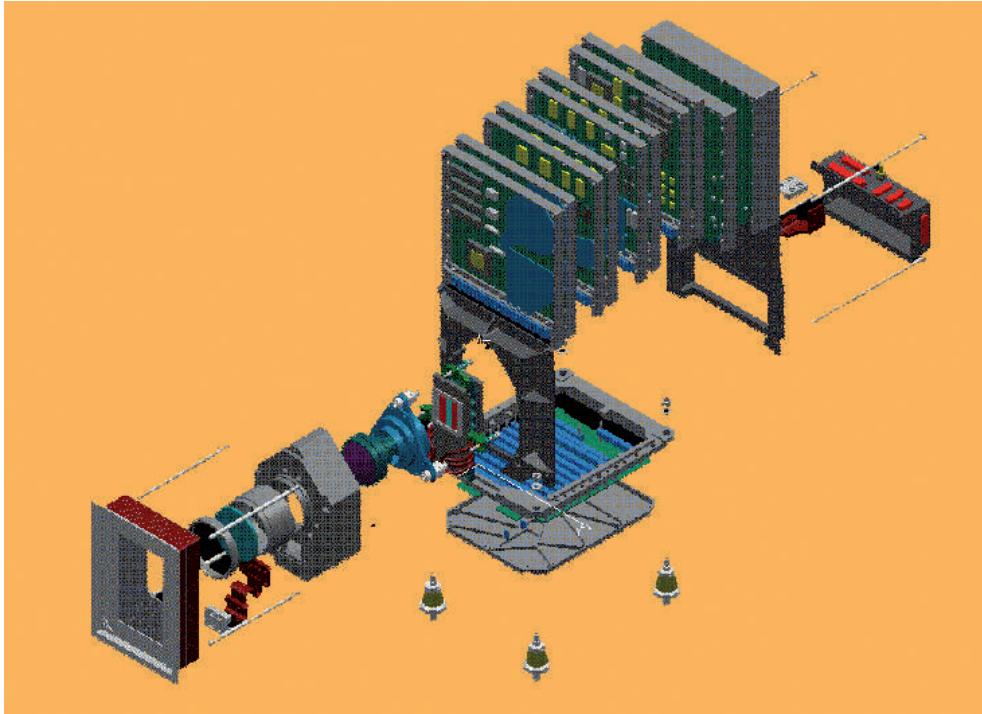
Fig. 1: Structure of the WAOSS camera (Wide-Angle Optoelectronic Stereo Scanner).
Source: WAOSS, a synoptic stereo camera for the Mars-96 mission, and WAAC, the camera for terrestrial applications. From left to right: baffle (reduces straylight), optical path, focal plane (three CCD-lines), front end electronics (redundant layout with four pairs of circuit boards), digital electronic part, compression board. CD ROM, DLR, Institut für Weltraumsensorik, Berlin, 1996.

the Mars 96 mission. WAOSS is a three line stereo scanner working in the push-broom mode. The Tab. 1 shows the most significant specifications of WAOSS. The WAOSS components and algorithms have been tested with the airborne version WAAC. The Wide Angle Airborne Camera WAAC was derived from the modular WAOSS design concept allowing flexible imaging conditions including high data rate and high data volume applications.

3 Airborne Digital Sensor (ADS40) Design (2000)

The company LH Systems and DLR OS have developed the commercial airborne digital sensor ADS40. This high-resolution imaging system is able to fulfil both photogrammetric and remote sensing requirements. The new sensor was introduced in mid-2000 and was designed to complete the digital chain for airborne photogrammetric data processing. The following Figs. 2 and 3 show that the focal

1 main ceramics	5 heat pipes
2 insert	6 ceramic frame
3 CCD	7 scattered light hood
4 holding fixture	8 electromagnetic valve
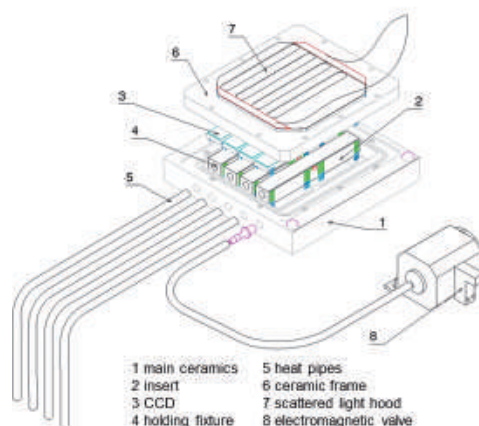
Fig. 2: ADS40 focal plane concept.
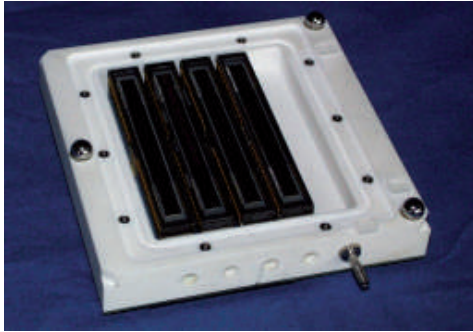
Fig. 3: ADS40 focal plane.

plane design for airborne applications is much more complicated than the one for space applications due to the fact that environmental conditions can change dramatically.

The FPA including the analog conversion and the optics define the performances of the instrument. In the case of ADS40 the flatness of 20 µm allows the small f-Number of the optics and the black detector shielding reduces the stray light effects. In order to compensate for the pressure differences an air filter and drying system was installed to avoid the optical distortion of the cover glass of the FPA. The thermal stabilisation via heatpipes is required to ensure the excellent image quality of the ADS40. The system works as a measurement device independent of the environmental conditions. The optics and the FPA were in focus to obtain the best reproducible imaging performances.

4   RapidEye: Focal Plane Assembly and Front End Electronics (2005)

This FPA has been optimised for a medium geometric and high radiometric resolution of the instrument based on the focal plane development for the airborne digital sensor ADS40. The advanced focal plane for ADS40 was modified for space in order to meet the RapidEye requirements. This focal plane is the main component of the Multi Spectral Imager (MSI) of the RapidEye payload (Fig. 4). DLR OS was the subcontractor of Jena Optronik GmbH, Jena, Germany, for the MSI development. The RapidEye satellite constellation consists of five identical small satellites. These satellites are each equipped with the powerful MSI to record imagery of the Earth in five spectral bands and with a GSD of 6.5 m. The FPA of the MSI contains five colour 12k CCD lines and the focal plane electronics. The FPA receives bias and clock signals from the front end electronic which is located in a separate box. The focal plane electronics includes the output buffering and the clock driver of the CCD. The amplified analog high speed data channel is part of the front end electronics.

5   Hot Spot Recognition System (HSRS) (2001 and 2010)

HSRS is a two-channel pushbroom scanner with spectral bands in the mid-wave infrared (MWIR) and thermal infrared (LWIR)
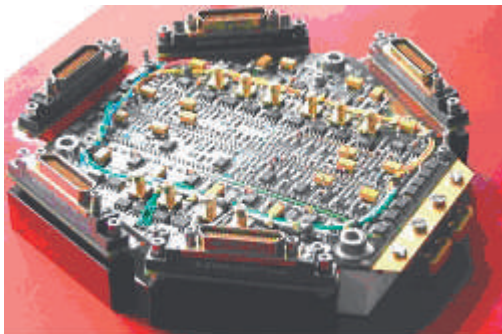
a)   b)

Fig. 4: RapidEye: a) Focal Plane with transport cover, b) without transport cover.
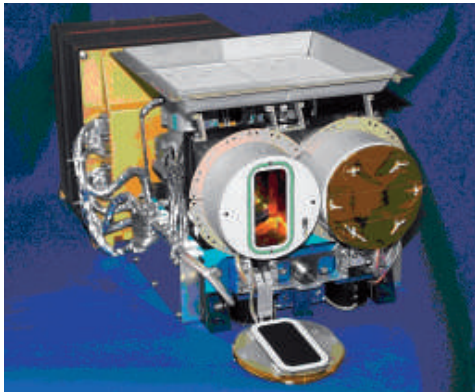
Fig. 5: Flight model HSRS 2001.

Fig. 6: Flight model HSRS 2010.
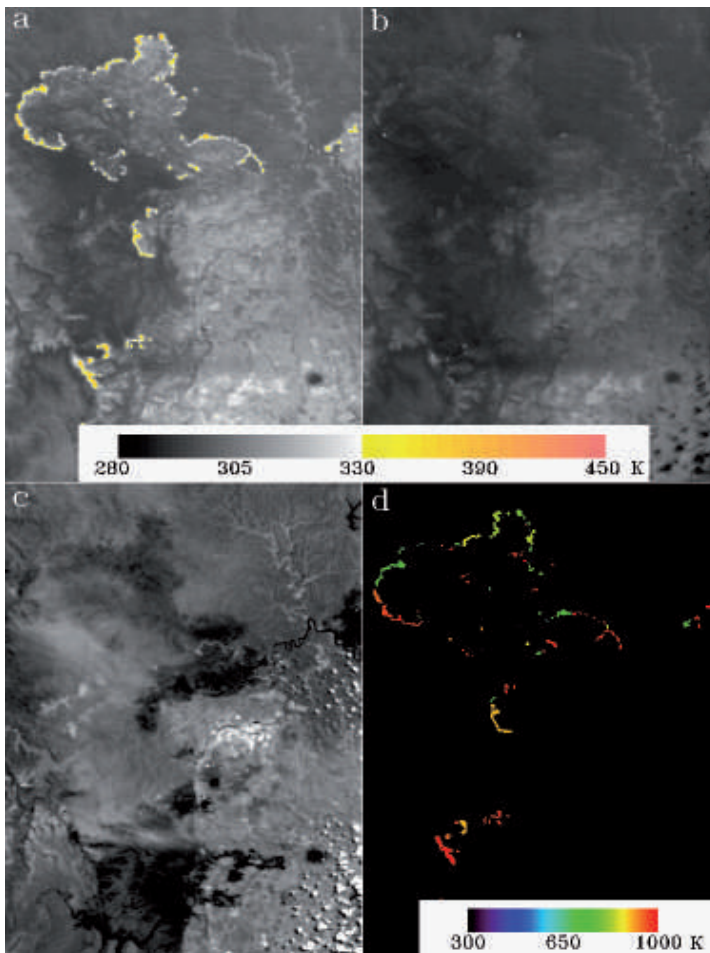
Fig. 7: BIRD image fragment of the Sydney bush fire scene observed on January 5, 2002, taken with the HSRS:
a – MWIR image
b – LWIR image
c – NIR image
d – detected hot clusters

The black-and-white and colour coding of the MWIR and LWIR images represents their pixel brightness temperature; the colour coding of the hot clusters represents their equivalent fire temperature.

Tab. 2: Modular Optical Scanner MOS IRS-P3, performance data (altitude 817 km).

Parameter	MOS-A	MOS-B	MOS-C
Spectral range [nm]	755 – 768	408 – 1010	SWIR
No. of channels	4	13	1
Wavelengths [nm]	756.7; 760.6; 763.5; 766.4	408; 443; 485; 520; 570; 615; 650; 685; 750; 870; 1010	1600
	O2A-band	815; 945 (H_2O-vapour)	
Spectral half width [nm]	1.4	10	93
FOV along track x [deg]	0.344	0.094	0.052
across track y [deg]	12.9	13.8	13.5
Swath width [km]	187	200	192
No. of pixels	420	384	299
Ground Sample Distance x*y [km²]	4.9*0.45	1.34*0.52	0.74*0.74
Measuring range Lmin ... Lmax [W/m²/nm/sr]	0.001 … 0.4	0.002 … 0.48	0.005 … 0.08
$\Delta L/L$ at L_{min} [%]	0.3	1.0	2.0

a)   b)
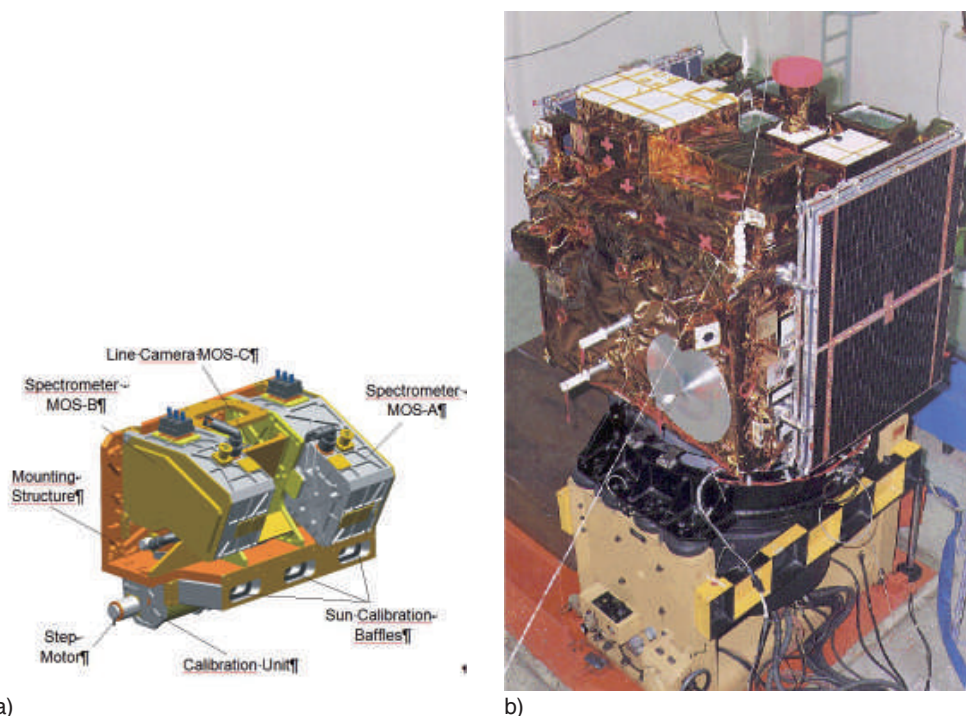
Fig. 8: MOS-instrument and Indian Remote Sensing Satellite IRS-P3 during pre-launch tests at Indian Space Research Organisation / Space Application Centre (ISRO/SAC).

spectral ranges. The detectors are two Cadmium Mercury Telluride (CdHgTe) linear photodiode arrays. The lines – with identical layout in the MWIR and LWIR – are comprised of 2 x 512 elements each in a staggered structure where two linear detector arrays are arranged in parallel to each other with an along-line shift of a half pixel size. The HSRS sensor head components of both spectral channels are based on identical technologies to provide accurate pixel co-alignment. Both spectral channels have the same optical layout but differ in the wavelength-adapted lens coatings. Figs. 5 and 6 show the HSRS flight model. The HSRS sensor was the key device of the BIRD (Bi-Spectral Infrared Detection) satellite.

6 DLR Sensor MOS IRS-P3 (1997)

The Modular Optoelectronic Scanner MOS was developed and built at DLR OS. This imaging spectrometer worked in the visible and near infrared spectral region and was especially designed for observations of relatively large scaled effects of the oceans, the atmosphere and land surface areas. MOS was launched on 21 March 1996 on board the Indian Remote Sensing Satellite IRS-P3 with the Indian Wide Field Scanner WIFS. During its operation time the MOS sensor provided spectral radiance data of the atmosphere-surface system in 18 spectral channels and up to 420 pixels in a 200 km swath from an 817 km sun synchronous polar orbit.

The international science community received a huge amount of important data for scientific use. MOS worked successfully for more than eight years in orbit.

7 KompSat3 CEU (2011-12)

KompSat3 (K3) is a project under the leadership of the Korean Space Agency KARI. The FPA has been developed by the joint teams of EADS-Astrium, BAE Systems and DLR OS. DLR OS is responsible for the FPA, front end electronics (FEE) and power design of the camera electronics unit (CEU).

The development challenge was to meet the high performances requirements of the system which has direct links to the focal plane assembly. In order to enable the design to meet

Tab. 3: K3 CEU Specification.

Key Parameters	Value
No. of Pixels PAN	24160
PAN-Sensor	2 x 12 080- plus max 64 TDI levels
Line Rate PAN	≤14 kHz
CCD Output Rate	16 x 25 MPixel/s
Data Rate	≤5.4 Gbit/s
MS-Sensor	8 x 6 040, plus max. 64 TDI levels
Line Rate MS	≤ 3.625 kHz
CCD Output Rate/ Colour	2 x 12.5 MPixel/s
Data Rate	4 x 338 Mbit/s
Pitch PAN	8.75 µm x 8.75 µm
Pitch MS	2 x 17.5 µm [binned 35 µm]
Anti Blooming	Yes
Image Plane dx, dy	220 mm, 97 mm
Dynamic Range	14 Bit
PRNU correction (photo-response non-uniformity)	Yes
DSNU correction (dark signal non-uniformity)	Yes
FPA-Flatness [z]	+/- 15 µm
SNR PAN	>100 [TDI64], 20 % albedo, 30° sun, 10:30 Seoul, SSO
SNR MS	>200 [TDI32], 20 % albedo, 30° sun, 10:30 Seoul, SSO
TDI Steps	1, 8, 32, 64
PAN	450 nm – 900 nm
NIR	760 nm – 900 nm
RED	630 nm – 690 nm
GREEN	520 nm – 600 nm
BLUE	450 nm – 520 nm

Tab. 4: K3CEU operation conditions.

Parameter	Value	Remarks
Power Interfaces	unregulated (26 … 30 VDC)	satellite power bus
Power consumption	<350 W	
Power module efficiency	>80 %	
Reliability	0.94	
Operation duty cycle	10 % / Orbit	Depends on thermal buffer
EMC	MIL-Std. 461 applicable	
FPA Mass	11 005 kg	2 x PAN + 4 x MS
Dimensions	See Figs. 9 and 10	
Operational Temperature Range	15 °C to 25 °C	Performances guaranteed
Non-Operational in-flight Temperature Range: Storage Temperature Range	0 °C to 40 °C −20 °C to 55 °C	
Radiation (total dose)	15 krad	
In-orbit lifetime	7 years	

the requirement of KARI, the design philosophy of ADS40 and RapidEye had been completely changed. Instead of using CCD line technology, TDI (time delay integration) technology was introduced. The FPA of K3 is equipped with six sensor modules (two PAN and four MS) which are completely independent. The key parameters of the K3 CEU are shown in the Tab. 3.

The FPA is able to operate under the following conditions shown in Tab. 4.

The mechanical configuration is based on a three-box philosophy. The first box contains the first stage of the power supply (CEUP). This box is used for the DC to DC converting of all different voltages and active/passive filtering of input and output voltages and the output can be controlled by the camera con-

troller. The second box (CC-Box) includes the different switching options driven by the redundancy philosophy, the camera controllers, the clock generators and the focus mechanism control (FMC). The third box contains the modular stack of all CCD line modules of the FPA.

The focal plane assembly for the KompSat3 satellite is specified as the part of the camera electronics unit which is integrated into the telescope structure, and provides the focal plane interface. The functionality of the FPA is the integration of the combined sensor system with the panchromatic and multi-spectral detectors, which includes the related electron-
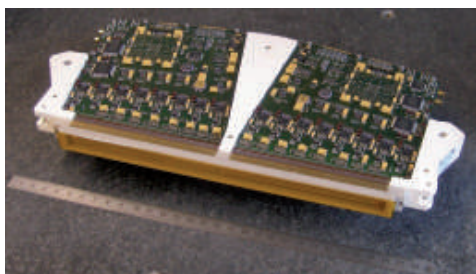
Fig. 9: K3CEU subunit Module.
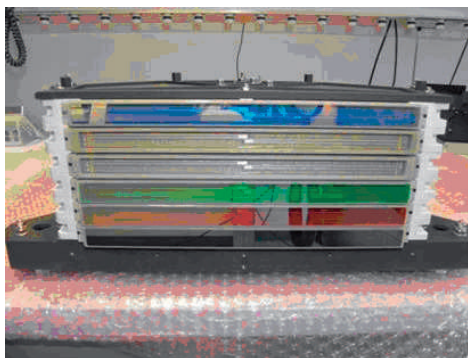
Fig. 10: K3CEU modular subunit Stack.
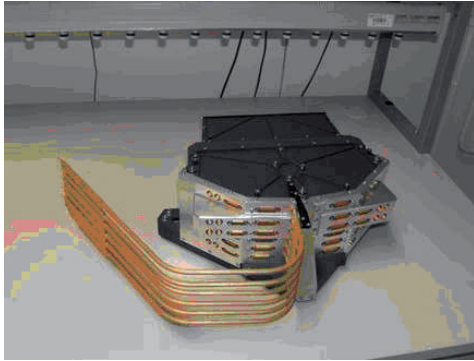
Fig. 11: Mechanical Interface of the K3CEU.

ics together with the structure for thermal management housekeeping and the mechanical interface to the telescope. To reduce the complexity of the arrangement a modular approach has been taken which is based on individual sub-units for each of the spectral channels in two forms:

(1) the 2x 12k panchromatic FPA TDI module and
(2) the 2x 6k multi spectral FPA TDI module. The design is shown in the Figs. 9 and 10.

When the CEU FPA was integrated into the telescope as a complete assembly the structure was to hold and handle the interfaces which are shown below. Here the optical interface is oriented to the Z-direction. Assuming the overall payload concept the opposite direction is oriented to the S/C outer wall where the thermal control system is located. FPA heat pipes are installed to this well defined thermal contact point, and provide a specified temperature and heat dissipation capability.

The key advantage of the current design are the free programmable line rates which are necessary to control the different scaling factors in order to realise the mission requirements and the key performances as shown in the key parameter table.

8 FPA Design Phase B1 for GMES Sentinel-4 (S4, 2010)

GMES Sentinel is a large European satellite mission. Requirements have to comply with spatial-geometrical, mechanical and thermal constraints by dedicated constructive and technological approaches designing a suitable concept for FPA assembly. Existing heritage in FPA design from ADS40, BIRD, RapidEye, TET, KompSat 3, EnMAP and MERTIS play a major role and influences the present FPA concept.

Main FPA design driving requirements can be summarized in the Tab. 5.

The appearance of high temperature gradients in optical interface can be suppressed by thermal isolation. That means existing heat flows should be reduced. Since the module of thermal conductivity and geometrical parameter as cross-section and length define the heat flow (HF) the concept must consider all of them. HF can be calculated as $HF = \lambda \times A/L$ where, λ is the thermal conductivity (material parameter), A is the cross-section (geom-

Tab. 5: S4 FPA Mechanical Specification.

Parameter	Value	Remark
Envelope	$\leq 70 \times 70 \times 80$ mm³	
Mass	≤ 0.7 kg	
Mechanical stability	≤ 1 µm	from Alignment on ground up to operation on orbit
Detector temperature	−43 °C	
Detector window temperature	+21 °C	
Telescope interface temperature	+21 °C	
Alignment	6 axes	
Alignment accuracy	axial ≤ 1 µm; lateral ≤ 5 µm	
Protection of sensor	against contamination	
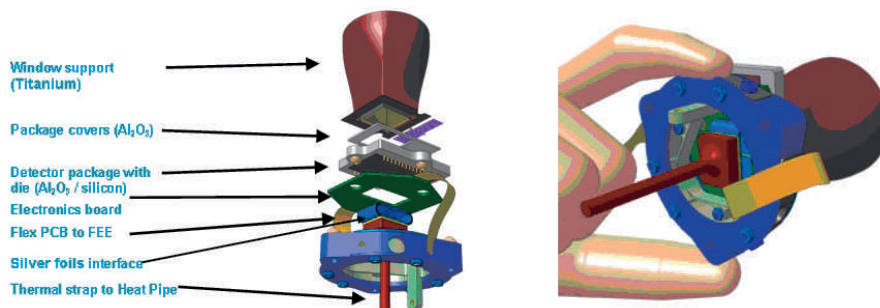
Fig. 12: Sentinel-4 FPA designexploded diagram (left) and sizes of the focal plane relative to a hand (right).

etry parameter) and L is the length (geometry parameter). The main focus of the design phase was on the mechanical design because the electronics design is well known and the pixel rate is low. But the thermal mechanical interface to the spectrometer is challenging. In order to realise this interface the optical glass and the baffle is sealed on ground and the detector is thermal controlled via a passive heatpipe system. Before launch the ventilation line system will be opened to avoid any optical distortion. Any condensation from the FPA on the launch side will be prevented by heating the system up.

9   EnMAP-VNIR-FPA (2012)

EnMAP (Environmental Mapping and Analysis Program) is a German satellite for simultaneous acquisition of high resolution hyperspectral images at visible to near infrared (420 nm – 1000 nm, VNIR) and short wave infrared (900 nm – 2450 nm, SWIR) wavelength.

DLR OS is developing the VNIR camera focal plane assembly VNIR-FPA as a subcontractor of Kayser-Threde. The key technology of the VNIR-FPA is an extremely low noise and sensitive sCMOS (scientific CMOS) detector device in back-side illumination configuration. This device is built by the OS subcon-

Tab. 6: EnMAP Key Parameters for the VNIR FPA.

Parameter	Value	Remark
Spectral channels	108	in the range from 420 nm to 1000 nm
Pixel per channel	1024	
Average band width of channel	6.5 nm	
Image rate	230 Hz	
Exposure time	4.4 ms	
Full Well Capacity (FWC)	> 1 000 000 e-/Pixel	
Read-out noise	< 200 e-/Pixel (low gain), < 70 e-/Pixel (high gain)	
Linearity error (10% - 100% FWC)	< 2 %	
Linearity error after digital correction	< 0,2 %	
Mass of sensor assembly	< 1 Kg	
Temperature stabilization	< 50 mK	
Power consumption	< 2 W	
Detector clock	252 MHz	

tractor BAE Systems. The highly integrated detector device has more than 2000 analog to digital converter and releases 13 bit high and low gain value per pixel in parallel.

The EnMAP VNIR-FPA is comprised of two mechanical units. The sensor assembly integrated into the Kayser-Threde optical unit carries the detector, the proximity electronics and a thermal control. A front end electronics box mounted outside the optics compartment provides power supply and camera control. For improved image quality a detector active thermal stabilization base on peltier element has been realized.

Key parameters of the VNIR-FPA detector are shown in Tab. 6.

The sensor assembly is built on a stiff Macor ceramics frame with a three point mounting interface to the optical unit. This provides the needed pixel registration stability for the narrow band hyperspectral mapping during space operation, and also a reliable interface for multiple mounting cycles during ground calibration and qualification procedures. The detector package has built in baffles to support stray light suppression and a tilted cover glass to prevent ghosting. Sensitive detector voltages are programmable to allow adjustment during life time if required.

The instrument power supply located in the FEE box is custom made by the company Apcon GmbH and optimized with respect to noise and stability to support the hyperspectral imager operation. The camera is controlled by a radiation tolerant re-programmable FPGA (field-programmable gate array). The main tasks of the controller are the detector control

and image acquisition, telecommand and telemetry handling, peltier control for detector temperature stabilization, digital image correlated double sampling, housekeeping data acquisition and radiation protection support (detector and FPGA scrubbing). It is possible to upload new FPGA controller designs in space via a telecommand interface.

The controller is designed by coupled state machines and provides automatic parameter checking for self-protection and error insulation. The envisaged launch of the EnMAP satellite is 2015.

10 MERTIS Imaging Spectrometer (2012)

MERTIS (MErcury Radiometer and Thermal Infrared Spectrometer) is one of the scientific payloads of the ESA deep space mission BepiColombo to Mercury. BepiColombo will be launched in 2014 to Mercury to observe the planet from 2020 on.

The MERTIS instrument design is based on a highly integrated and miniaturized concept, featuring low mass of approximately 3 kg and a sophisticated design developed by DLR OS. The specification is shown in Tab. 7.

MERTIS is an imaging spectrometer obtaining hyperspectral data in the thermal IR wavelength range with a medium spatial resolution to determine the mineralogical composition of the Mercury's surface. An un-cooled micro-bolometer array provides spectral sepa-

Fig. 13: EnMAP VNIR-FPA modules sensor assembly and front end electronics box.

Tab. 7: MERTIS Key Parameters.

Parameter	Value
Spectral range	7 – 14 μm (Spectrometer)
	7 – 40 μm (Radiometer)
Spectral resolution	80 spectral channels, 90 nm (<200 nm)
Spatial resolution	> 280 m
Swath width	> 28 km; Field of View: 4°
Mass	3,3 kg
Power	8 – 13 (19) W
Dimensions	180 x 180 x 130 mm³ (excl. Baffles)
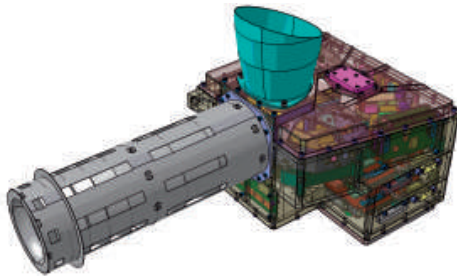
Fig. 14: MERTIS Instrument.
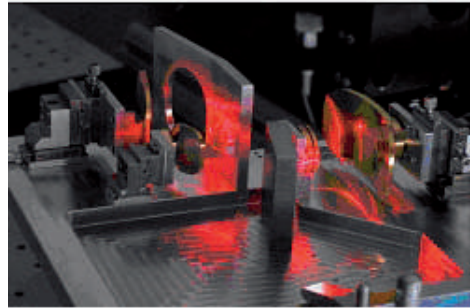
Fig. 16: MERTIS optical breadboard.

ration and spatial resolution according to its 2-dimensional shape and operates close to room temperature. Sharing the same optical path a pushbroom micro-radiometer is integrated allowing measurements of the Mercury surface temperature and obtaining the thermal inertia of the regolith.

The operation concept principle is characterized by intermediate scanning of the planet surface and 3 different calibration targets

– deep space and two on-board black body sources.

The general instrument architecture is comprised of two separate parts – the Sensor Head including optics, detectors, shutter and proximity sensor electronics and the electronics unit containing the instrument control unit, power supply as well as calibration sources. This highly integrated measurement system is complemented by a pointing/scanning device
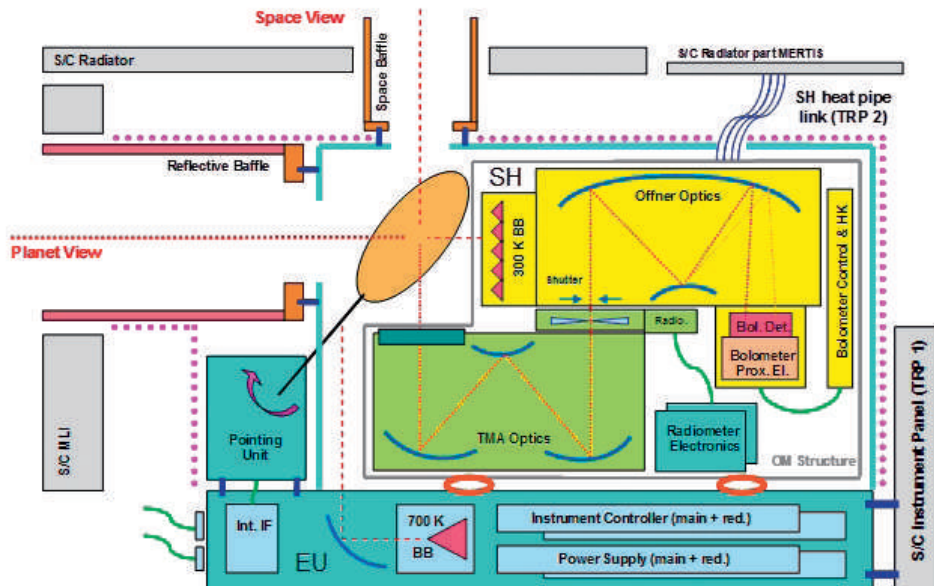
Fig. 15: MERTIS Block Diagram. S/C Radiator – space craft radiator, BB – black body, TMA – three mirror assembly, Int. IF – internal interface, EU – electronics unit, Bol. Det. – bolometer (thermal infrared) detector, Prox. El. – proximity (neighbouring) electronics, Offner Optics serving spectral decomposition.

which orients the optical path to the planet view and the calibration targets.

DLR OS develops the system design, integrates the instrument sub-units and verifies the overall performance based on laboratory investigations including instrument calibrations. The MERTIS development is done in close cooperation with scientific and industrial institutions, the Principle Investigator of the University Münster, the DLR Institute of Planetary Research in Berlin, Kayser Threde in Munich, Astrofeinwerktechnik in Berlin, the Polish Space Research Center in Warsaw and the Ingenieurbüro Ulmer in Frankfurt/Oder.

11 Summary and Outlook

The scientific objectives and the user requirements drive the performances of the whole system in particular of the focal plane. The improvement of the radiometry and the signal-to-noise ratio (SNR), the increase of the number of spectral channels and the spatial resolution (GSD), they define the technology edges of the design. In any case, the whole system shall be optimised to maintain the data product quality. The availability of new sensor technologies, e. g. CMOS back-thinning, allows the enhancement of the quantum efficiency mainly in the blue channels of the VNIR. The SNR and MTF achievable values can be met and related much more easily to the users' and scientists' performances requirements.

A software modelling system for the complete imaging chain of the digital cameras is used and continuously upgraded for design optimisation. The model incorporates the radiometry, the complete camera processing and the environmental conditions.

The next generation of detectors, new data processing capabilities and automatic data product algorithms are definitely of great interest to the work of DLR OS, and the application of on-board change detection capability will be one of our key topic focuses. The goal of applying this technology is data reduction and increase of information. This technology can be available for high resolution satellites in the next 15 years and will change the complete architecture of the ground and operation centres.

ANDREAS ECKARDT, Berlin

A Sensor-Based Approach to Image Quality

Herbert Jahn & Ralf Reulke, Berlin

Summary: In the past 20 years a large effort has been made to characterize the image quality of remote sensing systems. The image quality can actually be measured only by the quality of the final product (e. g. object detection, classification). One option now is to use the national image interpretability rating scales (NIIRS), because NIIRS is related to object detection. From an engineering standpoint a task-based scale, like NIIRS is not well suited, because it cannot be derived from the fundamental sensor and scene behaviour. Therefore, the aim of this paper is to derive an image quality criterion, based on the physical characteristics of sensor and scene. To assess the image quality, we compare the output of the real sensor with the output of an ideal sensor based on a local mean square error (LMSE). This criterion, we abbreviate in the following with IQC (image quality criterion).

Zusammenfassung: *Ein sensorbasierter Ansatz zur Bestimmung der Bildqualität.* In den letzten 20 Jahren wurde ein großer Aufwand zur Beschreibung der Qualität von Fernerkundungsbildern betrieben. Die Bildqualität kann letztlich nur durch die Beurteilung der Qualität des Endproduktes (z.B. Objektdetektion, Klassifizierung) eingeschätzt werden. Eine Möglichkeit ist die Verwendung des NIIRS (national image interpretability rating scales), da sich NIIRS auf die Objektdetektion bezieht. Vom Standpunkt des Sensorentwicklers ist NIIRS aber nicht gut geeignet, da es nicht von den grundlegenden Sensorparametern und den Szenencharakteristika abgeleitet werden kann. Deshalb wird in dieser Arbeit ein Bildqualitätskriterium vorgeschlagen, das auf diesen Größen beruht. Wir vergleichen hierzu den Output eines realen Sensors mit dem eines auf die entsprechende Aufgabe zugeschnittenen idealen Sensors mit Hilfe eines local mean square error (LMSE) Kriteriums. Dieses Kriterium kürzen wir im Folgenden mit IQC (image quality criterion) ab.

1 Introduction

For the characterization of image data or products often the spatial resolution (ground sample distance) is used which is related to detector pixel size and focal length. But there are several other influences of the imaging system that affect image sharpness and need to be considered. These other parameters are e. g. the point spread function (PSF) and signal-to-noise ratio (SNR) of the image product (Jahn & Reulke 1995). An image quality metrics can be established for any imaging system, given a characterization of the system in terms of blur and additive distortion (noise, non-linearity, compression, artefacts, preprocessing) when observing a certain scene described by its radiance. In general, image quality depends on the ultimate task of image data evaluation and cannot be defined for every image likewise. For instance, to measure star positions the quality of the deep space image is better if the image is blurred whereas the image should be sharp if objects are to be detected or recognized. Because there is not one best image quality measure here we propose an image quality criterion which is task-based and sensor-based.

To solve a definite task such as object detection or recognition in definite environment (e. g. the detection of a car in an agricultural area illuminated by solar radiation) with a space-borne sensor, that sensor will be optimized to give best performance for solving

that task (and, usually, related tasks). That means that the sensor parameters such as focal length, aperture and so on are fixed, and the illumination (in a certain range) is given too. Under these conditions an ideal sensor can be defined which gives best image quality. A real sensor which deviates more or less from the ideal one, provides worse image quality. That task-based and sensor-based approach differs from older approaches to be discussed in the following.

The most popular quantity for the description of the image quality is NIIRS. NIIRS has been developed by the imagery resolution assessments and reporting standards (IRARS) committee. It consists of different levels from 0–9. Higher values mean a capability to support a more detailed object analysis.

LEACHTENAUER et al. (1997) introduce the general image quality equation (GIQE):

$$NIIRS = 10.251 - a \cdot \log_{10} GSD + b \cdot \log_{10} RER \\ -c \cdot G/SNR - d \cdot H \quad (1)$$

GIQE is an apparent image quality (IQ) metric that measures the quality of object detection in terms of ground sample distance (GSD) and additional measures namely the relative edge response (RER), the signal-to-noise ratio (SNR), and an additional component to take care of the image restoration.

GSD is the most important factor and is related to the Nyquist frequency. Larger GSD decreases NIIRS. RER is defined as the slope immediately before and after an edge as a fraction of the edge height. A larger RER is related to a sharper point spread function (PSF) of an image and increase NIIRS. An increasing SNR results also in a decrease of the factor *G/SNR* and therefore in an increase of NIIRS. Often, before delivering the data will be modified in a preprocessing step. It includes also image enhancement algorithms. This leads to an improvement in image sharpness, but at the same time also an overshoot at the edges and an increase in noise. The gain G evaluates the noise after sharpening, and the overshoot term H measures the magnitude of ringing in the edge response of the imaging system.

Problems of applying quality metrics in remote sensing are pointed out in MIETTINEN

(2004). He introduces the 2D latent NIIRS metric based on the power spectrum of additive incoherent noise.

In the paper from KIM & PARK (2010) an image quality metric using the phase quantization code (PQC) is depiced. DUMIC et al. (2010) present an approach to the objective quality evaluation that could be computed using the mean difference between the original and tested images in different wavelet sub-bands. Wavelet coefficients are used to compute an image-quality measure (IQM). IQM is defined as perceptual weighted difference between coefficients of original and degraded image.

Image quality affects image processing results, e. g. automated classification of images. In YAN et al. (2009) a database of reference images was established that could enable automated, customized image quality modification to improve classification of new images. They introduced also a task-based definition of image quality.

GERWE et al. (2009) present a new information theoretic image quality evaluation (ITIQUE) for modelling and predicting NIIRS performance based on the visual information fidelity (VIF) IQ assessment metric. The evaluation shows a good agreement with the general image quality equation.

Image quality measure (IQM) is calculated traditionally in the image spatial domain. In the paper SHIH & FU (2008) they present a method of transforming an image into a low-dimensional domain based on random projection. From the transformed domain, it is possible to calculate the peak signal-to-noise ratio (PSNR) and apply fuzzy logic to generate a low-dimensional quality index (LDQI). The LDQI can approximate the IQM in the image spatial domain.

The paper from SCHUELER (2008) focuses on the system engineering trade-off driving almost all remote sensing design efforts, affecting complexity, cost, performance, schedule, and risk: image quality vs. sensitivity. The relationship between image quality and sensitivity is introduced based on the concepts of modulation transfer function (MTF) and signal-to-noise ratio (SNR) with examples to illustrate the balance to be achieved by the system architect to optimize cost, complexity,

performance and risk relative to end-user requirements.

CHEN et al. (2008) focus on mutual information-based quality measure and weighted averaging image fusion. Based on an image formation model, they obtain a closed-form expression for the quality measure and mathematically analyze its properties under different types of image distortion.

SHNAYDERMAN et al. (2006) present a grey-scale image quality measure that can be used to predict the influence of different noise sources, based on singular value decomposition. The measure was applied to different test images using six types of distortion (JPEG, JPEG 2000, Gaussian blur, Gaussian noise, sharpening, and DC-shifting).

An objective sensor based image quality measure has to take into account sensor specific characteristics, e. g. PSF & SNR. The approach is to compare the actual measured data with simulated image of an ideal sensor.

Therefore, in this paper we propose the usage of a new image quality criterion, namely local mean square error (LMSE), for describing the mean deviation of gray values generated by both ideal and real sensors.

This paper is organised as follows. Section 2 introduces the image quality measure, in section 3 we present some results and comparison between NIIRS and IQC and section 4 comes up with conclusions.

2 The new Image Quality Criterion

As mentioned in the introduction, here the quality of an image or the quality of the image generating sensor is assessed by comparing the output of the sensor with the output of an ideal sensor, i. e. we consider as a measure of quality a quantity $Q_{i,j}$ which is proportional to the averaged gray value deviation

$$Q_{ij} \sim \left\langle \left(G_{i,j} - G_{i,j}^{ideal} \right)^2 \right\rangle \quad (2)$$

Here, $G_{i,j}$ is the measured (i. e. noisy and blurred) gray value at pixel (i,j). The angle brackets $\langle \ldots \rangle$ denote the average of that measure over all pixels of the sensor to assess the

image as a whole or over local regions of the image. The signal generation process is explained more in detail in (JAHN & REULKE 1995).

The ideal sensor is characterized by
- given sensor parameters such as focal length, aperture, pixel size,
- no disturbances from the environment,
- no dark current,
- quantum efficiency $\eta_\lambda^{qu} = 1$ and optical transmission $\tau_\lambda^{opt} = 1$ within the considered spectral range $[\lambda_{min}, \lambda_{max}]$,
- diffraction limited optical point spread function (PSF),
- ideal pixel PSF (box shaped function),
- linear and noise free electronic channel with delta-shaped impulse response,
- analogue digital unit (ADU) with infinite small quantization step.

By definitions adopted here, images generated by that sensor have best quality at given illumination. The measure Q depends on certain sensor parameters $p_1,...,p_n$ (focal length, aperture, pixel size,…). Therefore, in principle, one could minimize the function $Q(p_1,...,p_n)$ in order to optimize the sensor, but this is not considered here.

The electron number generated in pixel (i,j) of the ideal sensor is given by

$$N_{i,j}^{ideal} = \left\langle N_{i,j}^{ideal} \right\rangle + \xi_{i,j}^{ideal} , \quad \left\langle \left(\xi_{i,j}^{ideal} \right)^2 \right\rangle = \left\langle N_{i,j}^{ideal} \right\rangle$$

$$(3)$$

$\xi_{i,j}^{ideal}$ is the noise of the signal electron number which cannot be avoided even in the ideal case. Because of the Poisson distributed photon or electron noise, the variance $\left\langle \left(\xi_{i,j}^{ideal} \right)^2 \right\rangle$ is equal to the averaged electron number $\left\langle N_{i,j}^{ideal} \right\rangle$, which can be calculated as follows:

$$\left\langle N_{i,j}^{ideal} \right\rangle = A \cdot \int_{\lambda_{min}}^{\lambda_{max}} d\lambda \cdot \lambda \cdot L_\lambda^{ideal} \left(x_i, y_j \right)$$

$$\left(A = \frac{\pi}{4} \cdot \frac{1}{f_\#^2} \cdot F_{pix} \cdot t_{int} \cdot \frac{1}{h \cdot c} \right) \quad (4)$$

with $f_\#$ = f-number of optics, F_{pix} = pixel area, t_{int} = illumination (integration) time, h =

Planck's constant, c = speed of light in vacuum.

Furthermore

$$L_\lambda^{ideal}\left(x_i, y_j\right) = \iint dx dy\, H_\lambda^{ideal}\left(x_i - x, y_j - y\right) \cdot L_\lambda'\left(x, y\right) \quad (5)$$

Here, $L_\lambda'\left(x, y\right)$ is the radiance in front of the sensor. H_λ^{ideal} is the point spread function (PSF) of the whole imaging system. The quality measure is defined with respect to that radiance. The generated electrons or charges $\left\langle N_{i,j}^{ideal} \right\rangle$ will be changed at the pn-junction of the photodiode into an electrical voltage. Let $U_{i,j}$ be the voltage in front of the ADU. Then we have with eq. 3

$$U_{i,j}^{ideal} = \alpha \cdot N_{i,j}^{ideal} = \alpha \cdot \left\langle N_{i,j}^{ideal}\right\rangle + \alpha \cdot \xi_{i,j}^{ideal} \quad (6)$$

The multiplier α is given by $\alpha = U_{max} / N_{sat}$ with U_{max} the maximal ADU input voltage and N_{sat} the saturation electron number. The gray values $G_{i,j}$ (output of ideal sensor) are given by

$$G_{i,j}^{ideal} = U_{i,j}^{ideal} \quad (7)$$

and we obtain from eqs. 4, 5, 6, and 7

$$G_{i,j}^{ideal} = \alpha \cdot A \cdot \int_{\lambda_{min}}^{\lambda_{max}} d\lambda \cdot \lambda$$
$$\cdot \iint dx dy\, H_\lambda^{ideal}\left(x_i - x, y_j - y\right) \cdot L_\lambda'\left(x, y\right)$$
$$+ \alpha \cdot \xi_{i,j}^{ideal} \quad (8)$$

Now we consider the real imaging sensor. As in eq. 3 we obtain the electron numbers $N_{i,j} = \left\langle N_{i,j}\right\rangle + \xi_{i,j}^{el}$ with

$$\left\langle N_{i,j}\right\rangle = A \cdot \int_{\lambda_{min}}^{\lambda_{max}} d\lambda \cdot \lambda \cdot \tau_{\lambda,i,j}$$
$$\cdot \iint dx dy\, H_\lambda\left(x_i - x, y_j - y\right) \cdot L_\lambda'\left(x, y\right)$$
$$+ \left\langle N_{i,j}^{D+U}\right\rangle$$
$$\left(\tau_{\lambda,i,j} = \tau_{\lambda,i,j}^{opt} \cdot \eta_{\lambda,i,j}^{qu}\right), \quad \left\langle \left(\xi_{i,j}^{el}\right)^2\right\rangle = \left\langle N_{i,j}\right\rangle \quad (9)$$

Here, $\left\langle N_{i,j}^{D+U}\right\rangle$ is the mean electron number in pixel (i,j) generated by dark current and environment (e. g. radiation of instrument parts in infrared). $\tau_{\lambda,i,j}^{opt}$ is the (optical) transmission and $\eta_{\lambda,i,j}^{qu}$ the quantum efficiency. The conversion of electrons in voltages U now is in differ-

ence to the ideal sensor (see eq. 6) non-linear with an additional noise:

$$U_{i,j} = f\left(N_{i,j}\right) + \xi_{i,j}^K = f\left(\left\langle N_{i,j}\right\rangle + \xi_{i,j}^{el}\right) + \xi_{i,j}^K \quad (10)$$

$\xi_{i,j}^K$ with variance $\sigma_K^2 = \left\langle \left(\xi_{i,j}^K\right)^2\right\rangle$ is the noise of the read-out channel (which was neglected for the ideal sensor in eq. 6).

Here we consider the case that the conversion characteristic $f(N)$ of the read-out channel only differs marginally from linearity. These characteristics include the three noise-components photon noise, dark current, and the read- or read-out noise. So, the expression in eq. 10 can be developed in a Taylor series and truncated after the first term:

$$f\left(N_{i,j}\right) = \alpha \cdot N_{i,j} + \delta f\left(N_{i,j}\right),$$
$$\left|\delta f\left(N_{i,j}\right)\right| << \alpha \cdot N_{i,j} \quad (11)$$

Then based on eqs. 10 and 11 it approximately holds that

$$f\left(\left\langle N_{i,j}\right\rangle + \xi_{i,j}^{el}\right) \approx \alpha \cdot \left[\left\langle N_{i,j}\right\rangle + \xi_{i,j}^{el}\right] + \delta f\left(\left\langle N_{i,j}\right\rangle\right) \quad (12)$$

and using eq. 10 leads to

$$U_{i,j} \approx \alpha \cdot \left\langle N_{i,j}\right\rangle + \delta f\left(\left\langle N_{i,j}\right\rangle\right) + \xi_{i,j}$$
$$\left(\xi_{i,j} = \alpha \cdot \xi_{i,j}^{el} + \xi_{i,j}^K\right) \quad (13)$$

Now we consider the ADU: $[0, U_{max}]$ is the range of the input signal. That range is represented by $M = 2^n$ gray value steps (n bits). Let Δ be the quantization step, i. e. $\Delta = U_{max} / M$. The non-linearity of analogue to digital conversion then is described by $G = g\left(U\right)$ with

$$g\left(U\right) = \left[\frac{U}{\Delta} + 0.5\right] \cdot \Delta \quad (14)$$

Here, [x] is the integer part of the real number x. We remember that in the ideal case $g^{ideal}\left(U\right) = U$ holds.

For each real number $z > 0$ the inequality $0 \leq z - \left[z\right] < 1$ is true. Then the ADU error is confined to $-0.5 \cdot \Delta < g\left(u\right) - U < 0.5 \cdot \Delta$. We interpret the error $g\left(U\right) - U$ as ADU noise

ξ^{ADU} and assume a uniform distribution in $-0.5 \cdot \Delta < \xi^{ADU} < 0.5 \cdot \Delta$. Then, we get as a result of a rectangular distribution (JÄHNE 2005)

$$\langle \xi^{ADU} \rangle = 0 \,, \quad \left\langle \left(\xi^{ADU} \right)^2 \right\rangle = \sigma_{ADU}^2 = \frac{\Delta^2}{12} \qquad (15)$$

Using eq. 13 and considering that $G_{i,j} = g\left(U_{i,j}\right)$ describes the analog-to-digital conversion of real sensors, the gray values of the real sensor are given by

$$\begin{aligned} G_{i,j} &= g\left(U_{i,j}\right) = g\left(\langle U_{i,j} \rangle + \xi_{i,j}\right) \\ &\approx g\left(\alpha \cdot \langle N_{i,j} \rangle + \delta f\left(\langle N_{i,j} \rangle\right) + \alpha \cdot \xi_{i,j}^{el} + \xi_{i,j}^{K}\right) \\ &= \alpha \cdot \langle N_{i,j} \rangle + \delta f\left(\langle N_{i,j} \rangle\right) + \alpha \cdot \xi_{i,j}^{el} + \xi_{i,j}^{K} \\ &\quad + \xi_{i,j}^{ADU} \end{aligned} \qquad (16)$$

We now consider the quality measure $\left\langle \left(G_{i,j} - G_{i,j}^{ideal} \right)^2 \right\rangle$: According to eqs. 3, 6, 7 and 16, and using an approximation of eqs. 11 and 16 we obtain

$$\begin{aligned} G_{i,j} - G_{i,j}^{ideal} &\approx \alpha \cdot \left(\langle N_{i,j} \rangle - \langle N_{i,j}^{ideal} \rangle \right) \\ &\quad + \delta f\left(\langle N_{i,j} \rangle\right) + \alpha \cdot \left(\xi_{i,j}^{el} - \xi_{i,j}^{ideal}\right) \\ &\quad + \xi_{i,j}^{K} + \xi_{i,j}^{ADU} \\ &\approx \alpha \cdot \left(\langle N_{i,j} \rangle - \langle N_{i,j}^{ideal} \rangle \right) \\ &\quad + \delta f\left(\langle N_{i,j}^{ideal} \rangle\right) + \alpha \cdot \left(\xi_{i,j}^{el} - \xi_{i,j}^{ideal}\right) \\ &\quad + \xi_{i,j}^{K} + \xi_{i,j}^{ADU} \end{aligned}$$

and

$$\begin{aligned} &\left\langle \left(G_{i,j} - G_{i,j}^{ideal} \right)^2 \right\rangle \\ &\approx \left[\alpha \cdot \left(\langle N_{i,j} \rangle - \langle N_{i,j}^{ideal} \rangle \right) + \delta f\left(\langle N_{i,j}^{ideal} \rangle\right) \right]^2 \\ &\quad + \alpha^2 \cdot \left\langle \left(\xi_{i,j}^{el} - \xi_{i,j}^{ideal} \right)^2 \right\rangle + \sigma_K^2 + \sigma_{ADU}^2 \end{aligned} \qquad (17)$$

The linear components are removed, because we assume that the different noise components are uncorrelated and the average of noise and signal components (e. g. $\left\langle \langle N_{i,j} \rangle \cdot \xi_{i,j}^{el} \right\rangle$) vanish.

Using $\Delta = \alpha \cdot \dfrac{N_{sat}}{2^n}$ and the variance of a rectangular distribution $\sigma_{ADU}^2 = \dfrac{1}{12} \cdot 2^{-2n}$ we can introduce the normalized quality measure

$$\begin{aligned} Q_{i,j} &= \frac{\left\langle \left(G_{i,j} - G_{i,j}^{ideal} \right)^2 \right\rangle}{\left(\alpha \cdot N_{sat} \right)^2} \\ &\approx \left[\frac{\left(\langle N_{i,j} \rangle - \langle N_{i,j}^{ideal} \rangle \right)}{N_{sat}} + \frac{\delta f\left(\langle N_{i,j}^{ideal} \rangle\right)}{\alpha \cdot N_{sat}} \right]^2 \\ &\quad + \frac{\left\langle \left(\xi_{i,j}^{el} - \xi_{i,j}^{ideal} \right)^2 \right\rangle}{N_{sat}^2} + \frac{\sigma_K^2}{\left(\alpha \cdot N_{sat} \right)^2} + \frac{1}{12} \cdot 2^{-2n} \end{aligned}$$
$$(18)$$

Now we discuss the measure $Q_{i,j}$ in more detail: The eq. 18 consists of deterministic and noise terms. The first two terms are deterministic. The contribution to $Q_{i,j}$ is the deviation $F_{i,j}^{(1)} = \langle N_{i,j} \rangle - \langle N_{i,j}^{ideal} \rangle$ of mean electron numbers.

The following equations until and including eq. 24 regard the nominators only because the denominator can in this context be considered as constant.

According to eqs. 4, 8 and 9 we obtain

$$\begin{aligned} F_{i,j}^{(1)} &= A \cdot \int_{\lambda_{\min}}^{\lambda_{\max}} d\lambda \cdot \lambda \\ &\quad \cdot \iint dx dy \left[\tau_{\lambda,i,j} \cdot H_\lambda\left(x_i - x, y_j - y\right) - H_\lambda^{ideal}\left(x_i - x, y_j - y\right) \right] \\ &\quad \cdot L_\lambda'\left(x, y\right) + \langle N_{i,j}^{D+U} \rangle \end{aligned}$$

Introducing the deviation $\delta\tau_{\lambda,i,j} = 1 - \tau_{\lambda,i,j}$ from the ideal case $\tau = 1$ ($\tau = \tau^{opt} \cdot \eta^{qu}$) we can write

$$\begin{aligned} F_{i,j}^{(1)} &= A \cdot \int_{\lambda_{\min}}^{\lambda_{\max}} d\lambda \cdot \lambda \\ &\quad \cdot \iint dx dy \left[H_\lambda\left(x_i - x, y_j - y\right) - H_\lambda^{ideal}\left(x_i - x, y_j - y\right) \right] \\ &\quad \cdot L_\lambda'\left(x, y\right) - A \cdot \int_{\lambda_{\min}}^{\lambda_{\max}} d\lambda \cdot \lambda \\ &\quad \cdot \iint dx dy \, \delta\tau_{\lambda,i,j} \cdot H_\lambda\left(x_i - x, y_j - y\right) \cdot L_\lambda'\left(x, y\right) \\ &\quad + \langle N_{i,j}^{D+U} \rangle \end{aligned} \qquad (19)$$

Here, the first term characterizes the PSF error, whereas the second summand is generated by deviations of optical transmission and quantum efficiency from ideal values. $\langle N_{i,j}^{D+U} \rangle$ describes the contribution from dark current and non-signal radiation. The PSF-error

$$F_{i,j}^{PSF} = A \cdot \int\limits_{\lambda_{\min}}^{\lambda_{\max}} d\lambda \cdot \lambda$$
$$\cdot \iint dxdy \left[H_\lambda \left(x_i - x, y_j - y \right) - H_\lambda^{ideal} \left(x_i - x, y_j - y \right) \right]$$
$$\cdot L'_\lambda (x,y) \tag{20}$$

strongly depends on the radiance $L'_\lambda(x,y)$ of the observed scene. In particular, it vanishes if the radiance does not depend on the spatial coordinates *x,y* (homogeneous scene). Therefore, there is no signal-independent quality measure. It must be related to a spatial scene or at least to a certain class of radiances describing background and objects.

$F_{i,j}^{PSF}$ also can be expressed in the spatial frequency domain:

$$F_{i,j}^{PSF} =$$
$$A \cdot \int\limits_{\lambda_{\min}}^{\lambda_{\max}} d\lambda \cdot \lambda \cdot \iint dk_x dk_y \left[\tilde{H}_\lambda \left(k_x, k_y \right) - H_\lambda^{ideal} \left(k_x, k_y \right) \right]$$
$$\cdot \tilde{L}'_\lambda \left(k_x, k_y \right) \cdot e^{i \cdot 2\pi \left(k_x \cdot x_i + k_y \cdot y_j \right)} \tag{21}$$

Here, $\tilde{H}_\lambda \left(k_x, k_y \right)$, $\tilde{L}'_\lambda \left(k_x, k_y \right)$ are the optical transfer function (OTF) and the 2D-Fourier transform of the radiance, respectively.

Sometimes quality measures use the OTF (or MTF) at Nyquist frequency. But generally the whole OTF function is necessary to express image quality correctly. Only under special assumptions concerning the radiance $L'_\lambda(x,y)$ or its Fourier transform $\tilde{L}'_\lambda \left(k_x, k_y \right)$ (eq. 21) can it be approximated to depend only on $\tilde{H}_\lambda \left(k_x, k_y \right)$ and $\tilde{L}'_\lambda \left(k_x, k_y \right)$ at the Nyquist frequency.

The transmission error (second term in eq. 19)

$$F_{i,j}^\tau = -A \cdot \int\limits_{\lambda_{\min}}^{\lambda_{\max}} d\lambda \cdot \lambda$$
$$\cdot \iint dxdy \, \delta\tau_{\lambda,i,j} \cdot H_\lambda \left(x_i - x, y_j - y \right)$$
$$\cdot L'_\lambda (x,y)$$

can be written approximately as

$$F_{i,j}^\tau = -A \cdot r \left(x_i, y_j \right) \cdot \int\limits_{\lambda_{\min}}^{\lambda_{\max}} d\lambda \cdot \lambda \cdot S_\lambda \cdot \delta\tau_{\lambda,i,j} \tag{22}$$

For estimation $L'_\lambda(x,y)$ was factorized in $r \left(x_i, y_j \right)$ a wavelength-independent reflectance and S_λ the spectral dependent radiance

term. The OTF at Nyquist frequency is also integrated in S_λ.

Therefore, the image quality contribution $F_{i,j}^{(1)} = F_{i,j}^{PSF} + F_{i,j}^\tau + \left\langle N_{i,j}^{D+U} \right\rangle$ can be estimated easily.

The second contribution to $Q_{i,j}$ (eq. 18) $F_{i,j}^{(2)} = \delta f \left(\left\langle N_{i,j}^{ideal} \right\rangle \right)$ describes the deterioration of image quality by the non-linearity of the electronic channel (read out circuit). If the non-linearity is weak (fulfilled for most CCD devices), the function $f(N)$ (eq. 11) can be approximated by

$$f \left(N_{ij} \right) = \alpha \cdot N_{ij} - \beta \cdot N_{ij}^2 \, ,$$
$$\delta f \left(N_{ij} \right) = -\beta \cdot N_{ij}^2 \quad \left(\beta \cdot N_{sat} << \alpha \right) \tag{23}$$

Using the approximation
$$\left\langle N_{i,j}^{ideal} \right\rangle \approx A \cdot \int\limits_{\lambda_{\min}}^{\lambda_{\max}} d\lambda \cdot \lambda \cdot S_\lambda \cdot r \left(x_i, y_j \right) \text{ we obtain}$$

$$F_{i,j}^{(2)} = -\beta \cdot \left\langle N_{i,j}^{ideal} \right\rangle^2 \tag{24}$$

Now, the systematic part of the quality measure (eq. 18) can be written as

$$Q_{i,j}^{syst} = \left[\frac{\left(\left\langle N_{i,j} \right\rangle - \left\langle N_{i,j}^{ideal} \right\rangle \right)}{N_{sat}} + \frac{\delta f \left(\left\langle N_{i,j}^{ideal} \right\rangle \right)}{\alpha \cdot N_{sat}} \right]^2$$
$$\approx \left[\frac{F_{i,j}^{(1)}}{N_{sat}} + \frac{F_{i,j}^{(2)}}{\alpha \cdot N_{sat}} \right]^2 \tag{25}$$

Now we consider the contribution of noise to the quality measure (eq. 18):

Using the formulas eqs. 3 and 9
$$\left\langle \left(\xi_{i,j}^{el} \right)^2 \right\rangle = \left\langle N_{i,j} \right\rangle, \quad \left\langle \left(\xi_{i,j}^{ideal} \right)^2 \right\rangle = \left\langle N_{i,j}^{ideal} \right\rangle ,$$
the part $F_{i,j}^{(3)} = \left\langle \left(\xi_{i,j}^{el} - \xi_{i,j}^{el,ideal} \right)^2 \right\rangle$ is given by

$$F_{i,j}^{(3)} = \left| \left\langle N_{i,j} \right\rangle - \left\langle N_{i,j}^{ideal} \right\rangle \right| = \left| F_{i,j}^{(1)} \right|, \text{ and we obtain}$$

$$Q_{i,j}^{noise} = \frac{\left| F_{i,j}^{(1)} \right|}{N_{sat}^2} + \frac{\sigma_K^2}{\left(\alpha \cdot N_{sat} \right)^2} + \frac{1}{12} \cdot 2^{-2n} \tag{26}$$

The formulas eqs. 25 and 26 allow the estimation of the systematic and random contributions to the image quality measure $Q_{i,j}$ in every pixel (*i,j*). To obtain a more global measure characterising the whole image, $Q_{i,j}$ can be averaged over all pixels of the image.

3   Results and Discussion

In order to assess the developed method we compare simulated image data with parameters from real data. We evaluate these data in the vicinity of an edge. The mean gray value there is 176. With the standard deviation $\sigma = 1.4$ we have a signal-to-noise ratio of about 125 (green channel). The sensor is characterized by $N_{sat} = 300,000$, $U_{max} = 1$ V. Then, the mean electron number (without PSF) is $\langle N \rangle = \langle N^{ideal} \rangle \approx 207,000$. The PSF is assumed as a Gaussian with standard deviation σ_{PSF}. Fig. 1 (left) shows the mean electron numbers $\langle N_{PSF}^{ideal} \rangle$ and $\langle N_{PSF}^{real} \rangle$ for $\sigma_{PSF}^{real} = 5 \cdot \sigma_{PSF}^{ideal}$

Here, we study only the influence of the PSF to the image quality. Therefore, only the contribution

$$Q_i^{syst} = \left[\frac{\left(\langle N_i \rangle - \langle N_i^{ideal} \rangle \right)}{N_{sat}} \right]^2 \quad \text{is considered.}$$

$Q_i^{noise} = \dfrac{\left| \langle N_i \rangle - \langle N_i^{ideal} \rangle \right|}{N_{sat}^2}$ shows the same be-

haviour, but is much smaller and therefore is not investigated here.

Fig. 1 (right) displays the function Q_i^{syst} for the case $\sigma_{PSF}^{real} = 5 \cdot \sigma_{PSF}^{ideal}$.

As it must be, $Q_i^{syst} = 0$ holds in the homogeneous image region whereas the quality near the edge is worse because of the PSF caused blur. Tab. 1 shows the dependence of $\max\{Q_i^{syst}\}$ from the parameter $\sigma_{PSF}^{real} / \sigma_{PSF}^{ideal}$.

Of course, with increasing parameter $\sigma_{PSF}^{real} / \sigma_{PSF}^{ideal}$ also the area around the edge with worse image quality increases which is not taken into account in Tab. 1.

Tab. 1: Quality in dependence of $\sigma_{PSF}^{real} / \sigma_{PSF}^{ideal}$.

$\sigma_{PSF}^{real} / \sigma_{PSF}^{ideal}$	$\max\{Q_i^{syst}\} \cdot 10^4$
1	0.0
2	1.3
3	2.9
4	4.1
5	4.9
…	
10	7.2

For comparison the IQC with NIIRS we investigate an IKONOS image (green channel) from Dresden. For images in a usual dynamic range the Poisson distributed photon noise dominates and again dark and read-out noise will be neglected here. Only the PSF and additional components from pre-processing influence the image quality. Fig. 2 (right) shows the comparison between the image quality measure and traditional NIIRS. This plot is a result of changing $\sigma_{PSF}^{real} / \sigma_{PSF}^{ideal}$ relation as seen in Tab. 1. The plot shows a linear part for $IQ \geq 10^{-4}$ (image quality, relative measure, no unit). This is equivalent with the results from (JONES 2004). He calculated for IKONOS with an average GSD = 0.93 m an average NIIRS 4.49 ± 0.19.

The parameter PSF and SNR are evaluated from the real image data. The PSF or RER was calculated from image edges (edge spread function - ESF), the SNR was derived from homogeneous areas in the images. The SNR
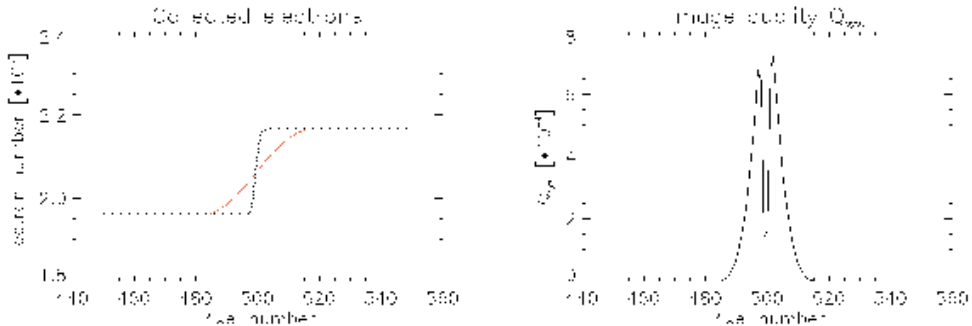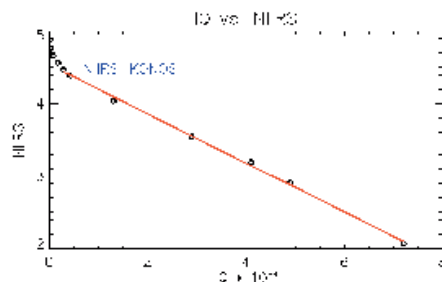

Fig. 1: Electron number (dashed line: electron number for the ideal case) and resulting function Q_i^{syst} (right).

Fig. 2: Test case IKONOS image acquired at 8.7.2007 (left) and comparison with NIIRS.

in the considered region is 125 with a mean of 175 (in digital numbers) and a standard deviation of 1.4. The RER (σ_{PSF}^{real}) is 0.55 (1.25). The resulting NIIRS corresponds to the results from Jones (2004).

Remarkable is the non-linear increase below $IQ < 10^{-4}$. It shows also the potential for further improvement of the sensor.

4 Conclusion and Outlook

In this paper a sensor based method for calculation image quality was proposed. It is based on the consideration of the deviation of an ideal sensor to a real one, using sensor-specific parameters.

Experimental results show that the proposed method is consistent with the subjective quality score such as NIIRS. The key advantage of the new criterion is that it can be derived directly from the sensor parameters. In addition, artefacts may be detected directly (from the deviation to the ideal sensor). The potential for the improvement of the sensor can be deduced also by comparison with the ideal sensor.

To conclude, the development of a concept for image quality will require an in-depth analysis of the imaging system, as well as a careful analysis of the definitions for quality. It must be checked for further studies, whether an ideal sensor should be described by a delta function PSF and without photon noise.

References

Chen, Y., Xue, Z.Y. & Blum, S., 2008: Theoretical analysis of an information-based quality measure for image fusion. – Information Fusion **9** (2): 161–175.

Dumic, E., Grgic, S. & Grgic, M., 2010: New image-quality measure based on wavelets. – Journal of Electronic Imaging **19** (1): Article ID 011018.

Gerwe, D., Carlos, E.L. & Brandoch, C., 2009: Information Theoretic Based Image Quality Evaluation. – Proceedings Signal Recovery and Synthesis: STuC1.

Jähne, B., 2005: Digital Image Processing. – **6th** revised and extended edition, 253, Springer, Berlin.

Jahn, H. & Reulke, R., 1995: Systemtheoretische Grundlagen optoelektronischer Sensoren. – 298, Akademie Verlag, Berlin.

Jones, E.C., 2004: Image Quality Evaluation of QuickBird Super Resolution and Revisit of IKONOS. – Civil and Commercial Application Project (CCAP). – http://calval.cr.usgs.gov/JACIE_files/JACIE04/files/1Jones12.pdf (1.10.2011)

Kim, D.O. & Park, R.H., 2010: Image Quality Measure Using the Phase Quantization Code. – IEEE Transactions on Consumer Electronics **56** (2): 937–945.

Leachtenauer, J.C., Malila, W., Irvine, J., Colburn, L. & Salvaggio, N., 1997: General Image-Quality Equation: GIQE. – Applied Optics **36** (32): 8322–8328.

Miettinen, K., 2004: Application of Image Quality Metrics to Problems in Remote Sensing System Design. – Visual Information Processing XIII **5438:** 150–158.

Schueler, C.F., 2008: Image Quality vs. Sensitivity: Fundamental Sensor System Engineering – art. no. 708708. – Remote Sensing System Engineering **7087:** 8708–8708.

SHIH, F.Y. & FU, Y.Y., 2008: Approximate Image Quality Measure in Low-Dimensional Domain Based on Random Projection. – International Journal of Pattern Recognition and Artificial Intelligence **22** (2): 335–345.

SHNAYDERMAN, A., GUSEV, A. & ESKICIOGLU, A.M., 2006: An SVD-Based Grayscale Image Quality Measure for Local and Global Assessment. – IEEE Transactions on Image Processing **15** (2): 422–429.

YAN, S., SAYAD, S. & BALKE, S.T., 2009: Image Quality in Image Classification: Design and Construction of an Image Quality Database. – Computers & Chemical Engineering **33** (2): 421–428.

Addresses of the Authors:

Prof. Dr. HERBERT JAHN, DLR German Aerospace Center, Department of Optical Information Systems at the Institute of Robotics and Mechatronics, Rutherfordstrasse 2, D-12489 Berlin, Germany, Tel.: +49-30-67055-510, Fax: +49-30-67055-385, e-mail: herbert.jahn@dlr.de

Prof. Dr. RALF REULKE, Humboldt-Universität zu Berlin, Institut für Informatik, Computer Vision, Unter den Linden 6, 10099 Berlin, Germany, e-mail: reulke@informatik.hu-berlin.de

SNR Evaluation of the RapidEye Space-borne Cameras

Ralf Reulke, DLR, Berlin & Horst Weichelt, RapidEye, Brandenburg

Summary: After launch and during continuous radiation exposure, space-borne cameras are constantly changing. Therefore, permanent technical determination and evaluation of the sensor in space plays an important role in the remote sensing community. There are a variety of evaluation criteria, which are all based on the essential camera parameters – the spatial resolution, point spread function (PSF) and noise.

Noise estimation is a challenging task for characterization of remote sensing systems in space. The in-flight measurement of noise will often be done with artificial test sites. If these test sites are not sufficiently available, homogeneous image regions (desert, snow, water surfaces) are often used. The albedo of these regions, however, lies normally outside the specified albedo range of remote sensing systems focused on agriculture and forestry areas. The only possibility to determine the noise after the satellite launch within the specified operational albedo range is to use very small image areas with the required albedo within the acquired imagery. As these objects have to be homogeneous, one needs methods that can detect the smallest homogeneous areas in the image to evaluate noise.

In this paper an approach for determining the signal-to-noise ratio (SNR) with data from natural targets is presented. In experiments, the results demonstrate that the described method performs quite satisfactorily and results are comparable to the standard methods used to determine SNR.

Zusammenfassung: *SNR Bestimmung der RapidEye Weltraumkameras*. Durch den Start und die kontinuierliche Strahlenbelastung verändern sich Weltraumkameras laufend. Deshalb ist die ständige Spezifizierung und Bewertung solcher Sensoren von eminenter Bedeutung in der Fernerkundung. Es gibt eine Vielzahl von Bewertungskriterien, die auf den wesentlichen Parametern einer Kamera basieren – die räumliche Auflösung, die Punktbildverwaschungsfunktion (PSF) und das Rauschen.

Die quantitative Bestimmung des Rauschens aus Daten von Weltraumkameras ist eine anspruchsvolle Aufgabe. In-flight Messungen des Rauschens werden oft anhand künstlicher Testflächen durchgeführt. Wenn diese nicht ausreichend zur Verfügung stehen, verwendet man normalerweise homogene Bildbereiche (Wüste, Schnee, Wasseroberflächen). Diese sind jedoch außerhalb des Albedobereichs von interessanten Gebieten, die üblicherweise mittels Fernerkundungssystemen untersucht werden. Für das Fernerkundungssystem RapidEye sind das zum Beispiel landwirtschaftliche Gebiete und Forsten. Um das Rauschen nach dem Satellitenstart im spezifizierten operationellen Albedobereich zu bestimmen, ist es erforderlich, die Auswertung in diesen Bildregionen durchzuführen. Deshalb braucht man Methoden, die kleinste homogene Bereiche im Bild erkennen und bezüglich des Rauschens auswerten können.

In diesem Artikel wird ein Konzept für die Bestimmung des Signal-Rausch-Verhältnisses (SNR) aus Daten natürlicher Szenen vorgeschlagen. Untersuchungen zeigen, dass das Verfahren zufriedenstellend arbeitet und die Ergebnisse mit den konventionellen Verfahren vergleichbar sind.

1 Introduction

Calibration, verification and validation of remote sensing systems are the most challenging procedures after completion of the sensor.

Using the sensor calibration, radiometric and geometric correction of the image data is possible. At the same time, the relationship between gray values and radiance is established.

The same data set is also used for determining the quality of the data products and the sensor.

The determination and evaluation of the performance of optical remote sensing systems is usually done on the basis of fundamental camera parameters. Some of these parameters can change over the lifetime of the sensor and therefore should be checked regularly at specified time intervals after the launch.

In recent years, there have been a variety of activities and publications focused on the geometric and radiometric validation of airborne cameras by EuroSDR (CRAMER 2008) and DIN-standards (REULKE et al. 2007).

This paper discusses the characterization of signal-to-noise ratio (SNR) values based on real image data from the RapidEye cameras. The RapidEye camera is a digital pushbroom scanner with 5 spectral bands in the visible and near infrared range. The focal plane was designed by the DLR Institute of Robotics and Mechatronics in Berlin-Adlershof. Each of the 5 detector lines contains 12,000 pixels and sensor elements, respectively. The radiometric dynamic depth of the camera is nominally 12-bit, with A/D conversion of 14-bit. The radiometric calibration for the defined operating point of the cameras is slightly different for the different spectral bands; the corresponding spectral radiance values are between 41 and 88 $W/m^2/sr/\mu m$. The cameras were built by Jena Optronic in Thuringia. Fig. 1 shows a schematic drawing of the camera structure.

Section 2 presents a short summary of previous papers on the topic of sensor characterization, while in section 3 we explain and discuss our approach. Our results are presented in section 4. In the last section we draw some conclusions.

2 Noise Measurement over Homogeneous and Non-Homogeneous Targets

Let us start by assuming a linear imaging system with a zero-mean white Gaussian random noise that is additive and uncorrelated to the signal. Consider the 2D-problem
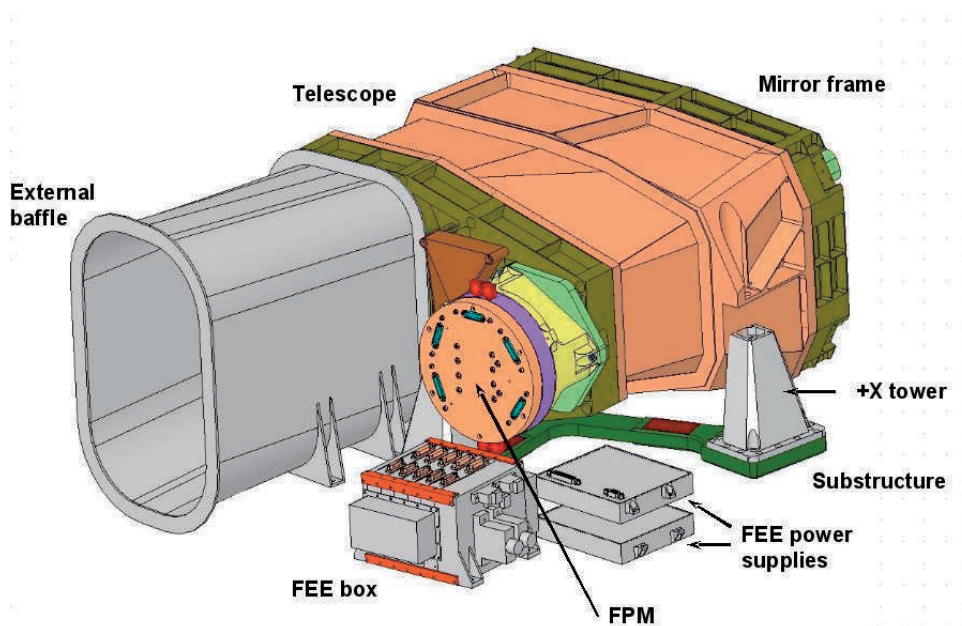

Fig. 1: RapidEye camera architecture and layout (FEE – front end electronic, FPM – focal plane module, +X tower – sensor suspension).

$$y(z_1,z_2) = \iint dz_1' dz_2' H(z_1 - z_1', z_2 - z_2') \cdot x(z_1',z_2')$$
$$+ \xi(z_1,z_2) \qquad (1)$$

$H(z_1,z_2)$ is the space invariant point spread function (PSF), $y(z_1,z_2)=y(i\Delta,j\Delta)$ is the sampled measurement (gray) values of the scene $x(z_1',z_2')$ on pixel position $(i\Delta,j\Delta)$ (Δ is the distance between pixels) and ξ the noise of the imaging system. $\xi(z_1,z_2) = \xi(i\Delta,j\Delta)$ are uncorrelated random numbers with zero expectation values:

$$\langle \xi_{i,j} \rangle = 0, \quad \langle \xi_{i,j} \cdot \xi_{k,l} \rangle = \sigma^2 \cdot \delta_{i,k} \cdot \delta_{j,l} \qquad (2)$$

The scene can also be supposed to be a stationary random process.

In this paper three different noise components will be taken into account: Dark noise, read noise and shot noise. For an overview about different noise sources in CCD-detectors see e. g. JANESICK (2001). The Poisson distributed dark current noise is a parasitic photocurrent in the absence of any illumination on the device, under specified operating conditions (temperature, integration time and bias). Read noise is defined as the temporal system noise of the focal plane assembly (FPA) in darkness. The Poisson distributed shot noise refers to the inherent natural variation of the incident photon flux. Because of the Poisson behaviour, this noise is signal dependent.

An overview about methods for noise estimation is given in LUO & ZHONG (2009). The homogeneous area (HA) method estimates the SNR of the image by the ratio of the mean to the standard deviation of manually selected homogeneous areas. The local means and local standard deviations (LMLSD) method automatically estimates the noise by dividing the image into many homogeneous blocks. Other methods for determining the SNR are the residual-scaled local standard deviations (RLSD) method and spectral as well as spatial decorrelation (SSDC) method (LUO & ZHONG 2009). For the purposes of our discussion the HA and the LMLSD should be explained more in detail.

The noise determination by the HA method requires an image containing a uniform and homogeneous surface such as a snow field of Greenland or a large homogeneous desert area.

As noise is signal dependent, it has to be determined separately for different signal levels. Unfortunately, most of the homogeneous surfaces mentioned above are very bright and are almost outside the radiometric range for normal operations of the sensor. In addition, systematic noise sources are superimposed to the random noise. Such systematic noise sources could be for instance micro-textures from the observed surface and a not sufficiently corrected PRNU (photo response non-uniformity) in CCD-line direction.

The radiometric characteristics of the sensor have to be determined from periodic measurements over test sites. Both the ground reflectance and the atmosphere are characterized simultaneously and in coincidence with the satellite overpass to estimate the observed at-aperture radiance. An ideal test site for that task should have several critical features (SCOTT et al. 1996). These include the impact of atmospheric errors (high-reflectance area) and the use of a surface reflectance that should have spatial uniformity (with near-Lambertian reflectance).

In the south-western part of the United States several calibration sites with the above required features exist and have been used for many years. Calibration using these test sites where explained in PAGNUTTI et al. (2002) and PAGNUTTI et al. (2011).

The crucial problem with the HA method are the remaining inhomogeneities of the surface. Different approaches have been suggested to overcome this problem of a non-uniform texture of the target.

In the first approach the landscape is considered to be sufficiently uniform to contribute to the low frequency signal. Statistic calculations separate the low frequency contribution to the signal's standard deviation (landscape contribution) from the high frequency contribution to the signal's standard deviation (instrument contribution).

Another method to estimate the SNR consists of selecting homogeneous snowy areas as described in DELVIT et al. (2002). As the snow-covered parts of the landscape are nearly uniform, a correct estimation of the noise can be done by calculating the standard deviation of

the signal. As there is little correlation between the noise and the signal from the landscape, images can be decomposed into an image corresponding to the 'pure' landscape and an image of noise.

A completely different approach is the noise-adjusted principal components (NAPC) transform, or maximum noise fraction (MNF) transform (Du & Raksuntorn 2006). The basic idea is to reorganize the data in a way that the principal components are ordered in terms of the SNR, instead of variance as used in the ordinary principal components analysis (PCA). The NAPC transform is very useful in multi-dimensional image analysis. As a result, object information can be better compacted into the first few principal components. A correlation method using bit planes gives reasonable results for decomposition of noise and image texture.

3 Determination of the Noise Equivalent Radiance (NER) from Real Imagery

In this study, the SNR is investigated on the radiance level NER (noise equivalent radiance). Two different methods were investigated. They are based on image data of natural homogeneous and non-homogeneous test areas. The analysis of homogeneous regions is based on a standard method to determine mean and variance of the noise. The second method, used for analyzing inhomogeneous surfaces, searches for homogeneous micro regions (consist of only few pixels) with a homogeneity criterion and clusters the results from these micro regions for NER analysis.

The NER determination with homogeneous targets is based on the evaluation of SNR in manually selected homogeneous areas. Larger homogeneous areas can be found in almost all very bright regions, i. e.. regions with high albedo values. As already mentioned earlier these noise values cannot be compared directly with the system-required values, as those were defined for the lower signal levels of the "normal" operating range, and therefore they are also much lower. To find a way for comparing the measured noise values from bright targets with the system noise requirement, a noise requirement function was derived for each band on the basis of the laboratory calibration. This was done by applying the dependency between the noise value and the signal level to the system noise requirement values determined during the laboratory measurements. If the NER of the measured radiance is lower than the NER derived from the noise requirement function, the requirement is fulfilled. For the interpolation within the range of signal levels used for the calibration this method works quite well. An extrapola-
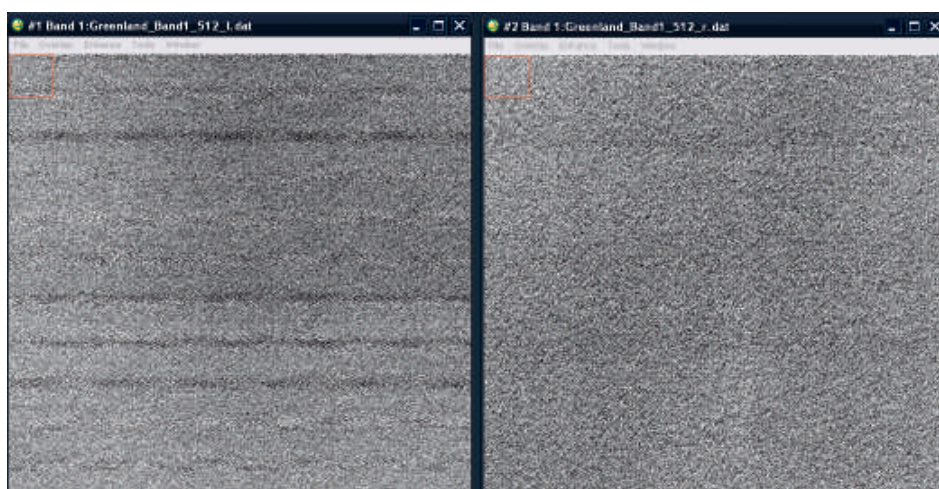

Fig. 2: The Greenland image: Example for systematic noise texture in the left and no systematic noise in the right image.

tion outside of the calibration range with only little uncertainty requires the availability of an accurate photon transfer curve (Janesick 2001).

For the noise determination homogeneous regions in the images were preselected manually. Subsets of 1024×1024 pixels were cut out in the central image part. These homogeneous image patches where extracted based on predefined criteria (related to the texture) and were used to evaluated the NER.

The selection procedure for homogeneous areas can be described as follows. In most cases, objects with a reflectivity of about 5 % to 20 % are investigated. In this reflectivity range areas with a homogeneous surface are normally very small and randomly distributed over the image. Therefore, splitting the image into many homogeneous blocks seems insufficient and additional procedures are required to recognize and analyse smaller homogeneous areas.

As already mentioned, the signal noise depends on the signal level. Moreover, for each image, random and systematic noise components are superimposed and sum up to a combined noise level. Systematic noise sources (e. g. micro-texture from the observed surface, not sufficiently corrected PRNU) can be superimposed to the random noise coming from the sensor. As an example an image part containing some remaining systematic noise is shown in Fig. 2 (left side). Images with this kind of noise are excluded for further investigation.

The image shown in Fig. 2 is not a typical example for the type of images we tried to analyse here, but we will use it later on for tests and comparison purposes. A more adequate image example is shown in Fig. 3.

For this more realistic type of images an automated procedure was developed to extract small homogeneous areas from the generally inhomogeneous image parts. Within these small areas it was assumed that the surface texture is negligible. The mean and standard deviation of the signal can be computed for these small areas. An advantage of this method is that it automatically measures noise values at different signal levels because of the different reflectance of the extracted small homogeneous image areas.

The procedure is formally based on the "homogeneous area" method used by Gao (1993) which was extended by Gao et al. (2008). For each image pixel texture information was derived in blocks around the pixel, with block sizes of 3×3, 5×5, …, 11×11 pixels. The ho-
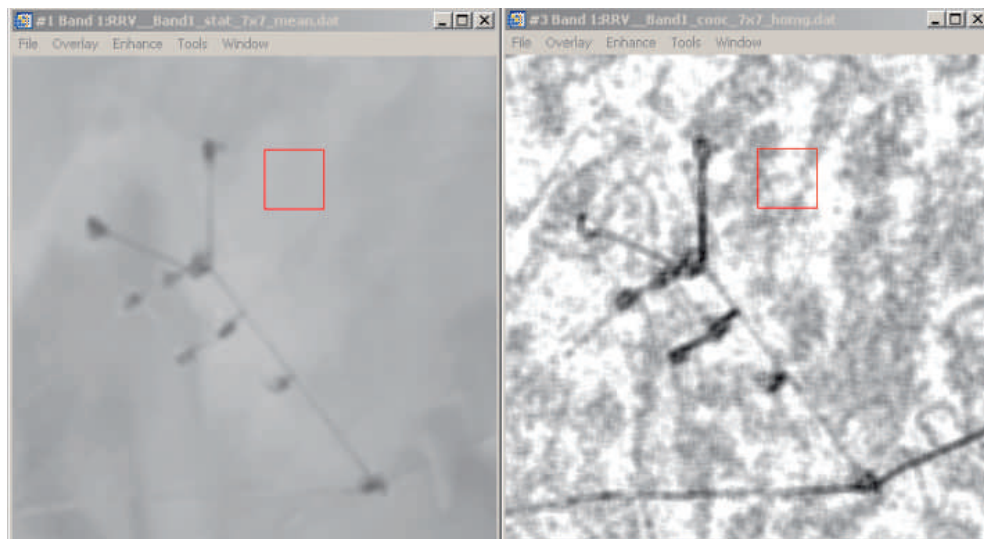

Fig. 3: Original image and homogeneity measure (right) for this image part. The image is from Railroad Valley Playa in Nevada. The left image seems homogenous except for the roads. The calculated homogeneity is seen in the right part, where bright regions stand for high homogeneity.

mogeneity texture measures were applied to the data in these blocks. In addition the mean and the standard deviation of the gray values were computed. The first step is to extract blocks with a sufficient homogeneity. It turned out that the parameter "homogeneity" derived from the *Gray-Tone Spatial-Dependence Matrix* or *Gray Level Co-Occurrence Matrix* (GLCM) (HARALICK et al. 1973) is suitable for the determination of the homogeneity level $h_{i,j}$ (inverse difference moment) at pixel (i,j):

$$h_{i,j} = \sum_{k=1}^{N} \sum_{l=1}^{N} \frac{c_d(k,l)}{1+(k-l)^2} \qquad (3)$$

In eq. 3, $c_d(k,l)$ is the GLCM, a statistical measure that contains information about the positions of pixels having similar gray level values, but does not provide any information about the repeating nature of texture. Furthermore, $d = (m \cdot \Delta, \cdot n \cdot \Delta)$ is a displacement vector. The GLCM counts all pairs of pixels separated by (m, n) pixels having the gray levels k and l. The matrix c_d has the size (N,N); N is the number of quantized gray levels. In a homogeneous image patch the range of gray levels is small and c_d will be clustered near the main diagonal. The denominator $1 + (k-l)^2$ enhances this trend. A heterogeneous image patch will be more spread. The GLCM can be calculated in different direction s (with respect to neighbouring pixel) and distances d (in pixels).

The image shown in Fig. 3 (left) is taken from Railroad Valley Playa in Nevada. The local homogeneity (right) is a measure for local similarity in the image. To achieve a separation between noise and texture, only the re-

gions or small areas with the greatest homogeneity were used for the further evaluation.

Considering the LMLSD method only pixels with sufficiently high homogeneity (close to 1) are involved in a data clustering process. For each cluster, which is related to a mean measured radiance, the variance-histogram is analyzed. It is assumed that the variance relative to the maximum of the histogram is representative for the measured radiance.

In a first test this approach is applied to the Greenland scene (Fig. 2, right) and the HA and LMLSD method are compared. Here a homogeneous area with almost only random noise will be assumed. The approach described above can therefore be directly compared to the SNR determination from the whole image part. The idea behind this is to check whether the results, i. e.. the calculated noise, according to the new method are comparable to the noise determined in the "classical" HA method. Fig. 4 shows the variance distribution and the overall result. The calculated mean is equal for both methods; the local variance deviation is related to the maximum for this data set (see Fig. 4, left) but is about 5 % - 10 % lower then the variance derived from the entire image.

To apply this procedure to an image with a complex surface texture (Fig. 3) some additional effort is required for the interpretation of the results. Fig. 5 shows the local variance with respect to the local mean for parts with maximum homogeneity. The threshold for the homogeneity value was set to 0.98.

Obviously this procedure generates a large number of small image segments with homogeneous radiometric behaviour. Regions where the image brightness changes strongly
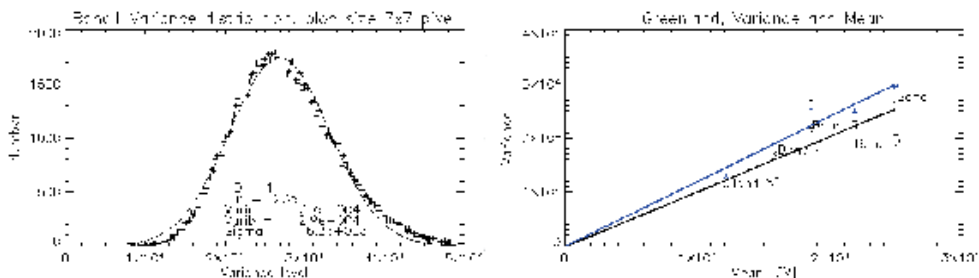
Fig 4: Variance distribution derived from LMLSD method with a maximum near the variance of the whole data set (left) for the Greenland image. Variance over mean dependence for all bands (black) with confidence interval (right) and variance derived with HA method (blue).

are excluded automatically in this procedure. As seen in Fig. 5 (left), for the extracted image parts with maximum homogeneity a data clustering with respect to the local mean seems to be possible. This was done here with histogram analysis (see Fig. 5 (right)). This procedure is equivalent to a classification based on texture parameters. The clustering however is only possible if the segmentation leads to patches that are homogeneously better than a predefined threshold value.

Fig. 6 presents the histogram of the local variance for a certain cluster. Between the minimum and the maximum of the local variance (lv), a fixed number of variance values with equal width (bins) are combined. In other words, the histogram is coarsened.

Furthermore the influence of the image block size was investigated. Four different block sizes (5×5, 7×7, 9×9, 11×11) where used for this investigation. The results show a significant influence of the block size. With increasing block size the segmentation between clusters becomes better. At the same time the number of blocks which fulfil the homogeneity criteria becomes smaller. As an optimal trade-off between these two parameters a block size of 7×7 was used in the following investigations.

Fig 5: Selected groups in the local mean – variance plot (left). Local mean histogram (right) is derived from data in the left plot and shows the selection of different clusters (related to the numbers).

Fig. 6: Histogram of the local variance (example).

4 Results and Discussion

Fig. 7 shows the result for the NER in relation to the radiance for Band 1. For the defined system reference radiance the measured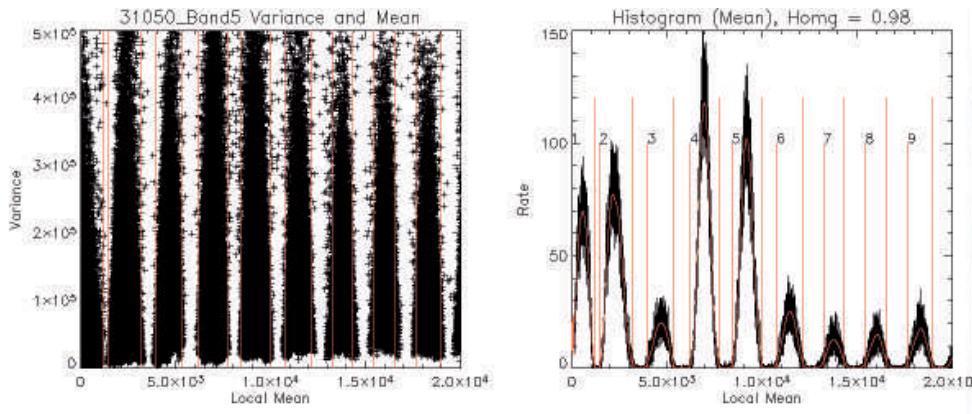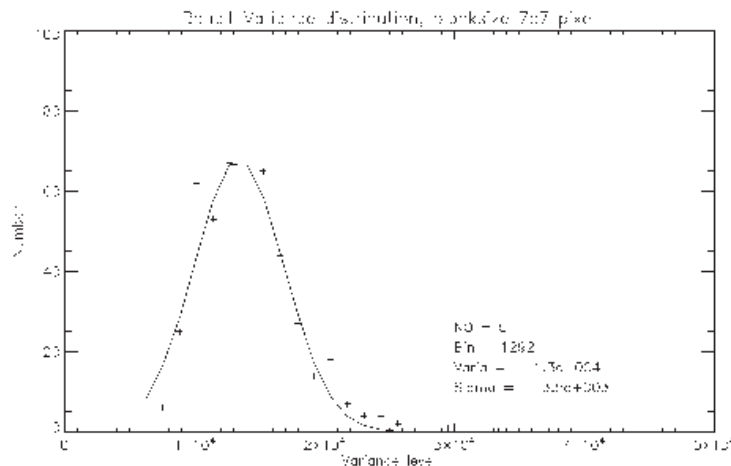 NER can be derived from the blue fitting line. Due to the Poisson distributed photon noise, the NER increases with the measured radiance.

Based on this method an in-flight determination of the radiometric image noise is possible. By comparison of the in-flight noise determination results with the NER values defined as system requirements it is possible to check whether the system is still within the specifications.

As an example, Fig. 8 shows the results for the Blue- and the Red-Edge bands of the RapidEye camera. The black diamonds in the Fig. 8 represent the in-flight calibration noise values, whereas the dotted colour lines show the pre-flight laboratory noise measurements for all five RapidEye sensors. The vertical black lines through the diamonds indicate the confidence intervals derived from the in-flight calibration measurements. The single blue star represents the system noise requirement for the RapidEye cameras, which e. g. for the Blue Band was defined at a radiance level of 72 W/m²/sr/μm. The two examples show clearly that using the presented in-flight noise determination method, a significant part of the radiomet-

ric range for normal camera operations could be covered although it was impossible to get data of the full radiometric range compared to the laboratory calibration measurements.

It is also obvious that the results of the in-flight noise measurements are in good agreement with the pre-flight calibration values for the camera noise. This is a strong indication that the camera systems are still working according to the RapidEye system specifications. No significant change of the camera characteristics regarding sensor noise after the launch and during normal operational work could be observed up to now. The measured values are clearly below the system noise requirements for the RapidEye sensors.

5 Conclusions and Outlook

The procedure described in this paper allows the evaluation of image noise directly from operational image data after the launch of a satellite sensor. This method is very important for the after-launch monitoring of the sensor quality and health status of the sensor by comparing periodic noise measurement results with the initial values defined by the system requirements.

The major problem for noise determination was to eliminate the impact of remaining sur-
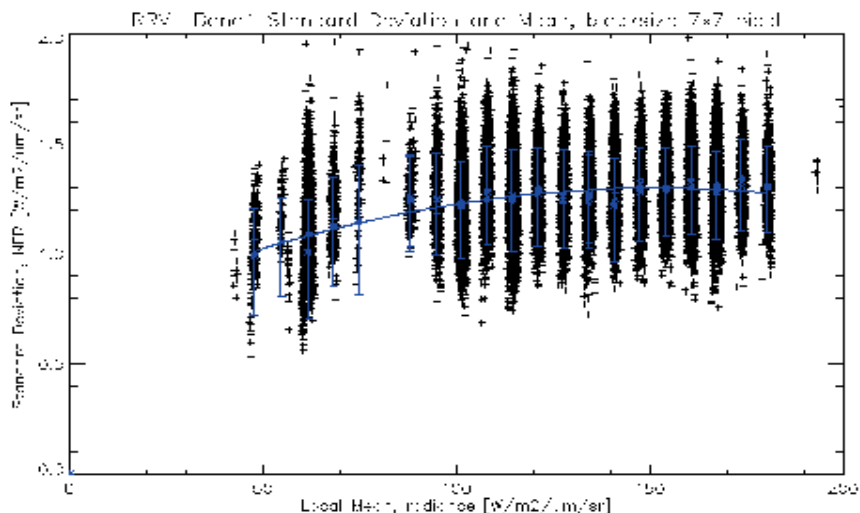
Fig. 7: Radiance vs. noise equivalent radiance (Band 1).
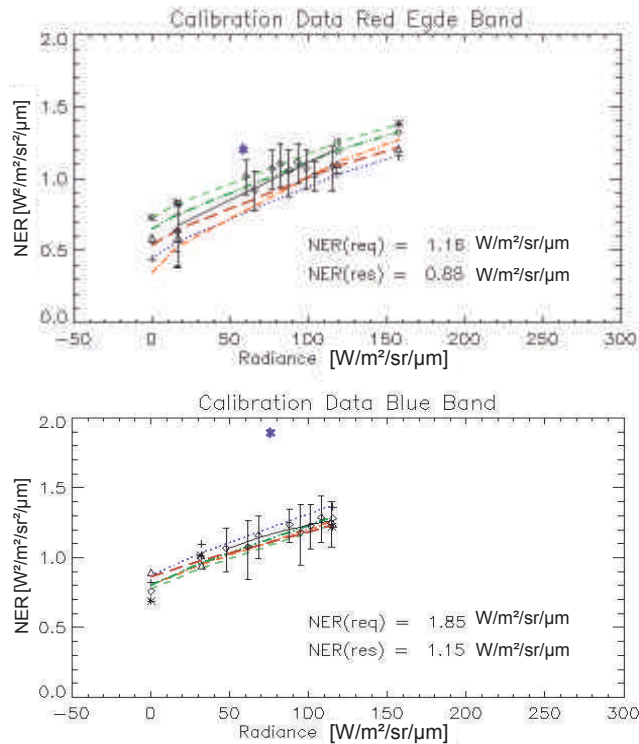
Fig. 8: Comparison of the pre-flight lab noise calibration and the in-flight noise determination according to the described procedure – Blue Band (below) and Red-Edge Band (above).

face structure. In contrast to Gao (1993), for each pixel, the local mean and variance are be determined within a block of predefined size around each pixel. To determine the influence of the remaining microstructure of the surface, an additional homogeneity criterion was used.

It was shown that with the proposed method an improvement of the NER determination for typical albedo values could be achieved. The procedure has been implemented as a semi-automatic scripted work flow. Based on this method, all 5 bands of all RapidEye cameras have been analysed. Exemplary results with two bands were presented in section 4.

In our future work, these results have to be double-checked with data from other sensors. In particular, the homogeneity criteria can be replaced by other criteria, e. g. the one described in Brügelmann & Förstner (1992).

Acknowledgements

References

Brügelmann, R. & Förstner, W., 1992: Noise Estimation for Color Edge Extraction. – In: Förstner, W. & Winter, S. (eds.): Robust Computer Vision. – Karlsruhe **1992:** 90–107.

Cramer, M., 2008: The EuroSDR approach on digital airborne camera calibration and certification. – ISPRS Congress Beijing, IAPRS, Volume **XXXVII** (B4): 1753–1758.

Delvit, J.-M., Leger, D., Roques, S., Valorge, C. & Viallefont-Robinet, F., 2002: Signal-to-noise ratio assessment from nonspecific views. – In: Serpico, S.B. (ed.): Image and Sig-

nal Processing for Remote Sensing VII **4541:** 370–381.

Du, Q. & Raksuntorn, N., 2006: Hyperspectral image analysis using noise-adjusted principal component transform. – In: Shen, S.S. & Lewis, P.E. (eds.): Algorithms and Technologies for Multispectral, Hyperspectral, and Ultraspectral Imagery XII **6233**.

Haralick, R.M., Shanmugam, K. & Dinstein, I.H., 1973: Textural Features for Image Classification. – Systems, Man and Cybernetics, IEEE Transactions on **3** (6): 610–621.

Gao, B.-C., 1993: An operational method for estimating signal to noise ratios from data acquired with imaging spectrometers. – Remote Sensing of Environment **43** (1): 23–33.

Gao, L.R., Zhang, B., Zhang, X., Zhang, W.J. & Tong, Q.X., 2008: A new operational method for estimating noise in hyperspectral images. – IEEE Geoscience and Remote Sensing Letters **5** (1): 83–87.

Luo, W. & Zhong, L., 2009: The effect of spatial resolution on the noise estimation in hyperspectral images. – In: Udupa, J.K. et al. (eds.): Multispectral Image Acquisition and Processing. – SPIE **7494**.

Janesick, J.R., 2001: Scientific charge-coupled devices. – 920, SPIE Press **PM83**.

Pagnutti, M., Holekamp, K., Ryan, R., Blonski, S., Sellers, R., Davis, B. & Zanoni, V., 2002: Measurement sets and sites commonly used for characterizations. – Proceedings of the ISPRS Commission I Mid-Term Symposium 2002: Integrated Remote Sensing at the Global, Regional and Local Scale **XXXIV**.

Pagnutti, M., Ryan, R., Blonski, S., Holekamp, K., Cramer, M., Helder, D. & Honkavaara, E., 2011: Targets, methods, and sites for assessing the in-flight spatial resolution of electro-optical data products. – Canadian Journal of Remote Sensing, Published on the web 12 May **2011**.

Reulke, R., Dörstel, C. & Schwebel, R., 2007: DIN 18740 "Photogrammetrische Produkte" Teil 4: Anforderungen an digitale Luftbildkameras und digitale Luftbilder. – DGPF Jahrestagung **2007**: 281–286.

Scott, K.P., Thome, K.J. & Brownlee, M.R., 1996: Evaluation of the Railroad Valley playa for use in vicarious calibration. – Proceedings of SPIE **2818:** 158–166.

Addresses of the Authors:

Prof. Dr. Ralf Reulke, Humboldt-Universität zu Berlin, Institut für Informatik, Computer Vision, Unter den Linden 6, 10099 Berlin, Germany, e-mail: reulke@informatik.hu-berlin.de

Dr. Horst Weichelt, RapidEye AG, Molkenmarkt 30, 14776 Brandenburg an der Havel, Germany, e-mail: weichelt@rapideye.de

System Theoretical Aspects for Designing Opto-Electronic Sensors for Remote Sensing

Ulrike Krutz, Anko Börner, Herbert Jahn, Carsten Paproth, Patrick Scherbaum & Emanuel Schlüssler, Berlin

Summary: The design of passive optical sensor systems for remote sensing requires more or less complex theoretical investigations. Based on the user requirements which are characterized by data products all relevant physical effects influencing the generation of an image have to be considered and modeled. The goal is to build the whole chain of signal generation and transformation: from the source of light, through the atmosphere to the object to be observed, through the atmosphere back to the sensor system. These models can be applied to simulations which can be used for the optimization of sensor parameters and observation conditions and for the estimation of the potential performance of such a system. For this task, specific retrieval algorithms have to be considered closing the loop of developing camera systems.

The paper contains classical approaches for a system design as a standard tool used in the Institute for Robotics and Mechatronics including methods for modeling the geometrical and radiometric relations and the description of camera hardware. The results of a complex investigation of the point spread function of camera systems form the core topic of this paper.

Zusammenfassung: *Systemtheoretische Aspekte zum Design von opto-elektronischen Sensoren für die Fernerkundung.* Die Auslegung von passiven optischen Sensorsystemen für die Fernerkundung erfordert je nach Applikation mehr oder minder komplexe Voruntersuchungen. Ausgehend von den Nutzeranforderungen an ein Kamerasystem, die in der Regel durch Datenprodukte charakterisiert werden, müssen alle relevanten physikalischen Effekte, die zur Generierung eines Bildes beitragen, berücksichtigt und modelliert werden. Ziel ist es, die gesamte Kette der Signalentstehung und -wandlung nachzubilden: vom Beobachtungsobjekt und seiner Beleuchtungsquelle, über die Atmosphäre bis hin zum Sensorsystem. Diese Modelle können in Simulationsrechnungen einfließen, die die Optimierung von Sensorparametern und Aufnahmebedingungen sowie die Bewertung des Potenzials eines solchen Systems gestatten. Für diese Aufgaben müssen konkrete Auswertealgorithmen in den Entwurfsprozess einfließen, womit sich der Entwicklungskreis schließt.

Der Beitrag umfasst klassische Ansätze zur Systemauslegung, die im Institut für Robotik und Mechatronik verfolgt werden. Darunter fallen Verfahren zur Modellierung der geometrischen und radiometrischen Verhältnisse sowie die Beschreibung der Hardware der Kamera. Die Ergebnisse einer beugungstheoretischen Untersuchung zur Punktverschmierungsfunktion von Kamerasystemen bilden den Schwerpunkt dieser Arbeit.

1 Introduction

In the 1980s the opto-electronic sensor department of the Institut für Kosmosforschung in Berlin-Adlershof started to design passive imaging sensors for remote sensing. One of the first projects in that direction was the design of a spaceborne imaging sensor for the detection of ocean waves and the estimation of wave parameters (Jahn et al. 1989). In that connection the idea arose to model and simulate the whole system comprising of the light source (blue sky light), the atmosphere, the scene (ocean water with waves), and the optical and

electronic parts of the sensor up to the image data in order to obtain optimal system performance for wave parameter determination. At the same time CCD sensors became available and have been studied carefully (OERTEL et al. 1985). After those first approaches the system theoretic aspects of opto-electronic sensor systems were developed in more detail resulting in a book (JAHN & REULKE 1995), in simulation software packets (JAHN et al. 1992, BÖRNER et al. 2001), and in the design of various sensors, e. g. WAOSS (SANDAU & ECKARDT 1996, SANDAU et al. 2000), HSRS for the small satellite BIRD (Bi-Spectral Infrared Detection) (SKRBEK & LORENZ 1998) and others. This work is now carried on in DLR's department of Optical Information Systems in various projects e. g. MERTIS (ARNOLD et al. 2009). In more detail, the system theoretic approach to remote sensing systems comprises the description and modelling of:

- the emitted radiances of the light source, e. g. a light reflecting and/or emitting surface with its physical and geometrical parameters,
- the atmospheric path of the radiation (radiation transfer, use of software packages, e. g. MODTRAN),
- the optical system with its fundamental parameters such as point spread function (PSF), modulation transfer function (MTF) and others,
- the opto-electronic detector with its characteristics (quantum efficiency, PSF, photo-response non-uniformity (PRNU), dark signal non-uniformity (DSNU) etc.),
- the electronic read-out channel with its impulse response,
- the analogue digital unit (ADU),
- the various noise components of all these components and, last but not least,
- the data evaluation algorithms, e. g. for object detection or classification.

The goal of that approach is to fulfil the scientific objectives of the project as optimally as possible, under certain constraints such as available technology and money. Ideally, the evaluation algorithm provides a quality criterion, e. g. for parameter estimation or classification, which depends on system parameters such as focal length, integration time etc. Then, minimizing that criterion provides op-

timal system performance. Of course, that approach often cannot be carried out in full purity but it gives a good guideline for system design. Additionally, observation conditions, e. g. orbit, season, time, and retrieval algorithms can provide input for an overall optimizing approach.

2 Modelling Approaches

The following paragraph describes typical approaches for system modeling. Depending on the project phase (from pre-studies to final system design) more or less complex models are applied.

2.1 Derivation of Top Level Requirements

Based on user requirements (geometrical resolution, swath width, number and position of spectral bands), technical top level requirements of the camera system are derived. For the design of imaging optical systems signal-to-noise ratio (SNR), MTF (typically at Nyquist frequency), wavelength and bandwidth of spectral bands and radiometric dynamics are the most important quantities defining parameters such as focal length, size of aperture, system clock and data rate. These optical and electronic system parameters are used to perform a first estimation about the expected system performance. As a basic input qualitative and quantitative information about incident light being reflected or emitted from the object to be observed is required. For this purpose, realistic at-sensor radiances have to be estimated by applying atmospheric transfer models, e. g. MODTRAN. The number of photons is converted into electrons considering optics and detector parameters. Most dominant noise sources are estimated to calculate the system's SNR.

The geometric resolution of a camera system is defined by ground sample distance, blur due to optical diffraction, motion of the camera during capturing the image and SNR. Usually, Rayleigh criterion is applied defining the distance of two single spots which can

be distinguished considering the effects mentioned above.

Such rough calculations are basic input for proposals for remote sensing missions for Earth observation or planetary research.

For concrete system designing and optimizing system parameters, more complex approaches have to be pursued. The next chapters describe tools supporting theses tasks. In general, geometrical and radiometric relations have to be considered as well as the hardware parameter of the opto-electronic system.

2.2 *Geometric Properties*

The challenge of the geometry module of the sensor simulation is to figure out to which direction each camera pixel is geared. For this purpose, a simple ray tracing approach is taken. Therefore, a digital terrain model (DTM) and a camera model as input are essential. Then the intersections of each ray can be investigated, constructed from the camera description for each pixel, with the DTM. The nearest intersection is taken as result. Furthermore, the same procedure can be applied to determine whether the area is shadowed or not, simply by using rays from the intersection points to the sun. If there is a nearer intersection between the DTM and the sun, then the observed area is shadowed. Finally, we obtain the following information from the geometry module for each camera pixel:

- the intersection point in Cartesian and geodetic coordinates,
- the surface normal at the intersection point,
- the Boolean shadow value,
- accompanying map values, e. g. albedo and temperature.

These results are needed for the radiometry module of the sensor simulation.

The described rendering procedure and with it the resulting camera images can suffer from the sample problem which results in aliasing due to under-sampling of the scene. To decrease the effect of aliasing, we can increase the resolution of the camera model, i. e. use more rays per pixel, or reduce the resolution of the geometric description of the scene, i. e. use a lower resolution DTM. The increas-
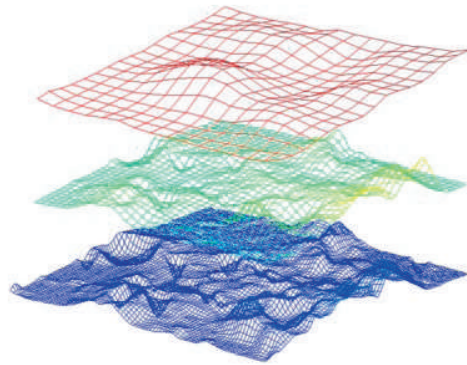
Fig. 1: The DTM is used in different resolutions to decrease aliasing.

ing of rays per pixel improves the image quality, but it also increases the computing power needed for one camera image. Lower space-resolved DTMs are part of this multi-resolution ray tracing approach. Starting point is a spatially high-resolution DTM from which the lower resolution models are created. This model is transformed into a pyramid of models where each model obtains only half of the linear resolution of the previous model, see Fig. 1. During the ray tracing procedure, the model with the best fitting resolution is chosen according to the ground resolution seen from the camera.

Moreover, the geometry module makes it possible to cover the interesting area with tiles. The size of the individual tiles can be kept small so that the need for memory is low for one tile. During the ray tracing only the currently needed tiles are kept in memory. The available memory is managed with a caching strategy. By this innovation, the area can be covered by terrain models with different resolutions, e. g. Germany as a whole can be covered by a DTM with low resolution while specific areas are considered with a high-resolution DTM.

2.3 *Radiation Transfer Models*

For the simulation of a sensor, the radiometric behaviour has to be specified (Börner et al. 2001). This is done with the radiometry module which calculates the at-sensor radiance

for every pixel of the camera from the visible spectral range to the thermal infrared. This module uses MODTRAN (BERK et al. 1987) for the radiative transfer through the atmosphere. The module works in two steps. The first step is the creation of a spectral look-up table for the global atmosphere parameters. In the second step this look-up table is applied to create spectral radiances for the local simulation parameters, e. g. albedo and surface normal. This procedure is much faster than the direct usage of MODTRAN and produces similar results. The required input parameters of MODTRAN are: spectral range and step size; average ground height; sensor altitude; sensor zenith angle; atmospheric model; haze model; visibility; sun zenith angle; albedo ρ and temperature T. Unless specified, the MODTRAN default values are used.

The at-sensor radiance can be written as a sum of five addends, see Fig. 2,

$$L(\lambda) = L_{dir} + L_{ind} + L_{sc} + L_{em} + L_{th} \qquad (1)$$

The indirect and scattered contributions L_{ind}, L_{sc} and L_{th} are calculated directly with MODTRAN and are part of the lookup table.

The direct and emitted contributions can be calculated with

$$L_{dir} = L_{sun} \cdot \cos\alpha \cdot \rho \cdot s \qquad (2)$$

and

$$L_{em} = B(T) \cdot (1-\rho) \cdot \tau \qquad (3)$$

with the solar irradiance L_{sun} and the transmittance of the atmosphere τ, which are also part of the lookup table. The angle between the surface normal and the incident light α as well as the Boolean shadow variable s are both results of the geometry module. With the spectral radiance of a blackbody $B(T)$ mapped values of ρ and T can be used to complete the radiometric simulation of a whole camera image without using MODTRAN directly for every camera pixel. Finally, the spectral at-sensor radiance for the corresponding spectral range gets convolved with a rectangular function to achieve the desired spectral step size and to avoid aliasing. The resulting spectrum is passed onto the camera module, which accomplishes the final processing. An example spectrum is shown in Fig. 3.

Fig. 2: MODTRAN calculates these contributions to the at-sensor-radiance: L_{dir} is the direct reflected solar radiance, L_{ind} is the indirect reflected solar radiance, L_{sc} is the scattered solar radiance, L_{em} is the emitted thermal radiance, and L_{th} is the scattered thermal radiance.
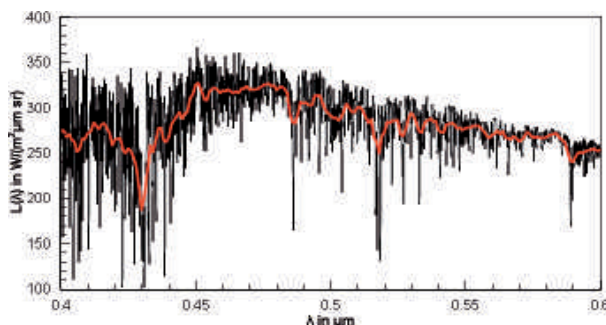
Fig. 3: Spectral at-sensor radiance for a mid-latitude summer atmosphere, sun at the zenith, sensor altitude 100 km, and $\rho = 0.5$. The red curve is the convolution of the at-sensor radiance with an appropriate rectangular function for a spectral step size of 1 nm.

2.4 *Camera Models*

By modelling the camera, the geometrical and physical properties of optics and sensor are simulated. The first step is the provision of data for further processing for the Raytracer. Then, the results of the radiometric simulation can be processed. The Raytracer requires the normalized direction vector for each pixel. The camera includes the position of each pixel in relation to the projection centre. With this position and the position of the principal point, the Raytracer can generate the direction vector (Fig. 4). With these pixel positions the geometric characteristics of various detector types such as Matrix, Line, Staggered and TDI can be modelled.

The output data of the radiometric simulation is represented by the at-sensor radiance. Out of this data, the digital number (DN) has to be calculated by the camera module. Therefore, the number of electrons which are liberated by the photons must be determined:

$$n_{el} = \frac{\pi}{4} \cdot \frac{1}{f_\#^2} \cdot A_d \cdot f_f \cdot t_{int} \int_{\lambda_1}^{\lambda_2} d\lambda \frac{\lambda}{h \cdot c} \cdot L(\lambda) \cdot \tau(\lambda)$$
$$\cdot QE(\lambda) \tag{4}$$

where $f_\#$ is the f-number of the optical system, A_d the area of a pixel, f_f the fill factor of a sensor element, t_{int} the integration time, λ the wavelength, $L(\lambda)$ the radiance (eq. 1), τ the transmission of the optical system and QE the quantum efficiency. Furthermore, h denotes the Planck constant and c the speed of light in vacuum.

If the bit depth (Depth) and the full well capacity ($Cap_{FullWell}$) of the detector are known entities, the digital number can be calculated

by quantization, as shown in the following formula:

$$DN = \frac{n_{el} \cdot (2^{Depth} - 1)}{Cap_{FullWell}} \tag{5}$$

The full well capacity determines the maximum number of electrons which the detector can generate. Furthermore, it represents a gain level which is used for the exposure. These simulated results usually do not correspond to reality. However, when the distortion model of the optics and the noise model of the sensor are known, it is possible to derive a result that reflects reality (HARTLEY & ZISSERMANN 2003).

3 Investigation of PSF

The previous section dealt with a geometrical and a radiometric approach of camera description. Now, a diffraction-theoretical approach follows, taken into account the point spread function (PSF). Consider a system like in Fig. 5. Here, g denotes the distance between object plane and the optics and f the focal length. Furthermore, n and n'' represent normal vectors, U' the amplitude right behind the object plane and V the amplitude right in front of the optics. Likewise, V' describes the amplitude immediately behind the optics and U the amplitude in front of the image plane.

By mapping a point P' of the object plane to the image plane, the point is blurred by the PSF. For translation-invariant systems the following equation is valid

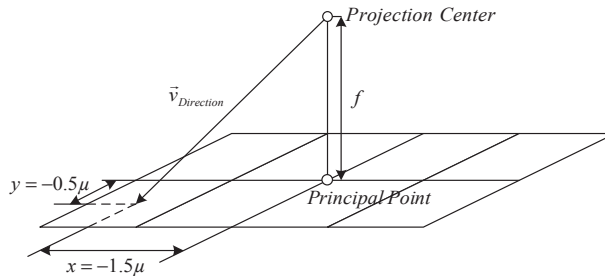$$b(P'') = \int_{-\infty}^{\infty} dP' \, \hat{g}(P') \cdot H(P'' - P') = (\hat{g} * H)(P'') \tag{6}$$

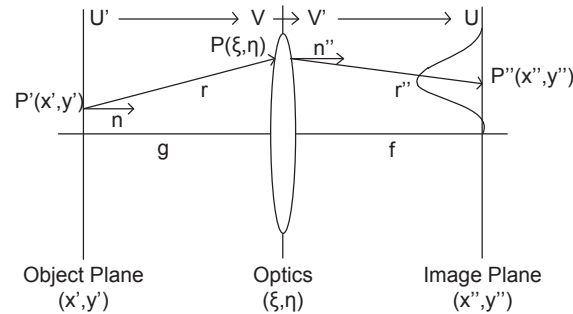**Fig. 4:** Direction vector of a pixel as used in a Raytracer.

Fig. 5: Mapping a point *P'* of the object plane (x', y') to the image plane (x", y") underlies impairments caused by the system's point spread function. g is the object distance, *P'* the emitting point, *P''* the image of the emitting point *P'*, *f* is the focal length, which is in the general case the image distance (b). ξ and η are the coordinates in the lens frame. ξ" and η" are the coordinates in the image frame. r and r" are the corresponding direction vectors.

where b is the image, H the PSF and $\hat{g}$ the point's intensity on the image plane.

The resulting image underlies all impairments caused by the system's total PSF. Let the system now be separable, so that it can be split into the components optics and detector. Furthermore, motion and eventually the atmosphere contribute to a blurring of the original signal. This blurring finds its expression in the successive convolution of the signal with the according point spread function of the system components.

3.1 *PSF of the Optics*

There are at least three different ways to determine the PSF of optics in theory, among quite a few possibilities to determine it in a practical way (Talbiersky 2010, Jahn & Reulke 1995). In theory the PSF of optics can be either calculated by the Kirchhoff diffraction formula, the Fresnel- or the Fraunhofer formula. Here, Kirchhoff is the origin for both, Fresnel, which is a square approximation, and Fraunhofer, which approximates Kirchhoff in a linear way. Like in Cooper et al. (2002) the Kirchhoff formula used here underlies the Kirchhoff boundary conditions (Born & Wolf 1999) as it is assumed that at the edge of the aperture the amplitude of the wave of the object to be imaged turns to zero quite suddenly. In practice this is mostly not the case. Furthermore, the polarization of light is ig-

nored and the calculations are based on scalars rather than on vectors. Therefore, the Kirchhoff diffraction formula itself is only an approximation of the exact issue.

The PSF by Kirchhoff is given by the following formula (Jahn & Reulke 1995)

$$H_\lambda^{OPT}\left(P', P''\right) =$$

$$\left| e^{\frac{2\pi i}{\lambda} \cdot n_\lambda \cdot \Delta} \iint_{O_L} d\xi d\eta \; e^{-\frac{\pi i}{\lambda f}\left(\xi^2 + \eta\right)} \cdot \right.$$

$$\left. \frac{e^{\frac{2\pi i}{\lambda}|\underline{r}''|}}{i\lambda|\underline{r}''|} \cdot \frac{\underline{n}'' \cdot \underline{r}''}{|\underline{n}''| \cdot |\underline{r}''|} \cdot \frac{e^{\frac{2\pi i}{\lambda}|\underline{r}|}}{i\lambda|\underline{r}|} \cdot \frac{\underline{n} \cdot \underline{r}}{|\underline{n}| \cdot |\underline{r}|} \right|^2 \tag{7}$$

where $r = \begin{pmatrix} \xi - x' \\ \eta - y' \\ g \end{pmatrix}$ and $r'' = \begin{pmatrix} \xi'' - x' \\ \eta'' - y' \\ b \end{pmatrix}$. Furthermore, λ is the wavelength, n_λ the refractive index and Δ the maximal diameter of the lens. The other parameters are the same as in Fig. 5. Obviously, this formula appears to be quite cumbersome. Fresnel approximations offer a large variety of advantages such as the way of simplifying modeling diffraction effects due to the replacement of a square root in a phase term by a quadratic form and minor other changes. Moreover, there are quick ways of implementing Fresnel (Mendlovic et al. 1997). This is especially the case for diffraction-limited systems as the PSF by Fresnel can be solved analytically by using polar coordinates. The result is the Bessel function J_l:

$$H_\lambda^{OPT}\left(P',P''\right)=\left|G\cdot 2\cdot\pi\cdot R^2\cdot\frac{J_1\left(\frac{2\pi}{\lambda b}\cdot\rho\cdot R\right)}{\frac{2\pi}{\lambda b}\cdot\rho\cdot R}\right|^2$$

(8)

Where R is the radius of the lens, λ the wavelength, ρ the distance in the image frame (or x''-y''-frame) from the centre point of the PSF, and

$$G:=-\frac{e^{\frac{2\pi i}{\lambda}(b+g)}}{\lambda^2\cdot b\cdot g}\cdot e^{\frac{\pi i}{\lambda b}\left(x''^2+y''^2\right)}\cdot e^{\frac{\pi i}{\lambda g}\left(x'^2+y'^2\right)}\cdot e^{\frac{2\pi i}{\lambda}n_\lambda\Delta_0}.$$

The diffraction pattern is the well-known Airy disk.

Let $P' = (x',y') = (0,0)$ and $P'' = (x'',y'') = (0,0)$ be on-axis observation points. In the following (P',P'') is represented by the vector $\underline{0}$. By using polar coordinates eq. 7 is transferred into

$$H_\lambda^{OPT}\left(\underline{0}\right)=$$
$$\left|-\int_0^R dr\ \frac{2\pi bg}{\lambda^2}\cdot\frac{e^{-\frac{\pi i}{\lambda f}r^2}\cdot e^{\frac{2\pi i}{\lambda}\left(\sqrt{r^2+b^2}+\sqrt{r^2+g^2}\right)}}{\left(r^2+b^2\right)\cdot\left(r^2+g^2\right)}\cdot r\right|^2$$

(9)

Likewise the PSF for Fresnel is

$$H_\lambda^{OPT}\left(\underline{0}\right)=\left|-\int_0^R dr\ \frac{2\pi}{\lambda^2 bg}\cdot e^{\frac{2\pi i}{\lambda}(b+g)}\cdot r\right|^2$$

(10)

Unfortunately, the advantages of Fresnel cannot be used for arbitrary camera systems. For configurations with wide aperture, e. g., the application of Fresnel approximation is not possible without accepting an unagreeable deviation. In Figs. 6 and 7 this effect is shown for a laboratory configuration with a focal length $f= 0.02\ m$, ground distance $g = 1\ m$ and a varying f-number. For low f-numbers the percentage mistake – regarding to the maximal values of the PSF of Kirchhoff and Fresnel – nearly hits 100% while the mistake tends to zero for f-numbers greater than 6.

Consider now the real and complex integrands of eq. 9 and eq. 10.

As can be seen in Fig. 8 and Fig. 9, the formula of Fresnel approximates the formula of Kirchhoff quite well for small apertures. For bigger values of r, Kirchhoff begins to oscillate – Fresnel cannot be used as an approximation anymore. The first zero of the complex integrand can be taken as a criterion up to which maximal aperture radius the formula
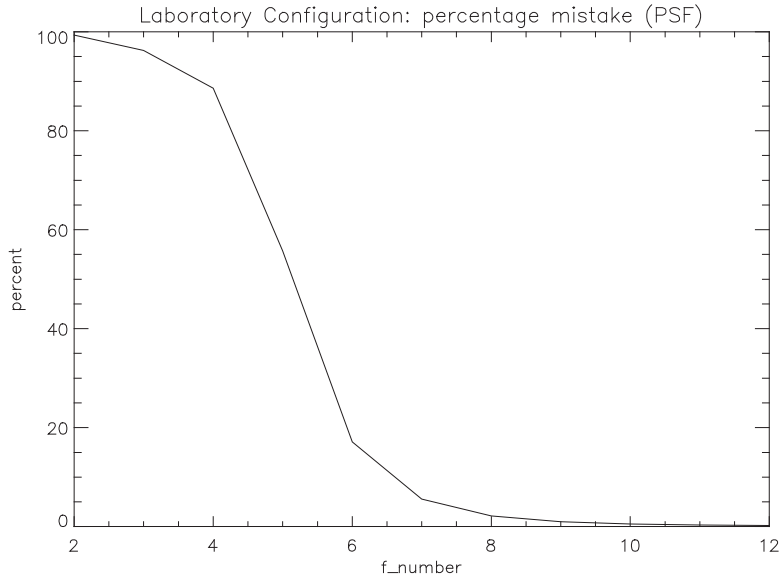
Fig. 6: Percentage mistake (PSF), regarding to the maximal values of the PSF of Kirchhoff and Fresnel.
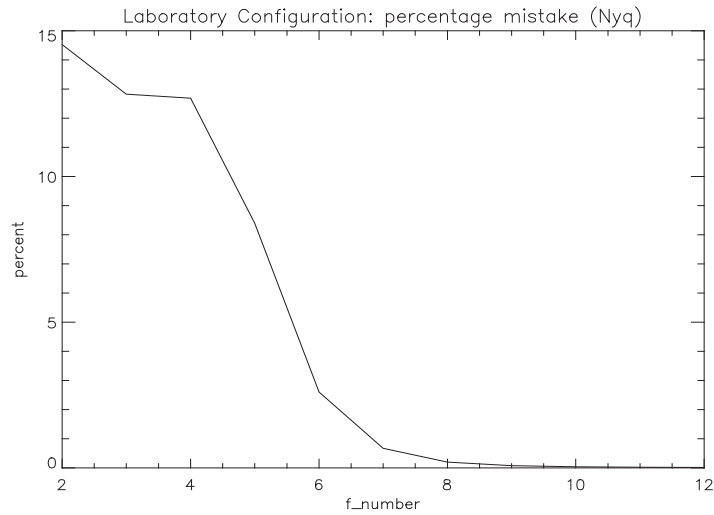
Fig. 7: Percentage mistake (at Nyquist frequency), regarding to the maximal values of the PSF of Kirchhoff and Fresnel.
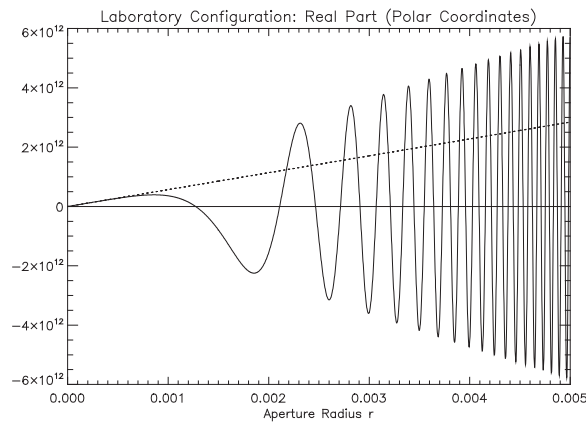
Fig. 8: Real Part of integrand.

by Fresnel can be used instead of Kirchhoff's. An analytical determination of zero leads to an equation from which the minimal f-number is derived, so that Fresnel approximations can still be applied to a system:

$$f_{\#\min} = \frac{\gamma}{2 \cdot R_{zero}} \tag{11}$$

with

$$R_{zero} = \sqrt[4]{\frac{8(\alpha + \beta) - 2l}{\frac{1}{\alpha^3} + \frac{1}{\beta^3}}}, \alpha := \frac{g}{\lambda}, \beta := \frac{b}{\lambda}, \gamma := \frac{f}{\lambda}$$

and l the first zero of the imaginary part or the real part of the integrand, depending on even or odd l.

For the laboratory configuration the zeros are calculated to $r_1 = 0.0013$ and $r_2 = 0.0018$. The error interval therefore is [0.2 %, 5 %] and the F-numbers range between ~ 6 (resulting from r_2) and ~ 8 (resulting from r_1). If one compares these values with the former results for different f-numbers it is significant that the bigger one of the first two zeros provides the minimal f-number for which the usage of the Fresnel formula is possible.
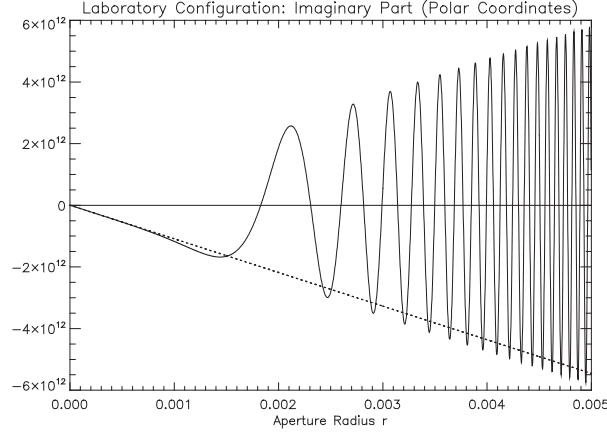
Fig. 9: Imaginary part of integrand.

Due to ignorance of the true PSF it is often convenient to use a simplified PSF-model represented by the following Gaussian function instead of the formulas given above:

$$H_\lambda^{OPT}\left(P',P''\right) =$$

$$\frac{1}{2\cdot\sigma^2\cdot\pi}\cdot\left(\frac{f}{g}\right)^2\cdot e^{-\frac{1}{2\sigma^2}\left[\left(\frac{f}{g}x'+x''\right)^2+\left(\frac{f}{g}y''+y''\right)^2\right]} \quad (12)$$

where $\sigma_x = \sigma_y = \sigma$. If the object distance is not fixed, but varies with the time, the PSF results into

$$H_\lambda^{OPT}\left(P',P'',t\right) =$$

$$\frac{1}{2\cdot\sigma^2\cdot\pi}\cdot\int_0^{t_{int}} dt\left(\frac{f}{g(t)}\right)^2\cdot e^{-\frac{1}{2\sigma^2}\left[\left(\frac{f}{g(t)}x'+x''\right)^2+\left(\frac{f}{g(t)}y''+y''\right)^2\right]} \quad (13)$$

3.2 *PSF of Motion*

The PSF of motion has to be considered whenever movement occurs between camera and object, nevertheless whether the camera or the object or both are the moving elements. In this section motion in x- and in y-direction are taken into account. The motion in z-direction effects the PSF of optics as can be seen in eq. 13 with g instead of z. Let $s(t) = s(0) + \int_0^{t_{int}} dt\, v(t)$ describe the distance

that a mapped point with a certain velocity $\underline{v}(t) = (v_x(t), v_y(t), v_z(t))$ covers on the CCD during the integration time. To obtain the PSF of motion, a moving light impulse represented by the term $\delta(x-s_x(t))\cdot\delta(y-s_y(t))$ has to be integrated over a certain time span. This results into

$$H^M\left(x,y\right) = \frac{1}{t_{int}}\sum_k \frac{1}{\left|v_x\left(t_k\right)\right|}\cdot\delta\left(y-\int_0^{t_k} dt'\,v_y\left(t'\right)\right)$$
$$\cdot R_{t_{int}}\left(t_k - \frac{t_{int}}{2}\right) \quad (14)$$

where t_k denotes the zeroes of the equation

$$\varphi(t) := \int_0^t dt'\,v_x\left(t'\right) - x = 0 \quad (15)$$

and $R_{t_{int}}(t)$ the rectangular function.

Let the motion be random $v_x(t) = \sin(\omega t)$, $v_y(t) = \cos(\omega t)$ and represent, e. g. the jitter of an airplane restricted by the angle $\alpha < \frac{\pi}{2}$. The integration time is $t_{int} = \frac{\alpha}{\omega}$. Furthermore let $x \in [0, t_{int}]$ where $t_{int} < \frac{\pi}{2\omega}$. Then the PSF of motion is given by

$$H^M\left(x,y\right) = \frac{1}{t_{int}}\cdot\frac{1}{\left|\frac{1}{\omega}\cos\left(\omega t_0\right)\right|}\cdot\delta\left(\cos\left(\omega t_0\right) - y\right)$$
$$\cdot R_{\frac{\alpha}{\omega}}\left(t_0 - \frac{\alpha}{2\omega}\right) \quad (16)$$

where $t_0 = \dfrac{1}{\omega}\sin^{-1} x$ is the only zero of eq. 16. In contrast to the PSF of the optics, a point source mapped onto the CCD is not blurred to a disk, but rather stretched to a line.

3.3 *PSF of the Detector*

Let the detector be ideal, i. e., a rectangle with the side lengths Δ_x and Δ_y. Furthermore the whole surface shall be of the same sensitivity. Then the PSF of the detector can be represented by

$$H^D(x,y) = \begin{cases} \dfrac{1}{\Delta_x \Delta_y} & for -\dfrac{\Delta_x}{2} \le x \le \dfrac{\Delta_x}{2}, -\dfrac{\Delta_y}{2} \le y \le \dfrac{\Delta_y}{2} \\ 0 & else \end{cases}$$

(17)

3.4 *Total PSF*

The total PSF of the system is obtained by the successive convolution of the PSFs of the system components and the PSF of motion. Before the original signal is smeared by the PSF of the optics, also the PSF of the atmosphere might contribute to the blurring. The PSF of the atmosphere can be approximated by a 2-dimensional Gaussian function like the one in eq. 12. A more detailed description can be found in KRISHNAKUMAR & VENKATAKRISHNAN (1998). If this PSF has to be taken into account

– whether yes or no depends on the project – both functions have to be convolved:

$$H^{(2)}(x,y) = \iint_{O_L} d\xi d\eta\, H^{OPT}(x-\xi, y-\eta) \cdot H^{ATM}(\xi,\eta)$$

(18)

If the atmosphere can be neglected, it is $H^{(2)}(x,y) = H^{OPT}(x,y)$. Then it is

$$H^{(3)}(x,y) = \iint_{O_L} d\xi d\eta\, H^D(x-\xi, y-\eta) \cdot H^{(2)}(\xi,\eta)$$

(19)

At last the PSF of motion smears the signal, so that the total PSF is obtained:

$$H^{total}(x,y) = \iint_{O_L} d\xi d\eta\, H^M(x-\xi, y-\eta) \cdot H^{(3)}(\xi,\eta)$$

(20)

A detailed description of the results can be found in (KRUTZ 2011).

4   Simulation and System Optimization

Based on the models of all relevant components of a complex system (including source of light, atmosphere, object, camera) computer simulations will be performed in order to recreate the real world and the behaviour of the opto-electronic system before it is built. The models are implemented into program languages (typically IDL, C, C++), all relevant input parameters of theses models can be set allowing the run of batches. These simulations
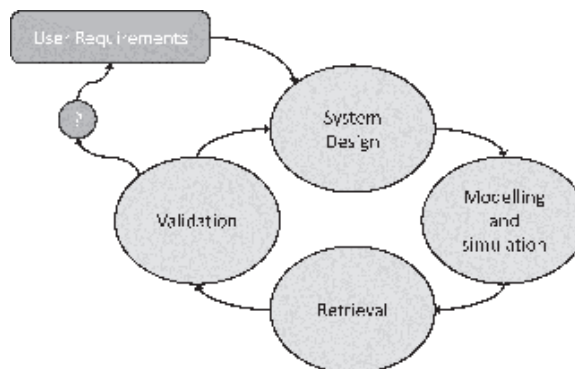

Fig. 10: Typical development cycle using models and simulation.

will result in virtual data which can be analyzed by dedicated retrieval algorithms deriving quantities which can be compared directly with user requirements. Modeling and Simulating allows the definition if a development cycle as depicted in Fig. 10.

Based on user requirements, technical top-level requirements will be derived. These parameters are used for a first system design being input for modeling and simulations. Outcoming virtual data can be processed with retrieval algorithms allowing a comparison between users expectations and systems capabilities. If necessary, system design, observation conditions and/or retrieval algorithms have to be adapted until an optimization criterion is reached.

As an example, the optimization cycle of a star sensor will be described. Starting with user requirements (pointing knowledge), top level parameters of the camera will be derived (focal length, SNR, MTF). These values will be used to define a camera model which enables the developing team to simulate images taken by this virtual camera under certain conditions (e. g. the camera's viewing direction). These images include all relevant effects, e. g. noise and blur. A retrieval algorithm then detects stars, performs an object matching with the star catalogue and determines viewing direction of the camera. The deviation between input viewing direction and determined viewing direction is an error criterion, which shall be minimized. This error minimization or system optimization is realized by dedicated changing of relevant parameters of the whole system, e. g. reducing the jitter of the satellite bus, improving optical MTF.

5   Conclusion and Outlook

Designing optical payloads for dedicated scientific or commercial tasks requires a precise analysis of the complete system including the environment and the sensor system itself based on physical models. Considering all relevant parameters of the object to be observed, the radiative transfer and the opto-electronic device allow the optimization of the all-over system chain with respect to performance and costs. Such an approach is worthwhile and in-dispensable for detector systems for remote sensing applications against the background of steadily increasing user requirements, limited ressources, operational availability and high accuracy and reliability.

Future work will be focussed on investigations on new optical technologies, e. g. potential of segmented and synthetic apertures, new detectors, e. g. sCMOS cameras, sensor data fusion, e. g. potential of radar / optics fusion / hyperspectral infrared systems, for applications in Earth observation and Planetary exploration.

References

ARNOLD, G., HIESINGER, H., HELBERT, J., PAPROTH, C., SÄUBERLICH, T., PETER, G. & WALTER, I., 2009: Thermal Infrared Imaging of Mercury – MERTIS – a New Remote Sensing Technology. – Infrared Spaceborne Remote Sensing and Instrumentation XVII, Proceedings of the SPIE **7453**, San Diego, CA, USA.

BERK, A., BERNSTEIN, L.S. & ROBERTSON, D.C., 1987: MODTRAN: A Moderate Resolution Model for LOWTRAN. – Techical Report, Air Force Geophysics Laboratory.

BORN, M. & WOLF, E., 1999: Principles of Optics. – **7th**, Cambridge University.

BÖRNER, A., WIEST, L., REULKE, R., RICHTER, R., KELLER, P., SCHAEPMAN, M. & SCHLÄPFER, D., 2001: SENSOR: a Tool for the Simulation of Hyperspectral Remote Sensing Systems. – ISPRS Journal of Photogrammetry and Remote Sensing **55:** 299–312.

COOPER, I., SHEPPARD, C. & SHARMA, M., 2002: Numerical Integration of Diffraction Integrals for a Circular Aperture. – Optik. – International Journal for Light and Electron Optics **113** (7): 293–298.

HARTLEY, R. & ZISSERMANN, A., 2003: Multiple View Geometry in Computer Vision. – **2nd**, Cambridge University Press, Cambridge, UK.

JAHN, H. & REULKE, R., 1995: Systemtheoretische Grundlagen optoelektronischer Sensoren. – 253, Akademie Verlag, Berlin.

JAHN, H., OERTEL, D., SANDAU, R. & ZIMMERMANN, G., 1989: Aspects of the Determination of Ocean Wave Parameters by Means of an Optoelectronic Satellite Sensor. – Acta Astronautica **19** (6–7): 513–519.

JAHN, H., REULKE, N. & REULKE, R., 1992: Simulation von Bilddaten für die Mars-Missionen. – Bild & Ton **45:** 276–281.

KRISHNAKUMAR, V. & VENKATAKRISHNAN, P., 1998: Determination of the Atmospheric Point Spread Function by a Parameter Search. – Astronomy & Astrophysics Supplement Series **131** (126).

KRUTZ, U., 2011: Analytische Betrachtung optisch abbildender Sensorsysteme im Rahmen der AsteroidFinder-Mission. – Ph.D. Dissertation, Humboldt Universität, Berlin.

MENDLOVIC, D., ZALEVSKY, Z. & KONFORTI, N., 1997: Computation Considerations and Fast Algorithms for Calculating the Diffraction Integral. – Journal of Modern Optics **44:** 407–414.

OERTEL, D., KAISER, G., JAHN, H. & SCHUSTER, R., 1985: CCD-Sensoren in optischen Meßanordnungen. – Radio Fernsehen Elektron **34:** 490–492.

SANDAU, R. & ECKARDT, A. 1996: The Stereo Camera Family WAOSS/WAAC for Spaceborne/Airborne Applications. – ISPRS XXXI Part B1 Commission **I:** 170–175.

SANDAU, R., BRAUNECKER, B., DRIESCHER, H., ECKARDT, A., HILBERT, S., HUTTON, J., KIRCHHOFER, W., LITHOPOULOS, E., REULKE, R. & WICKI, S., 2000: Design Principles of the LH Systems ADS40 Airborne Digital Sensor. – IAPRS XXXIII, B1, Comm. **I:** 258–265.

SKRBEK, W. & LORENZ, E., 1998: HSRS – An Infrared Sensor for Hot-Spot-Detection. – Infrared Spaceborn Remote Sensing VI, Proceedings of SPIE **3437:** 167–176.

TALBIERSKY, U., 2010: A new Method to Validate the Usage of Fresnel Approximation Instead of Kirchhoff Diffraction Formula for Calculations Concerning Camera Systems. – Proceedings of SPIE **7717**.

Addresses of the Authors:

ULRIKE KRUTZ, ANKO BÖRNER, HERBERT JAHN, CARSTEN PAPROTH, PATRICK SCHERBAUM and EMANUEL SCHLÜSSLER, DLR German Aerospace Center, Department of Optical Information Systems at the Institute of Robotics and Mechatronics, Rutherfordstr. 2, 12489 Berlin, Germany, Tel.: +49-30-67055-511, -509, -510, -566, -502, -571, Fax: +49-30-67055-385, e-mail: first name.last name@dlr.de (ö = oe, ü = ue)

Article

Dense 3D Reconstruction of Low Texture Surfaces Using an Energy Minimization Framework with Smoothness-Based Priors

Ralph Schmidt, Christian Heipke, Manfred Wiggenhagen & Bernd Michael Wolf, Hannover

Summary: This article describes the dense stereoscopic 3D reconstruction of surfaces which offer only low texture by employing a global matching algorithm with smoothness-based priors in an energy minimization framework. The envisaged application areas are high speed image sequences of dynamic processes where the projection of structured light is not applicable. The lack of depth cues on the measured object normally leads to very sparse and often false reconstructions if common local matching algorithms like cross correlation or least squares matching are employed. Within this AiF funded project an operational photogrammetric stereo measurement system has been developed consisting of a stereo rig with high speed cameras and a global matching algorithm. This system allows for the first time a dense reconstruction of surfaces with low texture in high speed image sequences. Quantitative and qualitative results for two test data sets demonstrate that the determination of a dense point cloud of low texture objects without employing structured light is possible.

Zusammenfassung: *Dichte 3D-Rekonstruktion von Oberflächen mit geringer Textur unter Anwendung eines Energieminimierungsverfahrens mit Glattheitsannahmen.* Dieser Artikel beschreibt die dichte stereoskopische 3D-Rekonstruktion von Oberflächen mit geringer Textur unter Anwendung eines globalen Zuordnungsverfahrens mit Glattheitsannahmen in einem Energieminimierungsverfahren. Der angestrebte Einsatzbereich sind Highspeed-Bildsequenzen dynamischer Vorgänge, bei denen die Projektion von strukturiertem Licht nicht möglich ist. Der Mangel an geeigneten Merkmalen am Messobjekt führt bei der Verwendung von üblichen lokalen Zuordnungsverfahren wie Kreuzkorrelation oder Kleinste-Quadrate-Bildzuordnung normalerweise zu einer dünn besetzten und oft falschen Rekonstruktion. Im Rahmen dieses von der AiF geförderten Projektes wurde ein operationell einsetzbares photogrammetrisches Stereomesssystem bestehend aus einem Stereorack mit Highspeed-Kameras und einem globalen Zuordnungsalgorithmus entwickelt. Dieses System ermöglicht erstmals eine dichte Rekonstruktion von Oberflächen mit geringer Textur in Highspeed-Bildsequenzen. Quantitative und qualitative Ergebnisse für zwei Testdatensätze demonstrieren, dass die Bestimmung einer dichten Punktwolke von Objekten mit geringer Textur möglich ist, ohne strukturiertes Licht zu verwenden.

1 Introduction

The three-dimensional reconstruction of static scenes has been a very important research area over the last three decades. For industrial applications mainly two methods are in use today: a) Structured light with la-serline or two-dimensional projector and one or two cameras, b) time-of-flight approaches for laser scanning devices or time-of-flight cameras. While the time-of-flight methods directly measure the depth values respectively distances between the object and the sensor by time measurements, the structured light ap-

proaches obtain depth information from triangulation. Using time-coded light patterns like grey code or time-varying patterns like light stripes an unambiguous correspondence for each image pixel is strived for (Battle et al. 1998, Pagès et al. 2003). These approaches operate in the time domain as several subsequent measurements are necessary for a complete and highly accurate reconstruction of the object or scene. Therefore, these methods are not applicable for dynamic scenes where the object changes its shape and/or position fast in relation to the time that is necessary for recording. Generally, only two dimensional sensors have the potential to capture 3D deformation and motion of a 3D object. An approach operating in the space domain is the conventional photogrammetric setup applying at least two cameras. Often artificial patterns are projected onto the scene to support unambiguous matching even in weakly textured image regions (Kang et al. 1995) which can also be applied to dynamic scenes by reconstructing each frame pair independently. In Davis et al. (2005) and Zhang et al. (2003) a spacetime stereo approach is presented which incorporates the time and space methods into a unifying framework.

In this paper we present an operational photogrammetric stereo measurement system consisting of a stereo rig with high speed cameras and a global matching algorithm which is able to produce a dense point cloud of objects which exhibit low texture. Dense is related here to the aim of determining a disparity value for every pixel of the image. The envisaged application areas are high speed image sequences of dynamic processes. In particular, the surface of an airbag during deployment within a crash test (impact test) should be reconstructed. To our best knowledge no operational projector is available on the market which is able to project a pattern to support correlation because very strong illumination and very high frame rates are needed during the crash tests. Thus, structured light approaches are not applicable. Also especially prepared airbags with imprinted patterns are not feasible since airbags from mass production are used during the tests. Our developed system allows for the first time a dense reconstruction of surfaces with low texture in high speed image sequences. There are no high accuracy requirements as the focus is on a dense and complete reconstruction of the surface of dynamic objects for the analysis of their deformation and motion behaviour. Additionally, for operational reasons the algorithm should be relatively fast which means the user should obtain the results within a few seconds. Also, it should be able to handle image sizes in full HD resolution (1920×1080 pixels). The described work was supported by AiF Arbeitsgemeinschaft industrieller Forschungsvereinigungen "Otto von Guericke" e.V. and thus focuses on technology transfer of innovative solutions.

An overview of local and global matching algorithms is given in section 2. A global matching algorithm using smoothness-based priors in an energy minimization framework, which allows a dense reconstruction of surfaces with low texture and which was developed to solve the given task, is presented in section 3. Quantitative and qualitative results for the reconstruction of two test data sets are shown in section 4. Finally, in section 5 conclusions are drawn and an outlook for future developments is given.

2　Matching

2.1　*Local Matching Algorithms*

Traditional stereo matching methods identify corresponding image points by analyzing the similarity of image patches. Typically, a reference window around the pixel of interest is compared to a search window over a certain search space. In a calibrated setup with two cameras the search space can be reduced to searching along epipolar lines which comply with corresponding image lines in rectified epipolar images. The search space can be further reduced with respect to the expected depth range so that it is not necessary to search along the entire line. One of the simplest similarity measures is the sum of absolute differences (SAD):

$$SAD = \sum_{(x,y) \in W_S} \left| I_r(x,y) - I_l(x,y) \right| \qquad (1)$$

where I_r are the intensity values of the right image, I_l the intensity values of the left image and W_s is the spatial aggregation window around the pixel of interest. Numerous other similarity measures have been developed which mainly aim at accounting for radiometric differences between the two images (HIRSCHMÜLLER & SCHARSTEIN 2009). The final corresponding pixel is selected by simply choosing the pixel in the second image with the lowest SAD which is commonly referred to as "winner-take-all strategy". The calculated pixel offset is called disparity or parallax. However, these local matching approaches impose an implicit smoothness assumption upon the scene which means that no depth discontinuity is allowed to lie within the aggregation window. The reason is that depth discontinuities lead to an unequal object appearance in the images when viewed from different perspectives. Therefore, the matching

window has to be as small as possible to reduce the probability of including discontinuities in depth or depth change. On the other hand, small windows may contain too little information for unambiguous matching and are sensitive to noise so that in the matching strategy there is always a tradeoff in choosing an appropriate window size.

In Fig. 1 the influence of different window sizes is shown using the example of a scene depicting the inner side of a car door without interior paneling. The reference result in Fig. 1d was produced by projecting different noise patterns on the door to support correspondence and employing a spacetime matching algorithm like in DAVIS et al. (2005). A 1×1 space window, i. e. the single pixels and no spatial aggregation window were used with 12 time windows, i. e. 12 different noise patterns. Without the projected texture the aggregation window has to be very large (45×45

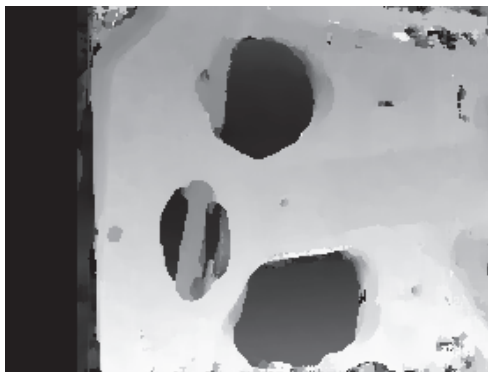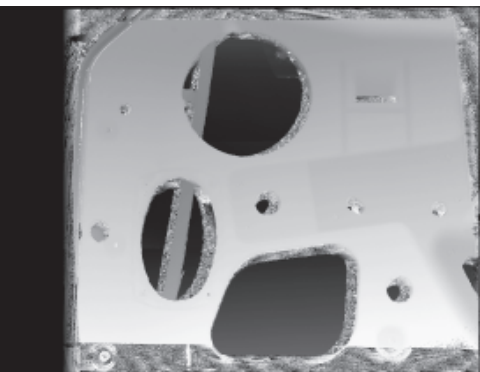
a) Image of the car door
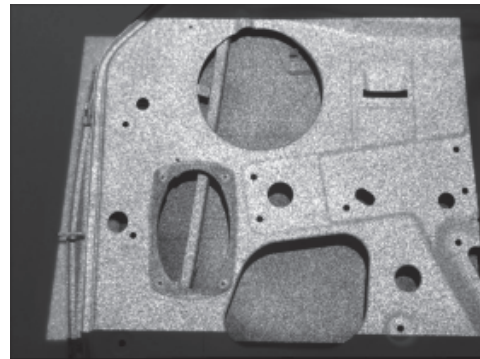
b) Image with projected texture

c) Disparity map of the car door image using a 45×45 pixels window

d) Reference disparity map using a 1 × 1 × 12 pixels spacetime window

Fig. 1: Influence of different aggregation window sizes.

pixels in this case) to gather enough grey value variation to allow a reliable correspondence search (Fig. 1c). The determined disparities are encoded as grey values and stretched to the range 0–255 so that the shown disparity maps are obtained. It can be observed that the large aggregation window oversmoothes small features. Especially at the edges of holes – which mark disparity jumps – it can be observed that the locations of the edges are displaced. This phenomenon is usually referred to as "foreground fattening" (Scharstein & Szeliski 2002) where pixels from the far surface are wrongly assigned the same disparity as pixels on the near surface.

2.2 Global Matching Algorithms

To avoid the problems of the local matching techniques global strategies have been developed which calculate the disparity map for the entire image by formulating the problem as an energy minimization framework (Terzopoulos 1986):

$$E(d) = E_{data}(d) + \lambda E_{smooth}(d) \qquad (2)$$

The data term $E_{data}(d)$ measures the pixelwise similarity, which means how well the disparity function d is consistent with the input images:

$$E_{data}(d) = \sum_{(x,y)} C(x, y, d(x, y)) \qquad (3)$$

Pixelwise similarity means that no aggregation window like in eq. 1 is necessary to compute the matching cost C though in principle this is also possible. The term $E_{smooth}(d)$ in eq. 2 explicitly encodes smoothness assumptions about the disparity function which is weighted by factor λ. These smoothness priors support the generation of reasonable disparity values over noisy and low texture areas. The smoothness term can e. g. be the sum of spatially varying smoothness costs for all 4-connected direct neighbours:

$$E_{smooth}(d) = \sum_{\{p,q\} \in N} w_{p,q} \cdot V(|d_p - d_q|) \qquad (4)$$

where q is a vertical or horizontal direct neighbour to pixel position $p = (x,y)$ and N is the set of all neighbouring pixel pairs. The smoothness term is the product of a function V of disparity difference and optional spatially varying weights $w_{p,q}$ for each pixel pair. The weights can for instance be computed by an edge detector because disparity discontinuities often coincide with intensity edges. Disparity differences between neighbouring pixels (first derivative) are penalized by this energy function where bigger differences lead to higher penalties. Second order smoothness terms which penalize the curvature of the disparity function require triple cliques rather than pairs, i. e. three consecutive neighbouring pixels (Woodford et al. 2009). Unfortunately, this algorithm only works for very small images and is computationally very demanding.

The energy can be viewed as an objective function of a Markov random field (MRF) (Geman & Geman 1984) where a minimum of the energy corresponds to a maximum a posteriori (MAP) estimate. Finding the best result (global minimum) requires an exhaustive search over all candidate solutions which is not applicable here because the problem is NP-hard (Boykov et al. 2001), i. e. the computational complexity of the problem takes non-deterministic polynomial-time to solve. Therefore, algorithms look for a good approximate solution, i. e. a local minimum. On the other hand, the global minimum may not be the best result anyway because the energy function might not model the real world correctly. Early algorithms for energy minimization like iterated conditional modes (ICM) (Besag 1986) or simulated annealing (Barnard 1989) were comparatively ineffective. Besides having a very slow convergence behaviour these algorithms only find a good solution if a single dominant global minimum exists which is usually not the case with the energy functions employed for stereo matching. During the last years significant progress has been made in developing powerful algorithms like graph cuts (Boykov et al. 2001) or message passing algorithms like belief propagation (Sun et al. 2003). These global matching strategies produce excellent disparity maps and mark the state-of-the-art (Scharstein & Szeliski 2007).

An interesting alternative is semiglobal matching (Hirschmüller 2008) which approximates the global 2D smoothness constraints of the MRF by combining several 1D optimization paths. Thus, a significant reduction of the computational time is achieved. Another principle of incorporating smoothness constraints provide variational methods which also minimize an energy function with a data and a smoothness term (Poggio et al. 1985).

3   Selected Matching Algorithm

In this section we present our global matching algorithm with smoothness-based priors which support the propagation of reasonable disparity values over low texture areas. Initial tests with semiglobal matching and a variational approach using the energy functional of Slesareva et al. (2005) with a multigrid method for energy minimization did not achieve satisfactory results on our special data sets. Therefore, we focus on the MRF formulation.

At first the similarity measure for the data term $E_{data}(d)$ is chosen. Absolute differences (AD) are one of the simplest matching costs which penalize dissimilarity. However, they presume photo consistency which means that corresponding points should have the same grey value in the stereo image pair. In our experiments we found that AD gave poor results because of the violation of this assumption due to different viewing directions of the cameras resulting in unequal illumination conditions and reflectance behaviour. Therefore, we use the census transform as matching cost (Zabih & Woodfill 1994) which has been shown to have the best performance in the presence of local brightness differences (Hirschmüller & Scharstein 2009). The census transform is a non-parametric matching cost which is based on the local order of the grey values. A bit string is generated where each bit corresponds to one of the neighbourhood pixels around the current pixel of interest. If the neighbourhood pixel has a lower grey value than the centre pixel the bit is set. In our implementation the bit strings are calculated over a 9×7 local window and are stored in a 64 bit integer variable. The final matching cost value is determined by calculating the Hamming distance (Hamming 1950) between the bit strings of the left and the right image. The Hamming distance is simply the number of positions where the corresponding bits are different. The computation involves a "bitwise exclusive or" step and the counting of the nonzero bits which can be implemented very efficiently on modern CPUs.

For the smoothness term $E_{smooth}(d)$ several different forms are possible. A truncated version of the smoothness penalty V is used here which ensures that the penalty cannot be higher than V_{max}:

$$V(|\,d_p - d_q\,|) = \min(|\,d_p - d_q\,|^k, V_{max}) \qquad (5)$$

A truncated term is discontinuity-preserving and does not favour depth discontinuities with large disparity differences over smaller differences because neither is assumed to be more probable than the other. We use the L_1 distance with $k = 1$ but in principle a quadratic version with $k = 2$ or the Potts model ($V_{max} = 1$) is possible, too. The energy function can also be extended with an additional term for handling occlusions (Kolmogorov & Zabih 2001) but as occlusions did not pose a problem in our experiments we did not employ such a term.

For energy minimization we use an optimized version of the tree-reweighted message passing (TRW) (Wainwright et al. 2005) algorithm called sequential TRW (TRW-S) (Kolmogorov 2006). While the original TRW was motivated by maximizing a lower bound of the energy it is not guaranteed that this bound be increased over the iterations. The algorithm also may not converge, a problem which can be observed with belief propagation, too. TRW-S guarantees not to decrease the lower bound, it always converges and it has been shown that it often achieves superior results compared to graph cuts or belief propagation (Szeliski et al. 2008). Another advantage of practical importance is that it only consumes half as much memory as traditional message passing algorithms. A detailed description of the message passing scheme is outside the scope of this paper; it can be found in the relevant literature (Pearl 1988, Wainwright et al. 2005, Kolmogorov 2006).

4 Experiments

4.1 *Hardware Setup*

The application area is the processing of high speed image sequences recorded by high performance cameras like pco.dimax (www.pco.de/). A stereo rig shown in Fig. 2a allows capturing high speed stereoscopic image sequences at up to 1,300 fps with full 2000×2000 pixels resolution with 12bit dynamic. The SOLVing3D.titan system uses only one camera and a beamsplitter (s3d.camsplitter) (Fig. 2b) which provides a cost effective alternative and avoids the problem of synchronization but image size is reduced by half. Higher image rates of up to 150,000 fps are achievable at the cost of a reduced image size, e. g. in a typical beamsplitter setup two 500×500 pixels images at 9,000 fps are acquired.

For the evaluation of the algorithm described above two test data sets have been created. The first data set consists of a stereo pair of an inflated airbag. As can be seen in Fig. 3a, the images show only very little grey value variations. For technical reasons only one stereo pair could be recorded rather than a complete sequence. Additionally, another stereo pair of the same scene with a projected speckle pattern was recorded which was used to obtain a reference disparity map as ground truth (Fig. 3b). This disparity map was generated using a local matching algorithm with a window size of 5×5 pixels. Because of the technical limitations to project structured light in order to capture ground truth data with high speed image sequences – in fact this was the motiva-

tion for this project – still images were used. For the second data set a white styrofoam head was used which also hardly exhibits any texture but in contrast to the first data set contains small features like eyes, nose and mouth (Fig. 4). In order to generate a high quality reference data set the head was captured by employing a spacetime stereo approach (Davis et al. 2005) using a 3×3 space window and 12 different speckle patterns.

4.2 *Results*

To assess the quality of the stereo reconstruction, first a visual inspection of the resulting disparity map was made. The result for the airbag obtained without using projected texture is displayed in Fig. 5a and from the stereo pair with projected speckle pattern in Fig. 5b. The search range in the rectified epipolar images amounts to about 100 pixels. The black area in the left part of the disparity map stems from a constant parallax offset. The parameter λ was set to 20 and V_{max} to 7. Because there are no disparity discontinuities that coincide with intensity edges on the smooth surface of the airbag the influence of the weights $w_{p,q}$ were set to 0. These parameters were determined in an iterative procedure by visually inspecting the result. The TRW-S algorithm has been iterated only five times. In principle a stop criterion for energy minimization could be defined, but we found that typically after five iterations the change is negligible. Remarkably, we were able to reconstruct the whole surface of the airbag without any gaps, holes or other gross errors. The shape of the airbag is clearly
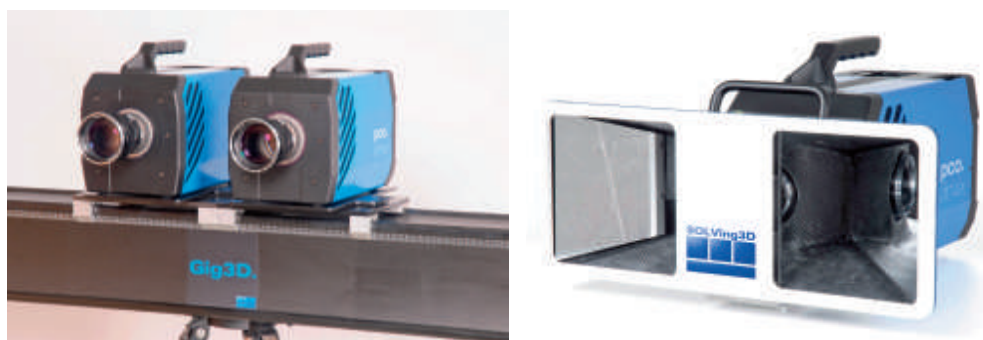
Fig. 2: a) pco.dimax in a stereo rig setup, b) With mounted beamsplitter.

visible. On the other hand the disparity map does not display a surface as smooth as the reference but exhibits small stepwise disparity jumps. The reason is that the prior of the form given in eq. 5 enforces a bias towards fronto-parallel surfaces over which the disparity is constant. The costs for the reconstruction of fronto-parallel planes are always lower
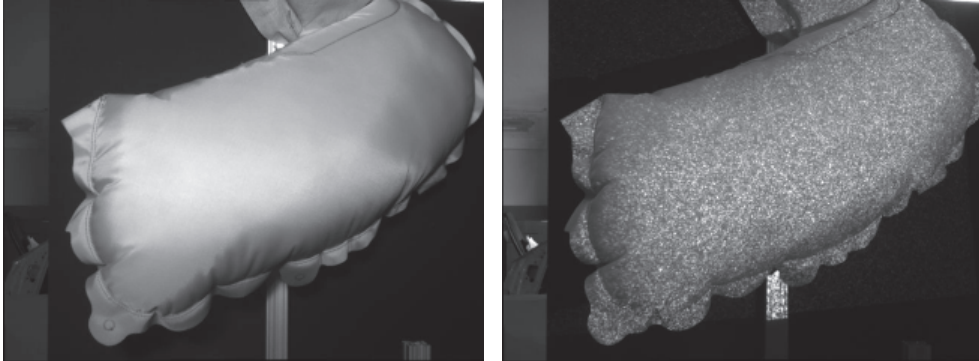
Fig. 3: a) Airbag test image, b) Airbag test image with projected speckle pattern.
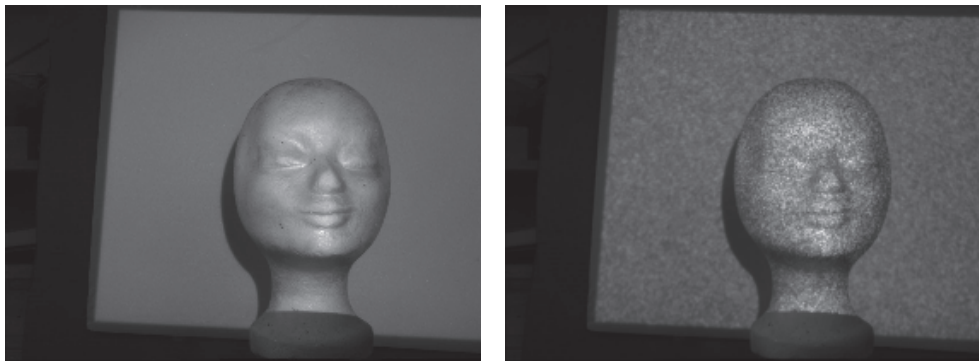
Fig. 4: a) Styrofoam head test image, b) Styrofoam head test image with projected speckle pattern, twelve different patterns were used for spacetime stereo.
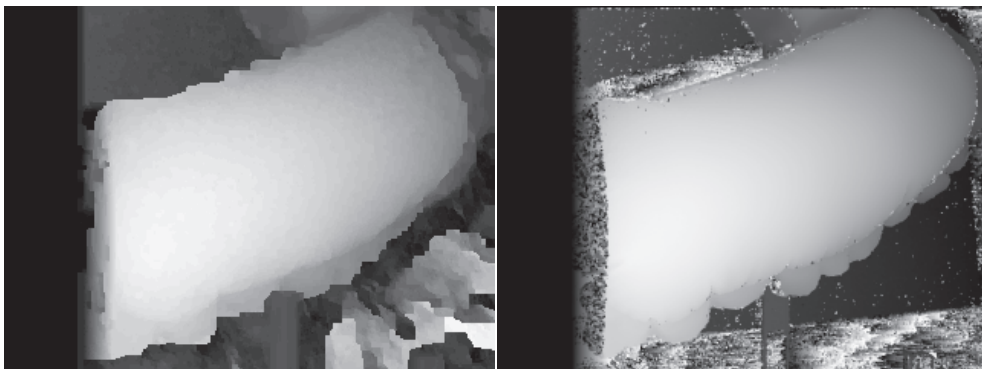
Fig. 5: a) Disparity map airbag test image, b) Reference disparity.

than for slanted surfaces with several small disparity jumps. Therefore, there is a tendency that slanted surfaces are reconstructed as a sequence of several small fronto-parallel surface patches.

The result for the styrofoam head is displayed in Fig. 6. The search range amounts to about 50 pixels because the background has not been incorporated into the range. This fact results in a noisy pattern but in our application the background is not of interest. The influence of the smoothing term was reduced a little bit by setting λ to 10 in order to preserve more details; V_{max} was set to 20. The computed disparity map is also not as smooth as the reference which is again an effect of the smoothness term's tendency to favour fronto-parallel surfaces. Nevertheless, the details of the face

like eyes, nose and mouth are clearly visible. Owing to the edge preserving property of the smoothness term of the energy function such small details could also be reconstructed. Generally, the parameters had to be tweaked carefully to our class of textureless data sets to achieve good results. Nevertheless, once set only small adaptations of λ and V_{max} are necessary in order to achieve optimal results. The processing took about 15 to 25 seconds on a current CPU which is an acceptable time in our use case.

In order to obtain a quantitative measure of the quality of the resulting disparity map a difference image was calculated between the computed and the reference disparity values. The resulting error map shows the absolute differences >1 of the disparity values (Fig. 7).

Fig. 6: a) Disparity map styrofoam head test image, b) Reference disparity.

a) Airbag error map   b) Styrofoam head error map

Fig. 7: Error maps displaying the absolute differences to ground truth >1.

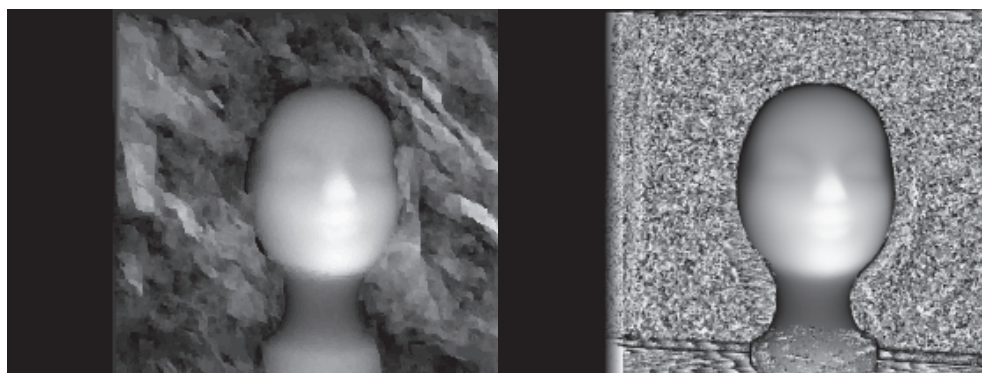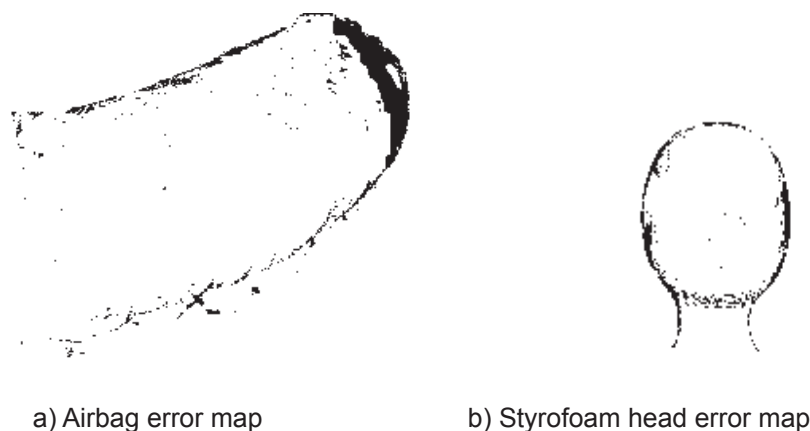Only the errors at the object have been considered, the background was masked out. The differences due to the fronto-parallel surface patches cannot be observed in the airbag test image because they lie in the subpixel range. Larger errors can only be found at the border of the object. Additionally, there is a small area in the back near the border which shows larger differences. The reason for this behaviour is currently unclear. In principle, for the styrofoam head test image the same observations can be made: The surface is not as smooth as the reference and shows errors at the border of the object.

In order to obtain global quantitative quality measures root mean square error (RMSE) and the percentage of erroneously matched pixels are given (SCHARSTEIN & SZELISKI 2002):

$$RMSE = \sqrt{\frac{1}{N}\sum_{(x,y)}|d_C(x,y)-d_R(x,y)|^2} \qquad (6)$$

$$B = \frac{1}{N}\sum_{(x,y)}(|d_C(x,y)-d_R(x,y)|> \delta_d) \qquad (7)$$

where $d_C(x,y)$ is the computed and $d_R(x,y)$ is the reference disparity map. N is the number of pixels in the image and δ_d is the error threshold which is set to 1 here. A differentiation into textureless, occluded and depth discontinuity regions like in SCHARSTEIN & SZELISKI (2002) was not performed because we mainly focus on textureless objects. For the airbag test data set we obtained a RMSE of 1.72 and an error percentage of 6.6 %. The values

for the head data set are slightly worse with a RMSE of 2.85 and an error percentage of 8.7 %. The RMSE values seem to be quite high but in consideration of the fact that we reconstructed two nearly textureless objects we did not expect to reach subpixel accuracy. Compared to the Middlebury evaluation ranking (SCHARSTEIN & SZELISKI 2009) our error percentage did not achieve a top score but again in consideration of our nearly textureless objects the values are very good.

In addition to the overall error, in Fig. 8 histograms show the distribution of the amount of the absolute differences to ground truth. As can be seen, the average error amounts to 1 disparity step with a few pixels having a difference of two steps. A negligible amount of pixels exhibit outliers which mostly can be found at the edges of the object or at the erroneously reconstructed small area on the airbag. However, experience with the results of the Middlebury evaluation ranking show that without projecting structured light or a speckle pattern it is hardly possible to avoid such effects.

Overall, it can be stated that both test objects could be accurately reconstructed without projecting structured light. Hence, for the first time it is possible to stereoscopically analyze the deformation and motion behaviour of objects in high speed image sequences. The requirements of a short processing time and the handling of images in HD size are fulfilled. However, high precision measurements with subpixel accuracy are not possible with
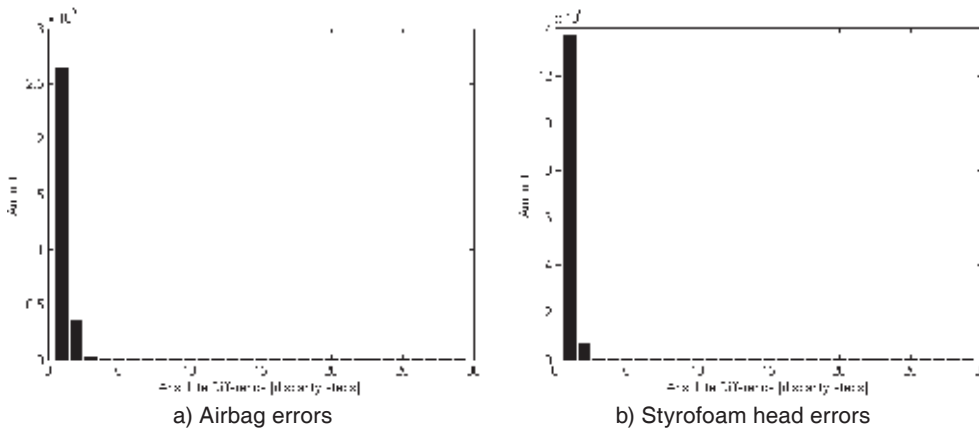

a) Airbag errors

b) Styrofoam head errors

Fig. 8: Histogram displaying the absolute differences to ground truth.

this method but for the envisaged application areas like the analysis of the inflation behaviour of an airbag the obtained accuracy is sufficient.

5   Conclusions and Outlook

We presented an operational photogrammetric stereo measurement system which allows for the first time a dense reconstruction of surfaces with low texture in high speed image sequences. It has been shown that it is possible to generate reasonable disparity values over noisy and low texture areas of an object by employing a global matching strategy with smoothness prior. Matching approaches using small local windows usually fail at this task because they do not contain sufficient unique and discriminating information for reliable correlation. Very large windows are not an option because of the foreground fattening effect. The prior helps in finding the correct solution taking into account the smoothness assumption. However, this smoothness assumption results in favouring fronto-parallel surfaces over slanted or highly curved surfaces. Obviously, this circumstance does not always model real objects or scenes correctly which has been shown in our experiments. Nevertheless, for our application area the algorithm delivers useful results. The average deviation to the two ground truth data sets is only about one pixel. This does not constitute a high accuracy measurement but the quality is sufficient for the analysis of the deformation and motion behaviour of objects.

The matching algorithm could be improved by using second order smoothness constraints like in WOODFORD et al. (2009) in order to model slanted surfaces more accurately without favouring fronto-parallel surfaces. Unfortunately, this algorithm has limitations in operational systems because it only works for very small images and is computationally very demanding.

The MRF used in our investigation assumes conditional independence of the variables which might not result in a realistic posterior distribution. In principle this assumption can be relaxed by employing conditional random fields (CRFs) which learn the free parameters of the MRF from ground truth data sets (PAL et al. 2011). However, like models with second order smoothness constraints this method has not reached an operational status yet.

References

BARNARD, S., 1989: Stochastic Stereo Matching over Scale. – International Journal of Computer Vision **3** (1): 17–32.

BATTLE, J., MOUADDIB, E. & SALVI, J., 1998: Recent Progress in Coded Structured Light as a Technique to Solve the Correspondence Problem: A Survey. – Pattern Recognition **31** (7): 963–982.

BESAG, J., 1986: On the Statistical Analysis of Dirty Pictures. – Journal of the Royal Statistical Society, Series B **48** (3): 259–302.

BOYKOV, Y., VEKSLER, O. & ZABIH, R., 2001: Fast Approximate Energy Minimization via Graph Cuts. – IEEE Transactions on Pattern Analysis and Machine Intelligence **23** (11): 1222–1239.

DAVIS, J., NEHAB, D., RAMAMOORTHI, R. & RUSINKIEWICZ, S., 2005: Spacetime Stereo: A Unifying Framework for Depth from Triangulation. – IEEE Transactions on Pattern Analysis and Machine Intelligence **27** (2): 296–302.

GEMAN, S. & GEMAN, D., 1984: Stochastic Relaxation, Gibbs Distributions, and the Bayesian Restoration of Images. – IEEE Transactions on Pattern Analysis and Machine Intelligence **6** (6): 721–741.

HAMMING, R.W., 1950: Error Detecting and Error Correcting Codes. – Bell System Technical Journal **29** (2): 147–160.

HIRSCHMÜLLER, H., 2008: Stereo Processing by Semiglobal Matching and Mutual Information.

– IEEE Transactions on Pattern Analysis and Machine Intelligence **30** (2): 328–341.

HIRSCHMÜLLER, H. & SCHARSTEIN, D., 2009: Evaluation of Stereo Matching Costs on Images with Radiometric Differences. – IEEE Transactions on Pattern Analysis and Machine Intelligence **31** (9): 1582–1599.

KANG, S.B., WEBB, J., ZITNICK, L. & KANADE, T., 1995: A Multibaseline Stereo System with Active Illumination and Real-Time Image Acquisition. – Proceedings Fifth International Conference on Computer Vision: 88–93.

KOLMOGOROV, V. & ZABIH, R., 2001: Computing Visual Correspondence with Occlusions using Graph Cuts. – Proceedings IEEE International Conference on Computer Vision **2:** 508–515.

KOLMOGOROV, V., 2006: Convergent Tree-Reweighted Message Passing for Energy Minimization. – IEEE Transactions on Pattern Analysis and Machine Intelligence **28** (10): 1568–1583.

PAGÈS, J., SALVI, J., GARCÍA, R. & MATABOSCH, C., 2003: Overview of Coded Light Projection Techniques for Automatic 3D Profiling. – Proceedings IEEE International Conference on Robotics and Automation **1:** 133–138.

PAL, C., WEINMAN, J., TRAN, L. & SCHARSTEIN, D., 2011: On Learning Conditional Random Fields for Stereo. – International Journal of Computer Vision, doi: 10.1007/s11263-010-0385-z.

PEARL, J., 1988: Probabilistic Reasoning in Intelligent Systems: Networks of Plausible Inference. – Morgan Kaufmann Publishers, San Francisco, California.

POGGIO, T., TORRE, V. & KOCH, C., 1985: Computational Vision and Regularization Theory. – Nature **317** (6035): 314–319.

SCHARSTEIN, D. & SZELISKI, R., 2002: A Taxonomy and Evaluation of Dense Two-Frame Stereo Correspondence Algorithms. – International Journal of Computer Vision **47** (1): 7–42.

SCHARSTEIN, D. & SZELISKI, R., 2007: http://vision.middlebury.edu/stereo/ (13.11.2011).

SCHARSTEIN, D. & SZELISKI, R., 2009: http://vision.middlebury.edu/stereo/eval/ (13.11.2011).

SLESAREVA, N., BRUHN, A. & WEICKERT, J., 2005: Optic Flow Goes Stereo: A Variational Method for Estimating Discontinuity-Preserving Dense Disparity Maps. – Lecture Notes in Computer Science **3663:** 33–44.

SUN, J., ZHENG, N.N. & SHUM, H.Y., 2003: Stereo Matching using Belief Propagation. – IEEE Transactions on Pattern Analysis and Machine Intelligence **25** (7): 787–800.

SZELISKI, R., ZABIH, R., SCHARSTEIN, D., VEKSLER, O., KOLMOGOROV, V., AGARWALA, A., TAPPEN, M. & ROTHER, C., 2008: A Comparative Study of Energy Minimization Methods for Markov Random Fields with Smoothness-Based Priors. – IEEE Transactions on Pattern Analysis and Machine Intelligence **30** (6): 1068–1080.

TERZOPOULOS, D., 1986: Regularization of Inverse Visual Problems Involving Discontinuities. – IEEE Transactions on Pattern Analysis and Machine Intelligence **8** (4): 413–424.

WAINWRIGHT, M., JAAKKOLA, T. & WILLSKY, A., 2005: MAP Estimation via Agreement on Trees: Message-Passing and Linear Programming. – IEEE Transactions on Information Theory **51** (11): 3697–3717.

WOODFORD, O., TORR, P., REID, I. & FITZGIBBON, A., 2009: Global Stereo Reconstruction under Second-Order Smoothness Priors. – IEEE Transactions on Pattern Analysis and Machine Intelligence **31** (12): 2115–2128.

ZABIH, R. & WOODFILL, J., 1994: Non-parametric Local Transforms for Computing Visual Correspondence. – Proc. 3rd European Conf. on Computer Vision **2:** 151–158.

ZHANG, L., CURLESS, B. & SEITZ, S.M., 2003: Spacetime Stereo: Shape Recovery for Dynamic Scenes. – Proceedings IEEE Conference on Computer Vision and Pattern Recognition: 367–374.

Addresses of the Authors:

Dr.-Ing. RALPH SCHMIDT, Prof. Dr.-Ing. habil. CHRISTIAN HEIPKE, Dr.-Ing. MANFRED WIGGENHAGEN, Leibniz Universität Hannover, Institut für Photogrammetrie und GeoInformation, Nienburger Str. 1, 30167 Hannover, Germany, Tel.: +49-511-762-2484, Fax: +49-511-762-2483, e-mail: surname@ipi.uni-hannover.de

Dr.-Ing. BERND MICHAEL WOLF, SOLVing3D GmbH, Osteriede 8-10, 30827 Garbsen, Germany, Tel.: +49-5131-907972-0, Fax: +49-5131-907972-9, e-mail: bernd-m.wolf@solving3d.de

Berichte von Veranstaltungen

XXIII. CIPA Symposium, 11.–16. September 2011, Prag, Tschechien

Prag, die goldene Stadt, Weltkulturerbe, Sitz der ältesten deutschsprachigen Universität, eine Metropole, die ihre historische Substanz in ihrem weitläufigen lebendigen Kern beidseits der Moldau weitgehend bewahrt hat, bot den angemessenen Rahmen als Tagungsort, um diejenigen Experten, die unser Kulturerbe sichern, beschreiben, bewerten, dokumentieren, restaurieren und konservieren, zusammenzubringen mit jenen, welche die messtechnischen Voraussetzungen hierzu schaffen. CIPA, (Comité international de photogrammétrie architecturale), besteht bereits seit 1969 als quasi bipolare Organisation, gegründet mit dem Ziel, Fachleute dieser zwei unterschiedlichen Fachgebiete, nämlich Experten aus Architektur, Baudokumentation, Bauforschung und Restaurierung auf der einen Seite und Fachleute zu Aufnahmetechniken wie Photogrammetrie und den inzwischen weiter entwickelten Möglichkeiten zur metrischen und bildlichen Erfassung und Darstellung auf der anderen Seite zusammenzuführen. Dementsprechend wird CIPA getragen von der ISPRS (International Society for Photogrammetry and Remote Sensing) einerseits und dem ICOMOS (International Council on Monuments and Sites) unter dem Dach der UNESCO andererseits.

Tagungsort war die Technische Universität (CTU), wo sich bereits am Vorabend der Tagungswoche bei einem zwanglosen Treffen im Foyer des Gebäudes der Fakultät für Bauingenieurwesen die Gelegenheit bot, Kontakte zu pflegen oder zu knüpfen. Alle Begegnungen spielten sich hier bzw. in den Hörsaaltrakten beidseits dieses geräumigen Licht durchfluteten hohen Atriums ab, das großzügig verglast und mit üppigem Grün ausgestattet an eine Orangerie erinnerte. Die exotisch angehauchte Atmosphäre begünstigte die Begegnung mit den Ausstellern ebenso wie die Gespräche der Tagungsteilnehmer untereinander während Mittagsmahlzeiten oder Kaffeepausen.

Die Plenarsitzung leitete als Organisator Karel Pavelka, (Faculty of Civil Engineering, Department of Mapping and Cartography). Nach dem Plädoyer des Vizerektors, einem Architekten, für das „Fusionsanliegen" von CIPA eröffnete der Präsident von CIPA, Mario Santana-Quintero, das Symposium. Orhan Altan, Präsident der ISPRS, erinnerte an seine engen Bindungen an CIPA, nämlich als Organisator des CIPA-Symposiums 2003, und unterstrich die Bedeutung der Träger ISPRS und ICOMOS. Der ehemalige CIPA-Präsident Cliff Ogleby warb als Direktor des ISPRS Kongresses 2012 mit einem Video für den Tagungsort Melbourne (siehe auch www.ISPRS2012.org).

Den Grußadressen folgten drei Plenarvorträge: Bernd Breuckmann, Gründer der gleichnamigen Firma mit Schwerpunkt Objekterfassung mittels Musterprojektion, stellte die Methodik mit ihren unterschiedlichen Schattierungen dar und zeigte herausragende Beispiele. Ondřej Humola wies den Weg vom herkömmlichen 3D-Modell zum perfekten Abbild der Natur durch Einbeziehung von z.B. Reflektion, Überstrahlung und Transparenz – auch am Beispiel der Rekonstruktion von Barockgärten. Jan Buriánek schließlich verblüffte mit seiner Reportage über die 3D-Visualisierung des weltweit einzigartigen kleinmaßstäbigen, mit ca. 13.400 Dachflächen äußerst detailreichen Modell Prags des Lithografen und genialen Modellbauers Antonin Langweil aus den Jahren 1826–1837, für das teils spezielle Aufnahmegeräte und -techniken entwickelt wurden.

Alle folgenden Vorträge wurden innerhalb parallel angesetzter Sessionen gehalten mit der Qual der Wahl bei Überschneidung der Interessen. Die Sitzungen waren den folgenden Themenbereichen zugeordnet: *Aufnahme, Dokumentation und lnformationsmanagement des Kulturerbes und Bewahrung des archäologischen und des architektonischen Erbes (A-1), Terrestrische und Luftbild-Photogrammetrie und ihre Anwendungen auf das Kulturerbe (A-2), Terrestrisches und Airborne-Laserscanning, Mobile-Mapping und Anwen-*

dungen auf das Kulturerbe (A-3), Anwendungen der Fernerkundung bei der Erfassung des Kulturerbes (A-4), GIS bei der Dokumentation des Kulturerbes (B-1), 3-D Modellierung, Animation, Rekonstruktion und Visualisierung des Kulturerbes (B-2), Anwendung von Web-Techniken mit Bezug zum Kulturerbe (B-3), Multisensor-Systeme für die Erfassung des Kulturerbes und neue Sensoren (B-4), Recht an geistigem Eigentum und Open Source mit Bezug zum kulturellen Erbe (C-1), Standards – Richtlinien für die Dokumentation des Kulturerbes (C-2), Strategien für die langfristige Archivierung digitaler Informationen des Kulturerbes, Präventionsmaßnahmen zum Schutz des Kulturerbes vor Risiken und Gefährdung (C-3), Erziehung, Training und Kommunikation (C-4).

Der Schwerpunkt der Beiträge lag bei den zwei Themenkreisen A-1 (23 Beiträge) und B-2 (29 Beiträge). Diese Gewichtung drückt aus, wie sehr die Erfassung und die Darstellung des Kulturerbes die Mitglieder CIPAs bewegen. Bei den Aufnahmeverfahren stehen Laserscanning und fortentwickelte weitgehend automatisierte photogrammetrische Verfahrensweisen im Vordergrund. Manche Beiträge sehen eine gewisse Konkurrenz um Genauigkeit, Vollständigkeit und Schnelligkeit der Aufnahme, andere berichten über Versuche, die verfahrenstypischen Eigenschaften zu integrieren. Neben dem Widerstreit der Methoden findet gleichzeitig also auch eine Annäherung statt.

Es fällt auf, dass es insbesondere beim terrestrischen Laserscanning nach Jahren der hard- und softwaremäßigen rasanten Fortentwicklung zu einer gewissen Konsolidierung gekommen ist. In erheblichem Umfang wird nämlich über Anwendungen berichtet, die zwar im Einzelfall besondere Herausforderungen bedeuten, die aber mit den bekannten Werkzeugen gelöst werden. Die Fülle der dargebotenen Beispiele mag diejenigen ermutigen, die den modernen Verfahren noch etwas skeptisch gegenüber stehen; deren Zahl schwindet aber auch auf Seiten der Anwender. Mit zunehmender Detailtreue der Modelle wachsen jedoch auch die Ansprüche der Abnehmer, also des nicht-technischen Parts von CIPA, z.B. um Forschungen am virtuellen Modell zu ermöglichen und so das reale Kul-

turerbe zu schonen oder den Zugang einem breiteren Kreis überhaupt zu ermöglichen.

In diesem Kontext ist eine spezielle Parallelsession zu sehen, die der besonderen Bedeutung der zurzeit diskutierten Charta von Sevilla (The Seville Charter – International Charter Of Virtual Archaeology) gewidmet war, mit der einheitliche Grundsätze zur digitalen virtuellen Dokumentation für die Praxis etabliert werden sollen. Eine die Session abschließende Diskussion zeigte den Willen zur Vereinheitlichung, aber auch die Probleme, will man dies bei einem so sehr in Bewegung befindlichen Gebiet erreichen.

Parallel zum Vortragsteil fand im lichten Foyer eine stets gut besuchte Firmenpräsentation mit ca. 20 Ausstellern statt: Firmen, die Hardware anbieten, Softwareentwickler aus den Bereichen Datenaufbereitung, -management und GIS sowie Dienstleistungsunternehmen.

Auf die drei Vortragstage folgte der Donnerstag als Tag der Fachexkursionen. Hier wurde ein neues Konzept erprobt: Nicht ein gemeinsames Ziel für alle Exkursionsteilnehmer, sondern unterschiedliche Zielgebiete, um unterschiedlichen Interessensschwerpunkten Rechnung zu tragen. Über die touristische Führung hinaus waren stets besondere fachliche Schwerpunkte gesetzt, teils in Form fachkundlicher Detailberichtung auf der denkmalpflegerischen Seite, teils durch Demonstration der konkreten Aufnahmemethodik.

Drei Stätten standen zur Wahl:
- Burg Karlštejn, wobei der photogrammetrischen Dokumentation der gotischen Wandgemälde besondere Aufmerksamkeit zukam,
- die Stadt Kutná Hora (Kuttenberg), wegen der Silberminen nach Prag wichtigste Stadt des Böhmischen Königreichs im Mittelalter und
- Karlsbad, mit seinen prächtigen Gebäuden nationales Kulturdenkmal.

Den gesellschaftlichen Höhepunkt bildete der Abendempfang im prachtvollen Rathaus der Stadt Prag, bei dem es der Bürgermeister sich nicht nehmen ließ, die Gäste persönlich zu begrüßen.

Der Freitag war der einzigen Postersession und der Abschlussveranstaltung vorbehalten. Die Themen der meisten der 40 Poster ent-

sprachen in ihrer Verteilung etwa den geschilderten Themenschwerpunkten des Vortragsteils, also Aufnahme und Dokumentation. Wie bei früheren Symposien wurden die besten Poster ausgezeichnet, darunter auch wieder ein deutscher Beitrag, der von Susanne Lipkowski und Michael Scherer (Universität Bochum) zur Kalibrierung von 3D-ToF-Kameras. Zum Abschluss zog der Präsident von CIPA, Mario Santana-Quintero, Bilanz: 190 Teilnehmer aus 29 Nationen trugen mit 155 Beiträgen zum Erfolg bei, darunter 51 „peer reviewed papers". Abschließend lud Pierre Grussenmeyer zum nächsten Symposium 2013 in Straßburg (Frankreich) ein. Vorher, bereits im August 2012, findet die gemeinsame CIPA–VSMM (Virtual Systems and MultiMedia)-Tagung im Rahmen des ISPRS-Kongresses in Melbourne, Australien, statt.

Anstelle eines Tagungsbandes erhielten die Teilnehmer erstmals lediglich eine CD mit den Beiträgen, d.h. den Papern zu den Vorträgen und zu den Postern. Alle Artikel sind im Internet einsehbar unter http://cipa.icomos.org/prague.html bzw. http://www.cipa2011.cz/cipa/.

Abschließend sei eine Zwischenfrage des Ehrenpräsidenten von CIPA, Peter Waldhäusl, wiedergegeben, deren Beantwortung uns alle beschäftigen sollte, und die es vordringlich zu lösen gilt: Wie, wo und durch wen werden all' die hervorragenden digitalen Dokumente und virtuellen Modelle zum Kulturerbe gesammelt, gespeichert und so aufbereitet, dass sie langfristig gesichert sind und durch eine breite Anzahl von Anwendern auch in Zukunft genutzt werden können?

Michael Scherer, Bochum

UAV-g 2011 Conference – Unmanned Aerial Vehicles in Geomatics, 14.–16. September 2011, Zürich, Schweiz

UAVs (Unmanned Aerial Vehicles) sind hoch entwickelte Geräte mit breitem Anwendungsgebiet. Sie dokumentieren archäologische Ausgrabungen, überwachen Naturgefahren (Hangrutschungen, Überflutungen, Vulkangebiete etc.) und werden für die Dokumentation von Kiesgruben und Baustellen eingesetzt.

Sie machen Aufnahmen von Agrar- und Forstwirtschaftsflächen, übernehmen Mapping-Aufgaben oder werden im Katasterwesen in Kombination mit herkömmlichen Aufnahmeverfahren gebraucht.

Die UAV-g 2011-Konferenz brachte 220 Wissenschaftler, Anwender, Behördenvertreter und Hersteller aus 30 Ländern an die ETH Zürich und auf den Flugplatz Birrfeld, um zu diskutieren, Beziehungen zu knüpfen und Schwerpunkte für die zukünftige Zusammenarbeit zu definieren. Sie brachten neueste wissenschaftliche Erkenntnisse ein, präsentierten technische Neuerungen und formulierten Nutzerbedürfnisse. Der Schwerpunkt der UAV-g 2011 lag auf den Forschungsaktivitäten in verschiedenen Disziplinen: Künstliche Intelligenz, Robotik, Photogrammetrie, Vermessung, Computer Vision, Luftfahrtingenieurwesen. Im Hinblick auf die Geomatik wurde gezeigt, was „State of the Art" ist und welche Herausforderungen in der Zukunft angegangen werden müssen, um UAVs noch erfolgreicher in der Geomatik einsetzen zu können. So sprach Roland Siegwart, Vizepräsident für Forschung und Wirtschaftsbeziehungen der ETH Zürich und Professor für autonome Systeme, in seinem Eröffnungsbeitrag über autonome Navigation und Positionierung, Kollisionsvermeidung und zeichnete den Trend zur Miniaturisierung von UAVs nach. UAVs können als bereits sehr hoch entwickelte Aufnahme- und Messplattformen für verschiedenste Anwendungen in Mapping und Monitoring eingesetzt werden. Allerdings ist ihr Betrieb durch gesetzliche Grundlagen, die von Land zu Land stark variieren, noch eingeschränkt.

Ein gesamter Konferenztag wurde Live-Demos auf dem Flugplatz Birrfeld gewidmet. Dort wurden unterschiedliche autonom fliegende Flugsysteme vorgestellt: Open-Source Systeme, Flächenflieger, Helikopter, Multikopter, Zeppeline und ein motorisierter Kite. Die drei besten Präsentationen erhielten den von Hexagon Technology Center/Leica Geosystems gestifteten „Most Innovative UAV Application and Demonstration Award". Das R-Pod System von senseFly, mit seiner flexiblen Einsetzbarkeit und dem geringem Gewicht für das Gesamtsystem (500 g) überzeugte die Jury. Ebenfalls sehr interessant ist der Ansatz des zweiten Preisträgers – der Schweizeri-

schen Hochschule für Landwirtschaft – welche einen Quadrokopter vom Open-Source-Projekt Mikrokopter für die Rehkitzrettung einsetzt. Der dritte Preis ging an Ascending Technology für ihr Falcon 8 System.

Weiterentwicklungen werden bei der Nachfolge-Konferenz UAV-g 2013 unter der Leitung von RALF BILL in Rostock vorgestellt werden.

Zusätzliche Informationen unter: http://www.uav-g.ethz.ch/ sowie bei HENRI EISENBEISS, ETH Zürich, Institut für Geodäsie und Photogrammetrie, Telefon +41-44-3287 633, henri.eisenbeiss@geod.baug.ethz.ch

HENRI EISENBEISS, Zürich

UAVs bei der Live-Demonstration.
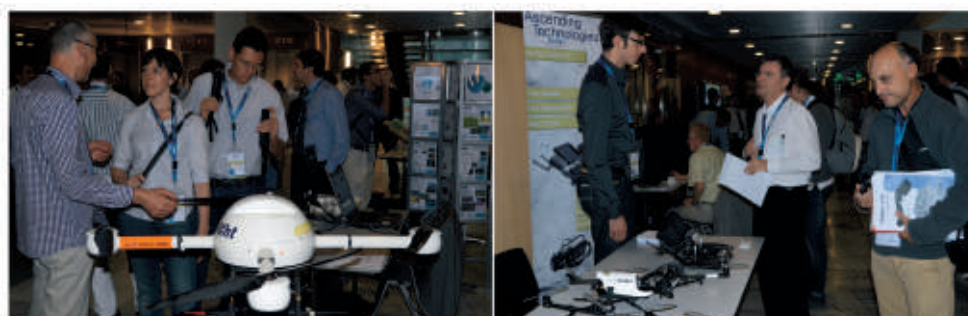
Ausstellung während der UAV-g Konferenz

11th International Scientific and Technical Conference, RACURS, Russian Federation, „From Imagery to Map: Digital Photogrammetric Technologies", September 19–22, 2011, Tossa de Mar, Spain

RACURS of Moscow, Russian Federation, is the major Russian Photogrammetric Hardware and Software Company founded in 1993. For 11 years the company organizes remarkable international scientific and technical conferences in very agreeable surroundings. The last international conferences were held 2010 in Gaeta, Italy, 2009, in Attica, Greece, 2008, in Porec, Croatia, and 2007, in Nessebar, Bulgaria. In 2011, the conference site was Tossa de Mar on the Spanish Costa Brava, north of Barcelona.

Victor Adrov, CEO and owner of the company, opened the meeting. Gisela Saldich of Tossa Municipio welcomed the participants. Cosmonaut Victor Petrovic Savinych, President of MIIGAiK chaired the first introductory session: Victor Adrov, RACURS, summarized the status of the company and that of its product PHOTOMOD: 280 companies use PHOTOMOD in Russia with 700 licenses. Worldwide there are 530 users with 1,400 licenses at 5,300 work places. Besides sponsors from industry, the following organizations supported the Conference; ISPRS, Russian GIS Association, Society of Friendship with Spain and the media GeoInformatics, GIM, GEO, Geomatica and Geotop. It is thereby remarkable that the composition of participants are to 1/3 directors, 1/3 chiefs, and 1/3 scientists.

David Sanchez-Carbonnel, Director of the Catalan Mapping Agency ICC, Barcelona reported about the progress made in photogrammetry in the Province of Catalunya: The Province with an area of 32,000 km^2 has a map scale at 1:5,000. ICC became a public company in 1997. In 2005 it also received by law the mandate for administration of the GIS under the Ministry of Territory and Sustainability. The staff of the ICC is 228. Specifications for all products made are on the ICC website. There is permanent updating. ICC operates 2 DMCs, LIDAR, CASI 2, TASI, airborne Radar and Geomobil (van). Processing is done with COTS and own application software. There are 270 TB of data online through a high performance network available. ICC has ISO certification for the production of 1:5,000 and 1:25,000 maps. Dissemination of the data is through www.icc.cat (online) or as printed paper maps. 10 % of Catalunya is covered by 1:1,000 maps updated every 5 years. The 4,274 maps 1:5,000 in 2.5D are also updated every 5 years and the 1:10,000 maps are generalized from the 1:5,000 maps. The production of orthophotos for Catalunya (32,000 km^2) at 50 cm GSD took 7 years from 1985 to 1992. In 2008 it only took 1 year. In 2009 25 cm GSD were produced for the entire area within 1 year as true orthophotos. In addition true orthophotos at 10 cm GSD were produced for some villages. The orthophotos are produced with DMC images in colour and IR. Also a thermal sensor is flown, as well as a hyperspectral CASI for thematic maps. LIDAR is used for DEM and for city models. Radar images are used for change detection. ICC also is engaged in technical cooperation projects: In Argentina 65,000 km^2 were mapped at 1:50,000 and 677,000 km^2 at 1:100,000 from satellite imagery. In Venezuela airborne radar was used for mapping 1:50,000 for 300,000 km^2 in the southern Orinoco area within a 3 months period. Subsidence was determined using radar interferometry in Catalunya, Colombia and France. Precision farming projects were carried out in Southern France and LIDAR surveys were conducted in Italy (Emilia Romagna) and Morocco. GIS base data can be accessed free of charge from WMS services at www.icc.cat. 300,000 maps are accessible.

Sergey Kadnichanskiy, chief scientist of *Meridian*, Moscow, discussed digital camera technology for large countries for mapping scales 1:5,000 to 1:25,000 (see www.agp-meridian.com). The options for aerial surveys depend on available aircraft types, scale of map to be produced, restrictions for aerial survey. For the scale 1:2,000 (18 cm GSD is usually chosen), 1:5,000 (35 cm GSD), 1:1,0000 (50 cm GSD). Urban areas need a narrow angle of view for 1:2,000 or 1:5,000 and open areas need a wide angle for 1:1,0000 or 1:25,000. Meridian operates 2 types of aircraft: King Air 350: ceiling 9,500 m, max. speed 578 km/h, min. speed 250 km/h, 5 hrs

operation time. It uses the following camera types: DMC (GSD 18 cm, h=1,800 m, 213 km²/h), ADS40 (GSD 18 cm, h=1,729 m, 207 km²/h), A3 (GSD 18 cm, 649 km²/h), comparison data for other camera types are: Ultracam 210 (GSD 18 cm, 571 km²/h), DMC II (GSD 18 cm, 399 km²/h, h=3,600 m), Ultracam 80 (GSD 18 cm, 325 km²/h, h=2,700 m). YURI RAIZMAN discussed the advantages of the Visionmap A3 camera. This panoramic type digital camera may be operated in various modes: vertical, one side oblique, and cross wise. The processing software is made for an automatic workflow. With a Learjet at 30 cm GSD, 9,000 km² may be covered per day, with a King Air at 25 cm GSD 6,250 km² and, with a Cessna at 18 cm GSD, 3,100 km². SERGEY KADNICHANSKYI discussed the acquisition of digital oblique images. Option 1: Meridian uses 2 or 4 medium format cameras mounted together with the vertical highresolution camera. Option 2: Use of Visionmap A3 camera, which covers a scan from -54.8° to +54.8° reaching a GSD from 8 cm to 12 cm. PETUCHOV of Leica Geosystems announced, that Hexagon which owns Leica Geosystems and Intergraph has acquired the company Jaggernaut with 8,000 employees. Leica Geosystems and Z/I Imaging now produce 4 sensor systems in a coordinated manner: Leica ASD80, Z/I DMC II, Leica RCD, Leica ALS. Cosmonaut and MIIGAik President VICTOR PETROVIC SAVINYCH discussed recent and future extraterrestrial space missions: Phobos – Grunt 2011 and Lyna – Glob 2015. MIIGAiK has developed Linux-based software for PHOTOMOD 5.2 to carry out mapping of small celestial bodies: selection of an object centric coordinate system, tie point creation using different lighting of craters, 3D models with overlay of textures. GOTTFRIED KONECNY spoke about remote sensing serving regional development. The scientific background of remote sensing has been developed in the 1920's and before by quantum physics. Aerial images have been used for interpretation since the 1850's. In the 1950's the American Society for Photogrammetry publishes a link between the two approaches (Colwell, "Basic Matter Relationships in Remote Sensing", Photogrammetric Engineering 1963). Landsat in 1972 became the first remote sensing satellite. The research years of remote

sensing are over by now. New and higher accuracy sensors are available now for the entire electromagnetic spectrum range. With satellite and other platforms expanding, the use of remote sensing for regional sustainable development has been initiated by the availability of integrated data systems permitting combination and analysis with data contained in relational data bases, as practiced by NASA, the US Government and the European INSPIRE effort.

In the afternoon session of the first day, ALEXANDRA KISELEVA, RACURS, presented the new capabilities of PHOTOMOD 5.2 such like special aerial triangulation for unmanned aerial vehicles (UAV), new adjustment algorithms, direct working with jpeg-images, without need for conversion. UAV processing consists of: Import of (inaccurate) exterior orientation data from navigation devices, correction by flight direction data, automatic block assembly and triangulation. An example with 700 images of a non-metric camera has been presented. Projection centers were known to +/-12 m. 8 GCP's were used with accuracies of +/-2 m. On-the-fly orthorectification is possible on the basis of SRTM-DSM data. Stereo vectorization of source images is also possible as well as the transfer of textures in 3D Mod from oblique images. ANTON VASSILJEV talked about the use of the NVIDIA graphics processor in his research project for oblique images correlation, bundle adjustment, and stitching of images, showing the advantages of GPU fast parallel processing. VANYA PETROVA, Sofia-GIS, discussed "Updating of Bulgarian Large Scale Topo Map". Systematic mapping of Bulgaria began with the map 1:25,000 in 1942, and at scales 1:5,000 and 1:10,000 in 1955. Since then digital photogrammetry using PHOTOMOD has been introduced. For Sophia (1,467 km²) an orthomap has been created at 10 cm GSD, and a DTM was established with 5 m contour output in 2008. DMITRY KOCHERGIN, RACURS, demonstrated a Geomosaic 5.2 PHOTOMOD project to generate a seamless mosaic for 1,000 images with automatic seamline generation and distributed processing. Seamlines may be edited. Tie points are generated automatically. Colour balancing is performed. SERGEY SKUBIEV, University of Land Use Planning, Moscow, is en-

gaged in UAV activities. Launches of different UAV's are possible by hand up to catapult operations with the UAVs landing on air strips or by parachute. Strategic UAVs can stay in the air for 24 to 72 hours and reach 15 to 20 km in height. At lower altitudes helicopter UAVs can be used to get data over 15 to 20 km^2 villages. As cameras the Canon 5D I D or Canon 20, 30 are used. Operation from ground stations is quite simple. ARMIN GRUEN gave a talk about UAVs and their applications. He was involved in 50 UAV projects since 2004. At present there is an integration of novel sensors with a trend towards real time applications. One does not look for high precision, but for robustness, open source, camera calibration, accuracy testing, 3D modelling and for obtaining flight permissions. There are various types of UAVs available. Preferred are autopilot and autonomous flights. He showed various project examples such as Ayers Rock in Australia, Xochicalco in Mexico, football stadium in Dortmund, Germany, "real time" flood control in Korea, archaeology in China, thermography in Shanghai and many cultural heritage applications, e.g. Pinchango Alto in Peru. The Zurich software SAT-PP is used for image matching as demonstrated in numerous projects. Regarding automation capabilities the human interpreter is good in image recognition and interpretation but the computer performs the measurement first as its accuracy is hard to match. ANDREY SECHIN, RACURS, reported on UAV Processing Capabilities with PHOTOMOD. These were demonstrated for the Kretchet Project, conducted by MIIGAiK. A Samsung amateur camera was used from 300 m to 2,500 m height at speeds of 70 to 100 km/h. Problems arose due to missing calibration of the camera, focal plane shutter, small stereo base, inaccurate exterior orientation. With no calibration the accuracy was around 30 m, with self-calibration using overlapping photos 1 m accuracy was achieved. It is recommended to use calibrated cameras with fixed zoom lenses and exposures <1/250 sec and use of professional GPS receivers. ALEXEY BELENOV, SOVZOND, used UAV photography for monitoring of pipelines, forest fires, gas and oil exploration. The major problem for use of UAV's was weather and wind. MIKHAILOV compared the use of metric and non-metric cameras on UAV's. VANYA PETROVA delivered IVAN KATZARSKY's paper on the history of Bulgarian photogrammetry.

The next day started with a report of SERGEY DUDKIN, SOVZOND: They monitor the Earth using a variety of available remote sensing satellites. It uses degraded images, but utilizes high performance processing with multisensory access. ANDREY SHUMAKOV, GeoEye: GeoEye provides satellite data and services for Ikonos, GeoEye1, and in the future for GeoEye2 and 3. Instant image delivery is possible via Internet. For this the EyeQ platform can be used. This software is available also as an option for exclusive customer use. It provides a Web Map Server (WMS), KLM, Web Map Tiling Service (WMTS), Web Coverage Service (WCS) and Web Feature Service (WFS). FELIX PULS reported that European Space Imaging (Munich) hosts a Direct Access Facility for WW1 and WW2 with stations at Oberpfaffenhofen and Abu Dhabi for satellite download of Quickbird-, WW1 and WW2 images (and in the future WW3, 2014). The constellation capacity is for Moscow daily, for Baghdad, because of the closer distance to the equator 2 to 3 days. Weather prediction by RT weather yields a success of cloud free images of 80 % and 30 % if no weather forecast is used. OLEG SOLONTSOV, Roslesinforg, represents forest mapping in the Russian Federation. Roslesinforg is an organization of 3,300 persons managing federal contracts, the forest cadastre, R&D and the international forestry contacts. The Russian Federation covers 25 % of the world´s forest reserves. 1970 aerial photos exist for the managed forest area of 1M km^2. The updating is done from high resolution satellite images with GSD 2.5 m (Spot5, ALOS), 5 m (RapidEye) and 0.5 m (WW1, WW2 and Quickbird). ANDREY SUDRGIN reported about software developed for different image formats and visualization. It includes interactive geometric radar-optical correction. ANDRANIK KHACHATRYAN from Nagorno-Karabakh reported on their update of topographic maps 1:10,000 from spaceborne data for 1:10,000 digitized maps using PCI software. JIHOON KANG, Korean Aerospace Research Institute, talked about accelerated satellite image processing using GPU. GOTTFRIED KONECNY presented the challenges offered by impor-

tant industry developments presented to geo-informatics such as, GPS positioning to +/-1 cm accuracy, digital imagery, high resolution satellites, laser scanning, exponential computer development progress, data bases, GIS and mobile technology. Armin Gruen discussed 3D mapping from space. Since the launch of the first remote sensing satellite in 1972 there has been an increase of resolution by the factor 150. We now have stereo capability and georeferencing. Accuracy in planimetry is to 1 pixel and in height to 1 to 5 pixel. The problems still existing are: lacking availability, high costs, low image quality and lack of good commercial software. Subpixel accuracy is a solved issue as well as automation, but automatic object extraction is not possible. 3D mapping is not fully understood, while 2D or 2.5D mapping has been used in practice. The *CyberCity Modeller* software was applied already 10 years ago for Hamburg and for Salzburg. The application is a matter of project pricing. There are two issues to be solved: 1) metric, this is easy to be solved; 2) semantic: there are a number of open questions; for instance, how does Google Earth or Bing Maps change the perception of a map? Should the data collection be offline or online? Should the object extraction be manual, semi-automatic or fully automatic? Should the modelling be 2D, 2.5D or 3D? In addition there are open questions concerning the map features: The Swiss map 1:25,000 and 1:50,000 has 105 types of objects. These are not all identifiable from satellite images (e.g. radio transmitters, road classes). The problem is that there is 1.5 to 3 years of time difference between photo flight and delivery of the map to the public. A topographic landscape model TLM should be created as base for the whole country. A TLM should have no generalization. It should be continuously updated with an accuracy of 1 m. Also the user requirements may change. Concerning satellite images problems exist regarding image quality, clouds, sometimes limited gray levels (ALOS PRISM only has 8 bit) and artifacts of CCD/CMOS sensor arrays. When aerial imagery is resampled to the ALOS 2.5 m GSD, ALOS images have less quality. The same is true for a comparison between 60 cm GSD QuickBird images and reasampled aerial imagery at 50 cm GSD, as

tested in the UK. Object extraction showed a completeness of industrial objects at 70 % and of residential objects at 65 %, which was mainly caused due to shadows and poor image quality. He concluded that image quality is an important issue, 3D city modelling is possible, but only in a semi-automated procedure. Satellites can be used, if the standards of conventional mapping are reduced. In Switzerland the opposite trends are noticed: standards go up. Discussion should be about models of the landscape, not maps. Mikhail Drakin reported about high performance cluster computing with PHOTOMOD HPC edition: Parallel processing is possible, if tasks are similar, if the source is independent from the tasks, and if the tasks are independent from the output. Parallel processing was done in the cases of tie point measurement, DTM calculations, ortho-rectification and mosaic formation. The cluster has been run by increasing the number of cores in off the shelf CPUs, by larger local networks, by using supercomputers as clusters of similar nodes. With PHOTOMOD HPC Edition a block covering 1,200 km^2 at 16 cm GSD has been processed in 3 hours. Victor Lebasov, finally, gave a talk about remote sensing for flight security and the special challenges due to more airplanes and the need for controlling takeoffs and landings. An airfield needs to be modelled in a diameter of 45 km, while natural or artificial barriers need to be modelled in 3 zones with a DTM grid width of 30 m in zone 1, of 3 m in zone 2, and of 0.3 m in zone 3. In particular for the Olympic sites at Sochi, a contract has been let to MIIGAiK to model the Sochi airfield to increase air traffic.

The afternoon session of day 2 started with a talk of Ekaterina Mukusheva about dynamic geometric models for optoelectronic space systems. Elena Kravtsova reported on satellite Kanopus-V image processing via PHOTO-MOD. Leonid Bykov presented the result of WorldView II orthomosaic creation for 214 settlements, covering 164 km^2. Yana Razumova mapped 147 licensed areas for natural gas production in Siberia covering a total area of 21,000 km^2 using GeoEye1 images at the scale 1:25,000. Alexey Peshkun investigated the use of many overlapping Resurs-DK1 images taken during the last 5 years to prove the feasibility to generate DTMs with 3 to 4 m ac-

curacy. OLGA GERSHENZON, ScanEx, presented projects of the company. Created in 1989, it is a satellite image provider cooperating with international non-classified satellite operators in America, Europe and Asia to obtain timely images for clients in Russia, such as the Forest Agency. She showed applications for flooding (Tomsk, Krasnojarsk), oil pollution (Turkmenistan), fire fighting (Siberia). KIRICHENKO, Panorama, reported on the creation of the Tver Geoportal for urban map distribution.VICTOR ADROV showed the development of a corporate management geoportal for the data archives, the contractors and the projects of RACURS. EUGENE IVASHCHENKO discussed the possibility of building SAR systems in the VHF band for depth penetration down to 10 m. YURI BARANOY, Gazprom, reported on the company's radar satellite InSAR efforts to detect surface movements in oil and gas fields in Siberia. Control markers are difficult to establish in permafrost areas. PAVEL NEYMAN talked about the difficulties in the visual interpretation of radar images. The first approach must always be visual, with the computer for further detailed processing. Optical images may help to geometrically reference radar images. For that purpose Terraview software has been developed (www.terraview.ru).

The third day was dedicated to a PHOTO-MOD Master Class including demonstrations of DMITRI KOCHERIN, who showed detailed demonstrations on Geomosaics, Digital Terrain Models from aerial images and satellite images, UAV applications for mosaicking and aerial triangulation and the use of 3D Mod. At the last day an excursion to the City of Barcelona has been organized including visits of Sagrada Familia, the Gothic Quarter and the Gaudi Park.

Abstracts of the papers and all power point presentations may be downloaded from the web (http://www.racurs.ru/Spain2011/en). On that website select "Review" and then "Presentations" to download each of the 42 presentations as ppts.

GOTTFRIED KONECNY, Hannover

ISPRS Konferenz „PIA11 – Photogrammetric Image Analysis", 5.–7. Oktober 2011, München

Die gemeinsame Konferenz der ISPRS-Arbeitsgruppen I/2, III/1, III/4 und III/5 fand vom 5.–7. Oktober 2011 an der Technischen Universität München (TUM) statt. Die lokale Organisation wurde vom Lehrstuhl für Photogrammetrie und Fernerkundung unter der Leitung von UWE STILLA, Vorsitzender der ISPRS Arbeitsgruppe WG III/5, durchgeführt.

Entsprechend der beteiligten Arbeitsgruppen wurden die Themen *„LIDAR, SAR and Optical Sensors"* (WG I/2), *„Pose Estimation and Surface Reconstruction"* (WG III/1), *„Complex Scene Analysis and 3D Reconstruction"* (WG III/4) und *„Image Sequence Analysis"* (WG III/5) angesprochen. Der Schwerpunkt der Veranstaltung lag auf der Methodik zur automatischen Extraktion von topographischen Objekten aus verschiedenen Datenquellen. Gerade durch die Verbindung der Arbeitsgruppen aus den Kommissionen I und III wurden sowohl Themen im Zusammenhang mit Sensoren als auch die automatische Auswertung diskutiert. Die PIA11 fokussierte nicht nur auf Wissenschaftler aus universitären Einrichtungen und Forschungsinstituten, sondern auch auf Teilnehmer aus Industrie, staatlichen Organisationen und privaten Unternehmen und bot eine ideale Plattform zur Diskussion neuester Entwicklungen und zukünftiger Trends.

Im *„Call for Papers"* der PIA11 riefen die Konferenzveranstalter UWE STILLA (Technische Universität München), FRANZ ROTTENSTEINER (Leibniz Universität Hannover), HELMUT MAYER (Universität der Bundeswehr München), BORIS JUTZI (Karlsruher Institut für Technologie) und MATTHIAS BUTENUTH (Technische Universität München) auf, Beiträge als *„Full Paper"* einzureichen. Daraufhin wurden insgesamt 54 Manuskripte von Autoren aus 18 Ländern eingereicht, die einem *„Double Blind"* Review-Prozess unterzogen wurden. Jeder einzelne Beitrag wurde im Mittel von drei der 29 Gutachter aus dem Programmkomitee bewertet. Insgesamt wurden 30 Beiträge angenommen, woraus eine Annahmequote von 56 % resultiert. Davon wurden 25 Beiträ-

ge in der renommierten Serie *„Lecture Notes in Computer Science (LNCS)"* des Springer Verlags in gedruckter Form veröffentlicht und fünf Beiträge in den *„International Archives of the Photogrammetry, Remote Sensing and Spatial Information Science (IAPRS)"* auf CD. Alle Beiträge sind im Tagungsband der IASPRS (Volume 38, Part 3/W22) im Teil 1 aufgeführt. Weiterhin wurden Autoren mit eher anwendungsorientierten Themen, die sich besonders für eine interaktive Präsentation eignen, eingeladen, erweiterte Kurzfassungen ihrer Arbeit einzureichen. Auch die nicht im *„Full Paper Review"* angenommen Beiträge wurden für die Auswahl der interaktiven Präsentationen erneut berücksichtigt. Teil 2 des Tagungsbandes enthält 23 von diesen Beiträgen. Insgesamt wurden 55 Präsentationen von 74 Einreichungen (74 %) akzeptiert. Erwähnenswert bei dem Reviewprozess der PIA11 war die Transparenz des Auswahlverfahrens, bei dem die Reviewer nachher in anonymisierter Weise Einblick erhielten, wie ihre Kommentare und Bewertungen in Relation zu andern Begutachtungen ausfielen.

Das Buch mit den gedruckten Beiträgen und der Tagungsband auf der CD waren bereits zu Beginn der Veranstaltung für die Tagungsteilnehmer verfügbar. Der Tagungsband ist sowohl im ISPRS Archiv (www.isprs.org) als auch unter http://www.pf.bv.tum.de/isprs/ pia11/pia11_pro.html verfügbar. Das Programm unterteilte sich in die sieben Sitzungen *Orientation*, *Matching*, *Object Detection*, *3D Reconstruction and DEM*, *Classification*, *People and Tracking* und *Image Processing and Visualization* mit insgesamt 28 Vorträgen und eine Postersitzungen mit 27 Beiträgen.

PIA11 wurde von 130 Teilnehmern besucht. In der Tradition der vergangenen Veranstaltungen wurde von den Organisatoren bewusst auf parallele Vortragsveranstaltungen verzichtet und jedem Vortrag genügend Zeit zur Präsentation und Diskussion eingeräumt. Erfreulich war, dass sich die Zuhörer aktiv an der Veranstaltung beteiligten und alle Beiträge intensiv diskutiert wurden. Dies wurde auch durch die günstige Architektur des Auditoriums unterstützt, die Zuhörer und Vortragende nahe zusammenbrachte. Neben den ausgewählten Vorträgen wurden zwei eingeladene Vorträge präsentiert, die das Auditorium begeisterten: Daniel Cremers (TU München) stellte konvexe Optimierungsmethoden für die Computer Vision vor und Horst Bischof (TU Graz) zeigte Möglichkeiten zur vollautomatischen Generierung von Stadtmodellen. Ein besonderes Highlight war die Postersession in den modernen Räumlichkeiten auf dem Dach der Technischen Universität mit einem ausgezeichneten Ausblick über die Stadt. Die Postersession ging später gleitend in die *Ice Breaker* Party mit einem feinen Büffet über und erlaubte auch noch hier weitere intensive Diskussionen an den Postern. Am zweiten Abend wurde zu einer zünftigen Abendveranstaltung im weltbekannten Münchener Hofbräuhaus geladen.

Uwe Stilla bei der Begrüßung der Teilnehmer

Ice Breaker Party

Abendveranstaltung im Münchener Hofbräuhaus

In der Schlussveranstaltung der PIA11 wurden der beste Beitrag aus dem Vortragsprogramm und der beste Posterbeitrag mit einem Geldpreis ausgezeichnet. Die Gewinner für

Preisverleihung für Falko Schindler und Philipp Meixner mit dem Chair und den Co-Chairs der PIA11 (v.l.n.r: Matthias Butenuth, Helmut Mayer, Falko Schindler, Franz Rottensteiner, Philipp Meixner, Boris Jutzi, Uwe Stilla).

den besten Vortrag waren Falko Schindler mit dem Beitrag *Fast Marching for Robust Surface Segmentation* und Philipp Meixner mit dem Poster *Interpretation of 2D and 3D Building Details on Facades and Roofs*.

Die Konferenz wurde durch das Team um Uwe Stilla mit Florian Burkert, Konrad Eder, Christine Elmauer, Ludwig Hoegner, Dorota Iwaszczuk, Michael Schmitt, Sebastian Tuttas und weiteren Helfern exzellent organisiert. Dies erstreckte sich von den Vorbereitungen für die Konferenz, die termingerechte Einhaltung der Benachrichtigungen, Erstellung des Tagungsbandes, über die Durchführung des technischen Programms bis hin zur ausgezeichneten Bewirtung der Teilnehmer. Die gezeigten Präsentationen waren allesamt auf sehr hohem Niveau. Die Diskussionen mit den internationalen Teilnehmern erlaubten einen interessanten Austausch und das Knüpfen von Verbindungen. Zum Ausklang der PIA gab es auch diesmal wieder nach bayrischer Tradition Bier vom Fass, Brezeln und Weißwurst. Nach den erfolgreichen Veranstaltungen 1999, 2003, 2007 und 2011 sieht man gespannt und erwartungsvoll der nächsten Münchner Veranstaltung dieser Art entgegen. Ausgewählte Themen der PIA11 werden im Rahmen eines Schwerpunktheftes der PFG im Jahr 2012 wieder aufgegriffen werden.

Boris Jutzi, Karlsruhe / Ettlingen

ISPRS Workshop „Geospatial Data Infrastructure: from Data Acquisition and Updating to Smarter Services", October 20–21, 2011, Guilin, province Guangxi, China

The goal of the workshop was to provide an exchange platform for research ideas, interests and collaboration in the context of geospatial data infrastructures. Important topics like data analysis, harmonizing and updating but also general infrastructure issues were addressed in the objectives of the workshop invitation. The conference was jointly organized by the ISPRS Working Groups *Geospatial Data Infrastructure* (WG IV/1), *Automatic Geospatial Data Acquisition & Image-Based*

Li River near Guilin, province Guangxi, in south China.

Databases (WG IV/2), *Virtual Globes and Context-Aware Visualization* (WG IV/4), *Distributed and Web-Based Geoinformation Services and Applications* (WG IV/5), *Planetary Mapping and Databases* (WG IV/7), *Updating and Maintenance of Core Spatial Databases* (ICWG IV/VIII) and hosted by the National Geomatics Center of China.

Around 90 participants have been attracted for two days of collaboration and discussion. After a warm welcome in the opening ceremony, the three keynote speakers LI DEREN (Wuhan University, China), RAJ SINGH (Open Geospatial Consortium, United States) and ANDREAS ILLERT (Federal Agency for Cartography and Geodesy, Germany) started to highlight many objectives of the conference. Global web services paired with open interface standards (OGC) have reached implementers and users in a mature status. Building up a geospatial infrastructure for many nations and big organizations has been successfully established, but achieving operational robustness and quality of the implemented service will be the real challenge in the future.

Organized in a single track on the first day, the workshop has been divided in two plenary sessions: *Mapping and Updating* as well as *Service and Application*. These topics revealed several core aspects for geospatial data infrastructures, starting from data acquisition and updating until the final delivery process by sharing data with users in the Internet. The vast amount of different data and processing requirements (e.g. for China) did indicate, what enormous conceptual effort in detail is necessary to maintain a consistent updating mechanism.

During the next day two parallel sessions were covering in detail the following aspects: *Data Updating, Planetary Mapping and Da-* *tabases* (two sessions), *Web-based Services* (two sessions), *Data Acquiring and Processing, Change Detection and Monitoring* and *Applications*.

Several speakers showed in detail fairly different approaches for data updating, which is typically related to very specific setups of national infrastructure. It was obvious that the concept of national geospatial infrastructure cannot simply follow a top-down command approach. Different cultural behaviour and habits on the regional level have to be integrated in a national structure, so that all participants are working in the same direction.

The sessions with planetary mapping and databases showed several unusual aspects of processing issues. For Earth bound imagery detailed knowledge about the spectral characteristic of soil types and the atmosphere results in operational aerotriangulation of large image databases. For planetary mapping tasks different assumptions and intelligent estimations have to replace missing ground truth data.

Web-based services were also present in several talks and show that they represent nowadays a kind of de-facto standard access interface for many services, therefore ontology based approaches and metadata services play a more and more important role.

The workshop was very well organized by JIANG JIE (Chair, ISPRS WG IV/1), WANG QIAN and many other collaborators from the National Geomatics Center of China. The two social events allowed for many informal discussions and the exciting environment of the Guilin ("forest of sweet Osmanthus") motivated several participants to attend different tours in the vicinity of amazing Li River.

RUEDI BOESCH, Birmersdorf, Schweiz

Buchbesprechung

Andre Iost, Katja Oehmichen **und Thomas Riedel: Evaluierung satellitengestützter Stichprobenkonzepte für die Bundeswaldinventur.**
Serie Geowissenschaften, Forstwirtschaft, RHOMBOS Verlag Berlin, 2010

Der Titel des Buches hat meine Neugierde geweckt. Er verspricht neue Erkenntnisse darüber, wie Satelliteninformation Stichprobenkonzepte für Großraum-Inventuren wie die Bundeswaldinventur (BWI) unterstützen könnte. Nach Durchsicht kann ich feststellen, dass sich das Buch vor allem mit der Frage befasst, ob eine Vorstratifizierung über Fernerkundungsdaten Genauigkeits- und letztendlich auch Kostenvorteile gegenüber einer rein terrestrischen Inventur bringen kann. Es geht somit um eine Studie zur Effizienzbeurteilung ausgewählter Verfahren bei konkreter Aufgabenstellung.

Das Buch ist in 8 Hauptkapitel untergliedert. Die Einleitung gibt einen kurzen Einblick in die Notwendigkeiten einer nationalen Forstinventur (Kapitel 1). Anhand der Kosten nationaler Inventuren mit konventioneller Methodik wird dargelegt, wieso alternative Inventurverfahren von Interesse sein könnten. In vielen europäischen Ländern spielt die Methode Fernerkundung hierbei eine entscheidende Rolle. Es ist daher naheliegend, diese Methode unter den speziellen Rahmenbedingungen in Deutschland zu untersuchen. In Kapitel 2 werden die Inventurverfahren der BWI (2.1), die eingebundenen Fernerkundungssysteme (2.2), die Testgebiete und Datengrundlagen der Studie (2.3, 2.4), sowie die Aufbereitung der Satellitendaten (2.5) vorgestellt. Kapitel 3 gibt dann einen sehr detaillierten Überblick über Inventurkonzepte im Allgemeinen und für forstliche Großrauminventuren im Speziellen. Es wird sowohl auf die Techniken der Stichprobenauswahl (3.1) als auch auf Inventurverfahren (3.3), Schätzverfahren bei Großrauminventuren und Stichprobenverfahren bei Folgeinventuren

(3.4, 3.5) eingegangen. Kapitel 4 wendet sich der Fernerkundung zu, genauer, der Erstellung von Waldmasken aus Fernerkundungsdaten. Dieser auf den ersten Blick triviale Vorgang erweist sich bei genauerem Hinsehen als hoch komplexes Kern-Problem (4.1). In den Unterkapiteln 4.2-4.5 werden die eingesetzten Techniken der Informationsableitung aus den Fernerkundungsdaten dargestellt. Unter 4.6 wird eine Einführung in Verfahren der Genauigkeitsanalyse bis hin zur Bewertung und Validierung der Ergebnisse gegeben. Kapitel 5 befasst sich mit der Erfassung waldspezifischer Parameter über Landsat und QuickBird Daten. Eingangs wird die zu Grunde liegende Grauwertanalyse erläutert (5.1). Danach wird die Eignung der Fernerkundungsdaten für Regressionsschätzverfahren (5.2) und hernach die Eignung der Klassifikationsergebnisse für stratifizierte Schätzverfahren untersucht (5.3). Abschließend wird das Potential zur Senkung des Stichprobenfehlers durch Stratifizierung über FE-Daten analysiert (5.4, 5.5). Kapitel 6 wendet sich dem Kostenaspekt zu. Ausgehend von der Kostenfunktion (6.1) werden Kosten-Zeitdaten der Fernerkundungsphase und anschließend der terrestrischen Aufnahmen untersucht (6.2, 6.3). Kapitel 7 befasst sich mit Fragen der Optimierung des Verfahrens. Es werden die Methode der antizipierten Varianz (7.1) und die Quotientenmethode (7.2) vorgestellt, auf die Daten angewandt und verglichen (7.3). Abschließend werden die Kosten tabellarisch gegenübergestellt. Die Diskussion (Kapitel 8) befasst sich mit den Themen Walddefinition (8.1), Verifizierungsverfahren (8.2), Schwellenwertverfahren (8.3), Logistischer Regressionsansatz anhand der Merkmale Waldstatus und Mischung (8.4) und dem k-NN Verfahren mit den Merkmalen Waldstatus und Alter (8.5). Abschließend wird ein Fazit zum Thema der Waldflächenermittlung mit Satellitendaten gezogen (8.6) und Empfehlungen zu alternativen Stichprobenverfahren aus den Untersuchungen abgeleitet (8.7). Ein umfangreiches Literaturverzeichnis und ein Anhang mit weiteren Ergebnissen der Optimierung schließen das Buch ab.

In Summe lässt sich festhalten, dass das Buch ausgeprägte Stärken aber auch einiges an Optimierungspotenzial besitzt. Den Fernerkundungsteil betreffend haben sich die Erwartungen nicht in vollem Umfang erfüllt. Die Einsetzbarkeit der Sensorik wird im Rückblick bewertet. Die zu Beginn der Studie als am ehesten ‚operationell‘ einzustufenden Systeme Landsat TM und ETM+ wurden als Stand der Technik angenommen und dienen als Basis für die Einschätzung des Nutzens von satellitengestützer Information für die BWI. Als Referenz wird QuickBird herangezogen. Es ist dabei fraglich, ob 16km Streifenbreite wirklich geeignet ist, um flächendeckend Informationen zu liefern. Auch hätten neue Systeme, wie etwa RapidEye, in Zukunft auch Sentinel 3 und 4, in Kombination mit den heute flächig verfügbaren digitalen Orthobildern auf Basis digitaler Kamerasysteme in die Betrachtung einbezogen werden können. Bezüglich der verwendeten Auswertemethodik wird ausschließlich auf ‚klassische‘ pixelbasierte Datenanalysetechniken eingegangen. Eine Erweiterung hinsichtlich segment-, objekt- und kontextorientierter Verfahren, die schon seit einigen Jahren sehr erfolgreich auf Daten unterschiedlicher Skalenbereiche angewendet werden, findet zwar Erwähnung, wird aber leider nicht näher betrachtet. Die eingangs erwähnten Alternativen zum bestehenden BWI-Inventurverfahren werden daher nur in Grundzügen skizziert aber nicht voll ausgeschöpft. Die erzielte hervorragende Genauigkeit der Bestimmung der Parameter Holzbodenfläche, bzw. Waldmaske oder ‚Waldstatus‘ lassen sich u.a. darauf zurückführen, dass multitemporale Signaturen für diese Parameter als weniger ausgeprägt betrachtet werden können. Für andere Parameter wäre eine detailliertere Diskussion der Aufnahmezeitpunkte, Atmosphären- und Reliefeinflüssen wünschenswert gewesen, da zwar – gegen solche Einflüsse theoretisch invariante – Indizes Erwähnung finden, aber offenbar nicht weiter in die Analyse einfließen. Die gezeigten Ergebnisse zur Unterscheidung von Mischwald basierend auf Landsat Daten sind moderat und decken sich damit mit den Erfahrungen anderer Arbeiten. Erstaunlich ist dagegen die hohe Erfolgsquote bei der Differenzierung von Nadel- und Laubwald. Insgesamt hat sich bei mir der Eindruck gefestigt, dass Fernerkundung als Methode zwar eingesetzt und untersucht, den Daten aber nicht das Optimum an Aufmerksamkeit gewidmet wurde.

Interessant und äußerst lehrreich sind die grundsätzlichen Probleme dargestellt und diskutiert. So erschließt sich etwa schnell die Problematik und auch die Komplikationen die sich im Falle der BWI durch die Notwendigkeit ergeben, robuste Verfahren für die gesamte Bundesrepublik zu entwickeln und zu bewerten. Es wird sehr deutlich, dass die Datenqualität (Fernerkundungsdaten, Zusatzdaten, Erhebungsdaten, etc.) nicht einheitlich ist, dieses aber auch nicht erwartet werden kann. Man versteht, dass die vorgestellten Lösungsansätze dem Diktat der Robustheit unterworfen sind. Es sind aber auch Detailfragen, die immer wieder an grundsätzliche Grenzen stoßen, die angesprochen werden. Etwa die Diskussion um die Bestimmung der Holzbodenfläche, bzw. der Waldmaske, die deutlich macht, dass es keine „offizielle“ und bundesweit verfügbare Datengrundlage gibt, anhand derer der Erfolg von Klassifikationen über Fernerkundungsdaten überprüft werden könnte (Kap. 4.3.2.3).

Trotz der obigen, teilweise wohl subjektiven Einschätzungen, die positiv gesehen auch als Denkanstöße verstanden werden können, möchte ich das Buch jedenfalls vorbehaltlos empfehlen – als Quelle für Verfahren der Großrauminventur, für klassische Auswertungsmethodik von Fernerkundungsdaten aber auch für statistische Verfahren der Stichprobeninventuren. Auch wenn der Stil für einen Fernerkundler, Statistiker oder auch Waldinventur-Spezialisten teilweise belehrend wirkt, die Detailtiefe und die präzisen Erläuterungen der Verfahren lassen auch den Nichtfachmann/frau verstehen, was gemeint ist und wie es umzusetzen wäre. Der Wissensschwerpunkt der Autoren liegt offensichtlich in der Statistik. Die theoretische Herleitung sowie die statistische Analyse sind hervorragend dargestellt und sachlich gut begründet: Lehrbuchqualität bei exzellentem, praxisorientiertem Problemfall! Für Studierende etwa der Forstwirtschaft kann sich das Buch zu einem Standardwerk für Großrauminventuren entwickeln.

Thomas Schneider, München – Weihenstephan

<div style="border:1px solid">

Persönliches

</div>

Rudolf Förstner zum Gedächtnis

99 Lebensjahre alt verstarb am 3. November 2011 in Kernen im Remstal Prof. Dr.-Ing. habil. RUDOLF FÖRSTNER, Direktor a.D. des damaligen Instituts für Angewandte Geodäsie (des heutigen Bundesamts für Kartographie und Geodäsie) in Frankfurt am Main. In seinem letzten ‚Jahresbericht' 2010 für die Großfamilie und Freunde hatte er diesmal als Leitmotiv gewählt „Die Stunde drängt, und rascher Tat bedarf's". Zu einem Jahresbericht 2011 kam es nun nicht mehr.

Hinsichtlich seiner Berufswahl folgte RUDOLF FÖRSTNER einer wohl etwa 100jährigen Familientradition: er wurde Geometer, später aber Photogrammeter. Am 15. Oktober 1912 in Geislingen an der Steige geboren (als Sohn des dortigen Oberamtsgeometers), studierte er 1931–1935 an der TH Stuttgart Geodäsie mit Abschluss und beendete 1938 seine Referendarzeit als Assessor des Vermessungsdienstes.

Seine berufliche Laufbahn begann er jedoch nicht in Württemberg, sondern in Berlin, am 1. November 1938 bei der Firma Hansa Luftbild GmbH, damals erdweit die größte Luftbildfirma. Der Geometer ist nun auf dem Weg zum Photogrammeter. Im Rahmen eines Versuchs zum Einsatz der Photogrammetrie in der Flurbereinigung (1940, luftphotogrammetrische Versuchsmessung ‚Helmstadt' westlich Würzburg), führte er die Messungen und Berechnungen zur Erstellung des erforderlichen Passpunkt- und Kontroll-Punktnetzes durch. Mit der daraus resultierenden Dissertation „Passpunktbestimmung, ein Beitrag zur indirekten Streckenmessung" wurde er 1943 an der TH Berlin zum Dr.-Ing. promoviert. Als Soldat in der militärischen Einrichtung „Sonderluftbildabteilung" (die Hansa Luftbild GmbH war inzwischen zu dieser umfunktioniert worden) erlebte RUDOLF FÖRSTNER das Ende des II. Weltkrieges. Nach Entlassung aus der Kriegsgefangenschaft kehrte er in seine württembergische Heimat zurück und arbeitete rund sieben Jahre beim Feldbereinigungsamt in Besigheim. Während dieser Zeit

habilitierte er sich 1947 an der TH Stuttgart mit der Habilitationsschrift „Die Richtungsfehler geneigter Luftaufnahmen bei der Radialtriangulation". Nach längerer Lehrtätigkeit an der TH ernannte ihn diese 1957 zum apl. Professor.

Bereits ab 1. August 1953 war RUDOLF FÖRSTNER hauptberuflich in das Institut für Angewandte Geodäsie (IFAG) in Frankfurt am Main eingetreten, einer Bundesbehörde im Geschäftsbereich des Bundesministers des Innern und Abteilung II des Deutschen Geodätischen Forschungsinstituts bei der Bayerischen Akademie der Wissenschaften. Dort war ihm die Leitung des Fachbereichs Photogrammetrie übertragen worden, der 1958 den Status einer Abteilung erhielt (neben den Abteilungen Geodäsie und Kartographie). Nach langjähriger Leitung der Abteilung Photogrammetrie, die in der Außenstelle des IFAG, in der Villa v. Meister (eines Gründers der Farbwerke Höchst) in Frankfurt-Sindlingen ansässig war, erfolgte am 1. Februar 1975 die Ernennung zum Direktor des Instituts für Angewandte Geodäsie. Damit verbunden war für RUDOLF FÖRSTNER ein Ortswechsel von der Au-

ßenstelle in die Zentrale des IFAG, der Villa Mumm in der Richard-Strauss-Allee in Frankfurt am Main. Die fachlichen Arbeiten der Abteilung Photogrammetrie beziehungsweise des (gesamten) Instituts für Angewandte Geodäsie sind in den veröffentlichten Jahresberichten dokumentiert. Persönliche Widmungen für RUDOLF FÖRSTNER zu seinen Geburtstagen 60, 65, 70, 75 und 90 erschienen in verschiedenen Fachzeitschriften, auch in dieser.

Herausragende Aktivitäten entfaltete RUDOLF FÖRSTNER während seiner aktiven Zeit vor allem in der OEEPE (Organisation Européenne d'Etudes Photogrammétriques Expérimentales), dem heutigen EuroSDR (European Spatial Data Research), wo er seit Gründung der Organisation (1953) tätig war, ab 1959 vor allem als Präsident der Kommission C (Großmaßstäbige Karten und Katastervermessung) und ab 1975 im Direktionskomitee als offizieller Vertreter die Bundesrepublik Deutschland. In nationalen fachlichen Einrichtungen waren es vor allem die Deutsche Geodätische Kommission (DGK) und die Arbeitsgemeinschaft der Vermessungsverwaltungen der Länder der Bundesrepublik Deutschland (AdV), wo er sich einbrachte. Am 31. Oktober 1977 trat er in den Ruhestand. Für seine Verdienste um die Bundesrepublik Deutschland verlieh ihm der Bundespräsident das Bundesverdienstkreuz. Anlässlich seines Goldenen Doktor-Jubiläums 1993 ehrte ihn die Technische Universität Berlin mit einem Festkolloquium.

RUDOLF FÖRSTNER hat als Mitglied in verschiedenen Fachverbänden mitgewirkt. Beispielsweise war er von 1948–1953 Vorsitzender des DVW Landesvereins in Württemberg. An der Universität Frankfurt am Main hat er viele Jahre einen Lehrauftrag wahrgenommen. Unter seiner Leitung wurden im IFAG ferner eine Reihe von Fortbildungsveranstaltungen für Photogrammeter in der Praxis durchgeführt, beispielsweise im Zusammenhang mit der Einführung der Orthoprojektion und der Bildkorrelation. Die Abteilung Photogrammetrie war unter seiner Leitung auch an verschiedenen deutschen Entwicklungsprojekten in Afrika und in Südamerika beteiligt.

Ergänzend zum beruflichen Lebensweg des RUDOLF FÖRSTNER seien hier noch zwei Anmerkungen gestattet. Seine große Liebe zur Musik offenbarte sich in den vielen Jahren, in denen er mit Musikliebhabern in seinem damaligen Wohnort Bad Soden im Taunus und in Nachbarorten Hausmusik gemacht hatte. Und dann gab es da noch den ‚unkonventionellen' Chef, mit dem der Verfasser 15 gemeinsame Berufsjahre im IFAG verbrachte. Unvergessen bleibt, wie wir beide an einem heißen Sommertag auf seinen Vorschlag hin das Prüfen einer geplanten OEEPE-Veröffentlichung spontan vom Dienstzimmer in den schattigen Park der Villa Meister verlegten.

RUDOLF FÖRSTNER hat nach langer Lebenszeit nun den Weg in die Ewigkeit beschritten. Die ihn kannten, werden sich seiner gern erinnern.

HEINZ SCHMIDT-FALKENBERG, Trostberg
30. 12. 2011

Veranstaltungskalender

2012

14.–16. März: 32. Wissenschaftlich-Technische **Jahrestagung der DGPF** in **Potsdam**. dgpf.de/neu/jahrestagung/informationen.htm

20.–22. März: **FOSSGIS** 2012 in **Dessau**. fossgis.de/konferenz/2012/

28.–30. März: **GEOINFORMATIK 2012** – Mobilität und Umwelt in **Braunschweig**. geoinformatik2012.de

11.–12. April: 8. **GeoForum MV** 2012 in **Warnemünde**. geomv.de/geoforum/

17.–18. April: 6th **International Satellite Navigation Forum** – NAVITCH 2012 in **Moskau**, Russland. eng.glonass-forum.ru

23.–27. April: **Geospatial World Forum** 2012 in **Amsterdam**, Niederlande. geospatial-worldforum.org

7.–9. Mai: **GEOBIA 2012**: 4th International Conference on Geographic Object Based Image Analysis 2012 in **Rio de Janeiro**, Brasilien. inpe.br/geobia2012

8.–10. Mai: 11. **Österreichischer Geodätentag** in **Velden** am Wörthersee, Österreich. ogt2012.at

7.–12. Juni: **WHISPERS 2012**, Workshop on Hyperspectral Imaging and Signal Processing, in **Shanghai**, China.

14.–15. Juni: 8. **GIS-Ausbildungstagung** in **Potsdam**. gis.gfz-potsdam.de/index.php?id=238

4.–6. Juli: **AGIT** 2012 - Symposium und Fachmesse für Angewandte Geoinformatik in **Salzburg**, Österreich. agit.at

22.–27. Juli: **IGARSS 2012**, International Geoscience and Remote Sensing Symposium, in **München**. igarss12.org

24. August–3. September: **XXII ISPRS Congress** 2012 in **Melbourne**, Australien. isprs2012-melbourne.org

7.–13. Oktober: **ECCV 2012**, European Conference on Computer Vision, in **Florenz**, Italien. eccv2012.unifi.it

9.–11. Oktober: **INTERGEO 2012** und **60. Deutscher Kartographentag** und **3. Europäischer Kongress der CLGE** (Comité de Liaison des Géomètres Européens) in **Hannover**. intergeo.de

16.–18. Oktober: 9th **Symposium on Location-Based Services** in **München**. lbs2012.tum.de

2013

30. April–2. Mai: 8th **International Symposium on Mobile Mapping Technology** 2013 in **Tainan**, Taiwan. conf.ncku.edu.tw/mmt2013

25.–30. August: 26th **International Cartographic Conference (ICC)** in **Dresden**. icc2013.org

2.–6. September: XXIVth **CIPA Heritage Documentation Symposium** in **Straßburg**, Frankreich. cipa.icomos.org

9.–13. September: 54. **Photogrammetrische Woche** in **Stuttgart**.

8.–15. Dezember: **ICCV 2013**, International Conference on Computer Vision, **Sydney**, Australien. iccv2013.org

Zum Titelbild

3D-Modellierung des Mt. Everest aus 50 cm Satellitendaten

Lagegenaue 3D-Koordinaten sind heute die Grundlage für weite Bereiche der Forschung, Planung und verschiedenste Anwendungen. Das Titelbild zeigt eine 3D-Visualisierung des Mt. Everest, die auf Grundlage von optischen Satellitendaten des Satelliten WorldView-2 (Digital Globe) mit 50 cm Auflösung im panchromatischen Kanal und 2 m in den Multispektralkanälen erstellt wurde. Die Satellitendaten wurden von Mitte Februar bis Mitte März 2010 aus drei unterschiedlichen Orbits aufgenommen (eine Einzelaufnahme, eine Stereoaufnahme und eine Tripelaufnahme – drei enge Stereowinkel aus einem Orbit). Die Abdeckung aus verschiedenen Blickrichtungen ermöglicht sowohl eine hochgenaue Stereoauswertung als auch eine annähernd komplette Abdeckung des Mt. Everest-Massivs ohne wesentliche Verdeckungen.

Die Orientierung der Zeilen-Daten und das Matching (semiglobal Matching) der Stereopaare wurde mit Software durchgeführt, die am Institut für Robotik und Mechatronik in Berlin und Oberpfaffenhofen entwickelt wurde. Die Prozesskette wurde in den letzten Jahren anhand von digitalen Luftbilddaten entwickelt und wird seit zwei Jahren auch erfolgreich auf Satellitendaten der optischen Satelliten WorldView-1 und -2 angewandt. Erstmals konnten aus Satellitendaten Oberflächenmodelle von Landschaften und Stadtgebieten mit einer Lagegenauigkeit von wenigen Metern berechnet werden.

Der Datensatz ist der erste, für den neben Stereobildpaaren auch multispektrale Daten verfügbar waren. Aus diesen konnte trotz des starken Reliefs des Mt. Everest flächendeckend ein farbig texturiertes 3D-Modell erstellt werden.

Die Verarbeitung der Daten war mit Schwierigkeiten verbunden, da es zwischen den Aufnahmen zu einer Neuschneeauflage gekommen war und sich darüber hinaus die Oberflächenstruktur der Gletscher innerhalb von drei Wochen deutlich verändert hatte. Eine komplett automatisierte Verarbeitung war deshalb nicht möglich. Die Firma 3D RealityMaps hat aus den 3D-Modellen und den Texturen eine interaktive Visualisierung erstellt.

Weitere Infos und Links zur interaktiven 3D-Welt und Videos zum Mt. Everest in 3D sind zu finden unter:

http://www.dlr.de/dlr/presse/desktopdefault. aspx/tabid-10308/471_read-780/year-2011/

Dipl.-Geol. Frank Lehmann
Abteilungsleiter Sensorkonzepte und Anwendungen, Einrichtung Optische Informationssysteme am Institut für Robotik und Mechatronik, Deutsches Zentrum für Luft- und Raumfahrt, Rutherfordstr. 2, 12489 Berlin, Germany, Tel.: +49-30-67055-425, Fax: +49-30-67055-385, e-mail: frank.lehmann@dlr.de, www.dlr.de/os/

Korporative Mitglieder

Firmen
AEROWEST GmbH
AICON 3D Systems GmbH
aphos Leipzig AG
Becker GeoInfo GmbH
Bernhard Harzer Verlag GmbH
Blom Deutschland GmbH
Brockmann Consult
bsf swissphoto GmbH
Büro Immekus
CGI Systems GmbH
con terra GmbH
DELPHI IMM GmbH
Deutsches Bergbau-Museum
EFTAS Fernerkundung Technologietransfer GmbH
ESG Elektroniksystem- und Logistik-GmbH
ESRI Deutschland GmbH
EUROPEAN SPACE IMAGING
Eurosense GmbH
fokus GmbH
g.on experience gmbh
GAF GmbH
GeoCart Herten GmbH
GeoContent GmbH
Geoinform. & Photogr. Engin. Dr. Kruck & Co. GbR
geoplana Ingenieurgesellschaft mbH
GEOSYSTEMS GmbH
GGS - Büro für Geotechnik, Geoinformatik, Service
Hansa Luftbild AG
IGI - Ingenieur-Gesellschaft für Interfaces mbH
ILV Ing.-büro für Luftbildausw. und Vermessung
Imetric 3D GmbH
Infoterra GmbH
INVERS - Industrievermessung & Systeme
ITT Visual Information Solutions Germany
J. Linsinger ZT-GmbH
Jena-Optronik GmbH
Leica Geosystems GmbH
Luftbilddatenbank-Würzburg
Messbildstelle GmbH
Microsoft Photogrammetry
MILAN Geoservice GmbH
PHOENICS GmbH
PMS - Photo Mess Systeme AG
RIEGL Laser Measurement Systems GmbH
RWE Power AG, Geobasisdaten/Markscheidewesen
technet GmbH
TRIGIS Vermessung + Geoinformatik GmbH
Trimble Germany GmbH
trimetric 3D Service GmbH
Wichmann, VDE Verlag GmbH
Z/I Imaging Ltd.

Behörden
Amt für Geoinformationswesen der Bundeswehr
Bayerische Landesanstalt für Wald und Forstwirtschaft
Bundesamt für Kartographie und Geodäsie
Bundesmin. für Ernäh., Landw. u. Verbraucherschutz
DB Netz AG
Hess. LA für Bodenmanagement und Geoinformation
Innenministerium NRW, Gruppe Vermessungswesen
Inst. für Umwelt- und Zukunftsforschung
LA für Geoinformation und Landentwicklung, BW
LA für Vermessung und Geoinformation, Bayern
LB Geoinformation und Vermessung, Hamburg
LB f. Küstenschutz, Nationalpark u. Meeresschutz, SH
Landesvermessung und Geobasisinformation Nieders.
Märkischer Kreis, Vermessungs- und Katasteramt
Regierungspräs. Tübingen, Abt. 8 Forstdirektion
Regionalverband Ruhr
Staatsbetrieb Sachsenforst Pirna
Stadt Bocholt, Fachbereich 31
Stadt Düsseldorf, Vermessungs- und Katasteramt
Stadt Köln, Amt für Liegensch., Verm. und Kataster
Stadt Wuppertal, Verm., Katasteramt und Geodaten
Thüringer LA für Vermessung und Geoinformation

Hochschulen
BTU Cottbus, Lehrstuhl für Vermessungskunde
FH Frankfurt a.M., FB 1, Studiengang Geoinformation
FH Mainz, Inst. f. Raumbez. Inform.- und Messtechn.
Jade Hochschule, Inst. für Angew. Photogr. und Geoinf.
HCU HafenCity Universität Hamburg, Geomatik
HfT Stuttgart, Vermessung und Geoinformatik
HS Bochum, FB Vermessung und Geoinformatik
HS Karlsruhe, Fakultät für Geomatik
HTW Dresden, FB Vermessungswesen/Kartographie
KIT Karlsruher Inst. f. Technologie, Inst. für Photogrammetrie und Fernerk.
LUH Hannover, Inst. für Kartogr. und Geoinformatik
LUH Hannover, Inst. für Photogrammetrie und GeoInf.
MLU Halle, FG Geofernerkundung
Ruhr-Uni Bochum, Geographisches Institut
RWTH Aachen, Geodätisches Institut
TU Bergak. Freiberg, Inst. f. Markscheid. u. Geodäsie
TU Berlin, Computer Vision & Remote Sensing
TU Berlin, Inst. f. Geodäsie und Geoinformationstechnik
TU Braunschweig, Inst. für Geodäsie und Photogr.
TU Clausthal, Inst. für Geotechnik und Markscheidew.
TU Darmstadt, Inst. für Photogrammetrie und Kartogr.
TU Dresden, Inst. für Photogrammetrie und Fernerk.
TU München, FG Photogrammetrie und Fernerk.
TU Wien, Inst. für Photogrammetrie und Fernerk.
Uni Bonn, Inst. für Photogrammetrie
Uni Göttingen, Inst. für Waldinv. und Waldwachstum
Uni Heidelberg, IWR Interdis. Zentr. f. Wiss. Rechnen
Uni Kassel, FB Ökologische Agrarwissenschaften
Uni Kiel, Geographisches Institut
Uni Stuttgart, Inst. für Photogrammetrie
Uni Würzburg, Geographisches Institut
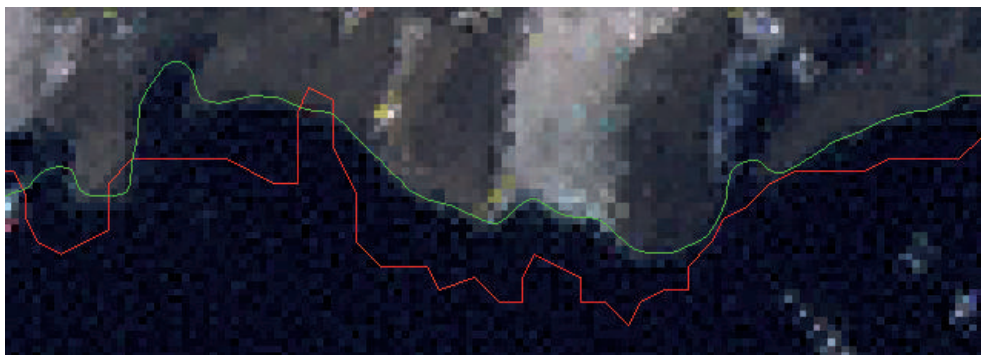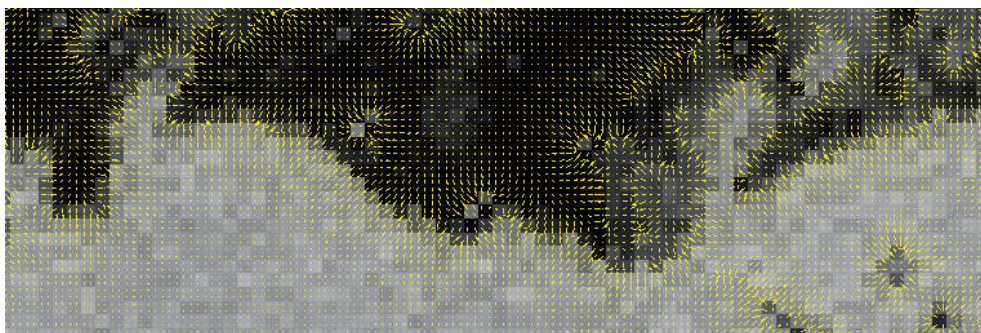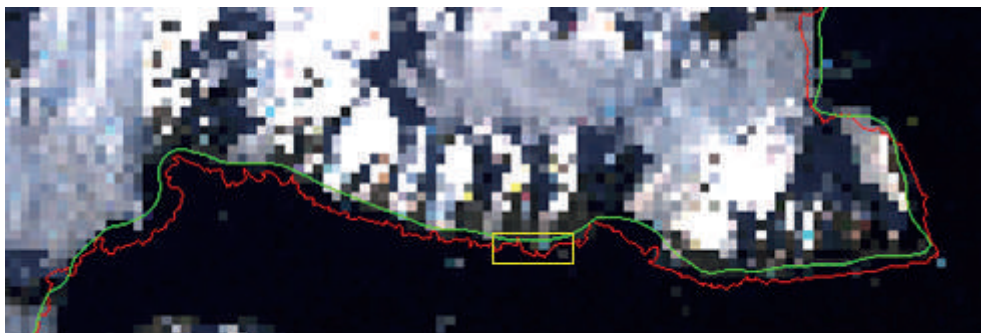Uni zu Köln, Geographisches Institut

Corrigendum to PFG 6/2011

Dear readers of PFG,

on page 431 of a.m. volume Fig. 9 has been published without consideration of the author's corrections.
Therefore, please find now here the correct version of Fig. 9.
We apologize for the inconvenience.

Schweizerbart Science Publishers

Autorenantwort zur Buchbesprechung

Peter Kohlstock: Topographie – Methoden und Modelle der Landesaufnahme, Verlag de Gruyter 2011 (PFG 4/2011)

Die oben genannte Buchbesprechung ist in einigen Punkten leicht zu korrigieren. Nach den Worten des Rezensenten wird mit dem Buch eine „Entwicklungsgeschichte der topographischen Landesaufnahme" vorgelegt. Dieses Thema wird nur kurz behandelt. Stattdessen liegt der Schwerpunkt auf den heutigen Verfahren der topographischen Landesaufnahme. Der in der Rezension herangezogene Vergleich der Verfahren zur Kartenfortführung bei der amtlichen Vermessung und beim Alpenverein ist eine interessante Idee des Rezensenten, jedoch kein Gegenstand des vorgelegten Buches. Das Messtischverfahren wird am Rande erwähnt, aber nicht als heute noch wichtiges Verfahren vorgestellt.

Peter Kohlstock